DELFT UNIVERSITY OF TECHNOLOGY

ET4300 MASTER THESIS

HVDC GIS Magnetic Field Antenna System Characterization

By:

Avinash Vasudeva Nayak

in partial fulfilment of the requirements for the degree of
Master of Science
in Electrical Engineering at the Delft University of Technology,
Faculty of Electrical Engineering,
Mathematics and Computer Science, Electrical Sustainable Energy Department,
DC Systems and Storage Group,
The Netherlands,
to be defended online on Thursday August 27, 2020 at 10:00 AM.

Responsible Supervisor:
Dr. A.Rodrigo Mor TU Delft
Daily Supervisors:
Dr.ir.Fabio Muñoz TU Delft & Dr. Luis Carlos Castro Heredia TU Delft
Thesis Committee:
Prof. Ir. Peter Vaessen TU Delft, Dr. Armando Rodrigo Mor TU Delft & Dr. Milos Cvetkovic TU Delft

Abstract

Partial Discharge (PD) measurements are of great importance to enable the monitoring and diagnostics of HV systems. The requirements of the Paris Agreement and climate goals have fuelled the increase in penetration and demand of HVDC for offshore wind. The HVDC Gas Insulated Switchgear (HVDC GIS) is a reliable technology to support the necessary electrical infrastructure. Nevertheless, some in-service failures may occur. These failures can occur in the insulation system and thus developing a measurement system for PD detection is essential for monitoring and diagnostics.

To monitor and diagnose the HVDC GIS, a novel Magnetic Antenna (MA) is being developed to operate in the high-frequency (HF) (30-300 MHz) range. The well-established UHF method for the GIS is typically used due to its high sensitivity and resilience to electromagnetic interference. However, the UHF method is unable to calibrate to apparent charges as this information is in the low frequency (up to 30 MHz) until HF range. The knowledge of charge calibration indicates the discharge type which is important in DC as DC does not have phase-resolved information as with AC. The appropriate frequency range of the MA should enable the measurements of the apparent charge and localize the defects when monitoring and diagnosing a HVDC GIS setup.

The overarching goal is to develop a measurement system to measure PDs in the HF range in a GIS setup. For this purpose, MAs are created and investigated. A workbench has been built and developed to characterize the MAs and measure its frequency characteristics. A 380 kV GIS measurement setup has been developed. This enabled the measurement and acquisition of data of the discharges using the MAs. The Threshold Peak detection (TPD), Energy Criterion (EC), and Phase Method (PM) localization methods are investigated and implemented for localization of the source of defects. The PM is unable to localize the pulse due to its sensitivity to noise and reflections. The TPD and EC are both suitable with the TPD being the preferred method due to its 95% accuracy of localizing the defect within $\pm$ 1.5 m.

Acknowledgements

I would like to thank my supervisors Dr. A.Rodrigo Mor, Dr.ir.Fabio Muñoz, and Dr. Luis Carlos Castro Heredia for their continued support and making the project an enjoyable and productive learning process. I would also like to thank Prof. Ir. Peter Vaessen for his invaluable feedback for the thesis. Moreover, I express my gratitude to the rest of the High Voltage Staff at the TU Delft for their assistance and interesting discussions particularly at the coffee machine in the high voltage laboratory.

I would also like to thank my sponsors ASML and the Energietalenten for providing me scholarships and invaluable learning experiences and networks.

I would like to thank all of my classmates, and professors who helped me on my academic journey of becoming an electrical engineer. I would like to thank my roommates and other close friends for their support and all the enjoyable moments. Lastly, I want to thank my mother and father for all they have done and continue to do for me.

Contents

List of Figures

List of Tables

Nomenclature, Acronyms and Abbreviations with Notation

AC: Alternating Current

CM: Common Mode

DC: Direct Current

EC: Energy Criterion

EMF: Electromotive Force

GIS: Gas Insulated Switchgear

HF: High Frequency

HV: High Voltage

HVDC: High Voltage Direct Current

MA: Magnetic Antenna

N/A: Not Applicable

PD: Partial Discharge

PDF: Partial Discharge Filter

PM: Phase Method

PPLG: Picosecond Pulse Lab Generator

TE: Transverse Electric

TEM: Transverse Electromagnetic Mode

TOA: Time Of Arrival

TPD: Threshold Peak Detection

UHF: Ultra High Frequency

1 Introduction

1.1 Background

Renewable energy sources are becoming of increasing importance due to the Paris Agreement climate goals and the negative climate change consequences. In the Netherlands, particularly the growth of off-shore wind is of increasing importance. This is exemplified by the roadmap devised by the "Rijksdienst voor Ondernemend Nederland" (RVO) [The Netherlands Enterprise Agency] which entails a growth from 1000 MW in 2015 to 4500 MW in 2023 [1]. Moreover, there are developments from transmission system operators such as TenneT striving to increase the connection capacity by an additional 6.1 GW for the 2030 roadmap [2]. An offshore wind substation is shown in Figure 1.

Figure 1: Offshore Wind Substation [3].

Amongst important policies, the ambition of increasing the capacity of offshore requires a plethora of technical developments to support the infrastructure. HVDC can also be used for the transport of energy as an alternative to AC transmission. Several technical benefits of HVDC include the bulk power transmission over long distances due to AC consuming reactive power with the parallel capacitance paths in cables and other losses such as the skin effect. Another advantage is the power exchange between two asynchronous networks overseas. This also enables markets to be coupled encouraging a price competition for exchanging energy. Moreover, HVDC is preferred due to its cost-effectiveness with capex and opex for distances above 50km for offshore applications [4]. Due to these prevalent benefits, it is also important to monitor and diagnose up and coming technology in HVDC. The project PROMOTioN (PROgress on Meshed HVDC Offshore Transmission Networks, see Figure 2) under the EU Horizon 2020 aims to make progress regards to developing a meshed HVDC grid [3]. The GIS is an essential unit of the electrical infrastructure required to realize this. This is the first time that such equipment is tested in an independent commercial laboratory.

Figure 2: PROMOTioN Project Logo [5].

The GIS is a gas insulated switchgear which has promising prospects in HVDC transmission for offshore substations. This is relevant as aforementioned due to the increased demand and penetration of off-shore

Figure 3: PROMOTioN Project ABB's 320 kV HVDC gas insulated switchgear (GIS) test equipment in the KEMA High Voltage DC Laboratory in Kleefse Waard, Arnhem, Netherlands. [6].

turbines. A GIS is a switchgear that is encapsulated in metal with high-pressure gas inside. A switchgear in the context of electrical power systems contains fundamental high voltage electrical components such as switches, fuses, disconnectors and circuit breakers [7]. The GIS is essential to enabling the control and protection of electrical equipment. The coaxial structure is used with the inner-conductor transporting power, grounding the exterior enclosure and is insulated using gas. The interior is supported using solid insulation known as spacers. A GIS is typically filled with SF_6 with the second generation using a gas mixture technology involving N_2. The benefit of the hybrid second generation provides better insulation characteristics whilst reducing the amount of the harmful SF_6 greenhouse gas which is relevant during potential leaks. Using GIS technology with other gases over conventional air-insulated options result in a 90% reduction in volume [6]. This reduction is especially useful in offshore applications where space is limited and expensive. An example of a GIS is shown in Figure 4.

Figure 4: GIS Example [8] inside of a yellow substation in Figure 1

Partial Discharge (PD) measurements enable the monitoring and diagnostics of the GIS system. This can thus notify the operator of the type of defect in the system so that appropriate measures can be devised and if necessary executed. As defined in the IEC 60270 standard, Partial discharges (PD) are localized electric discharges which partially bridge the insulation between conductors [9]. They are progressively detrimental to the insulation and this deterioration may ultimately lead to insulator failure. It is therefore important to monitor and diagnose this phenomenon so appropriate measures can be made.

1.2 Problem Statement

Early detection and localization of a PD source can enable insights for example for preventive maintenance to deter dangerous and costly breakdowns. The detection method investigated in the thesis involves research on high frequency (HF) magnetic antennas. A magnetic antenna has already been designed for this purpose. This magnetic antenna needs to be constructed, developed and characterized in terms of frequency performance with various amplifiers. Furthermore, it has to be tested in a GIS setup to determine its suitability for localization purposes. Although not explored this thesis, the antenna can also be used to determine the PD apparent charge in pC. This is to determine the severity of the discharges. This is particularly important in DC as the phase resolved information which provides clearer categorization of the type of discharge is unavailable when compared to AC. In DC the magnitude of the discharges provide indications for characterizations of the defects. On the whole, these developments will result in valuable research towards developing a measuring system as part of the PROMOTioN project pertaining to the application of offshore HVDC GIS PD monitoring.

1.3 Research Goals

The overarching problem statement involves developing a measurement system to measure PDs in the HF range. For this purpose, a magnetic antenna is investigated. The research goals are expressed in the following milestones:

- Workbench Development: Build and develop a workbench for the characterization of the magnetic antennas.
- Magnetic Antenna Characterization: Use the workbench to measure the antenna response and process the data to determine the frequency characteristics.
- Conference paper: Contribute to a paper for CIGRE Paris 2020 on "A NEW PARTIAL DISCHARGE MEASURING SYSTEM IN HVGIS BASED ON MAGNETIC FIELD ANTENNAS".
- Measurement GIS Setup: Develop the magnetic antenna measurement infrastructure for the 380 kV GIS at the High Voltage Laboratory of the Delft University of Technology.
- Localization: Research, implement, and evaluate 3 algorithms for localizing PD defect sources in the GIS system using the magnetic antennas.

The main scientific contributions envisioned are developing a workbench to characterize the designed magnetic antenna and to assess the localization capabilities of the antennas with the TPD, EC and PM algorithms on a GIS setup.

1.4 Thesis Structure

The thesis structure is divided into eight chapters. The chpater contents are as follows:

Chapter 2: The fundamentals of PDs are explored. The main focus of the chapter lies in prior research of electrical PD sensing with high-frequency current transformers (HFCTs) and magnetic antennas which acts as a springboard for the thesis.

Chapter 3: The workbench to characterize the magnetic antenna is explored. An initial workbench and a developed workbench are created. The steps to create the developed workbench and concepts on how to mitigate undesired reflections are explained and implemented.

Chapter 4: The magnetic antenna is characterized using the developed workbench. The construction of the antenna is explained. The frequency behaviour of the time domain input current is investigated with

the HFCT and the output voltage is measured using the antenna. The antenna is investigated with several amplifiers and passive components. Finally, the antennas bode response is investigated to investigate resonance peaks.

Chapter 5: The 380 kV GIS setup at the Delft University of Technology High Voltage Lab is used for testing the magnetic antenna measurement system. The measurement system and its equipment are systematically constructed to enable proper analysis and tests of the magnetic antenna.

Chapter 6: Three algorithms for localization of PDs in the GIS setup are explored. The Threshold Peak Detection, Energy Criterion, and the Phase Method are implemented and evaluated for its suitability in terms of accuracy, reliability and run time.

Chapter 7: The conclusions of the research are presented and a future scope of recommendations and a research path is outlined.

Chapter 8: In the appendix, supplementary supporting information for the chapters, and a complete overview of the measurements are presented. Moreover, a list of figures and tables are included.

2 Fundamentals

Fundamental theory and elements of relevant literature research and review are explored as required prior knowledge. Relevant literature elements to be investigated for the project have also been embedded into other sections as part of a dynamic process based on the necessity of information.

2.1 Partial Discharges

PDs are initiated if the voltage stress exceeds that of the corona inception voltage of the void/object. The equivalent circuit for internal PD from the IEC60270 standard is shown in Figure 5. A discharge occurs when the voltage V_c across the capacitor c surpasses the breakdown voltage U_d following from the Paschen curve [9]. The actual charge displacement is $q1$ across capacitor c across the void. However, as per convention, the apparent charge q is used. This is because q can be calibrated and is roughly inversely proportional to the insulation thickness. Furthermore, the magnitude of q is an appropriate representation of the intensity as its directly related to the energy dissipated, the dimension of the cavity.

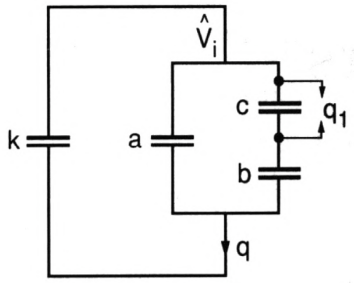

Figure 5: ABC network PD from IEC60270 [9].

When a PD occurs, a high-frequency transient current pulse occurs. The current flowing through the impedance of the component gives a voltage pulse. In the time domain the pulse duration is in the order of nanoseconds. It has a wide frequency spectrum up to low GHz components [10].

2.2 Prior Research

The thesis continues on the research initiated by the DCE&S group at the High Voltage Laboratory of the Delft University of Technology. A review of their published papers concerning PD measurements for GIS applications is conducted. Firstly, the paper presenting a novel measuring system using the HFCT in the high-frequency range for a high-frequency current transformer (HFCT) is explored. Secondly, the paper presenting a novel measuring system using an antenna detecting the magnetic field is explored. Finally, the latest publication develops on the antenna creating a single loop antenna for PD measurements.

In the GIS structure, there are spacers that are connected through bolts. HFCTs are installed at the bolts of the spacers that pickup the PD induced currents in the enclosure. The bandwidth of the HFCT used is in the order of hundreds of kHz to a few hundred MHz. A benefit with the HFCT is the lower frequency range relative to the HF and UHF method. The UHF method uses a frequency range of 300-3000 MHz which avoids the noise caused through power electronic switching. The HF also has better noise suppression due to its bandwidth of 30-300 MHz. Nevertheless, the damping and dispersion of electromagnetic waves in the GIS components such as spacers, T-share branches and E-Bends, is remarkable for the higher frequencies [11]. Hence the system measuring in the HF range is beneficial due to the lower attenuation. The PD currents are distributed over the bolts and a high gain amplifier is used to amplify the mA currents which are detected. Increasing the number of turns increases gain but reduces bandwidth, for the application, bandwidth had a

higher priority. A configuration of one sensor at a bolt was used with the other 15 bolts are other current paths was used as the effects of reflections are minimal when compared to other configurations. The charge calculation might be possible with the HFCT method but the influence of partial reflections at the GIS components needs to be investigated. A limitation of the HFCT sensors is that they are only installable in GIS designs featuring external spacers.

Continuing on the research, the paper presenting the novel antenna for PD measurements in a GIS based on Magnetic Field detection is explored. These antennas can be placed in the dielectric windows present in the coaxial GIS which is beneficial compared to the spacers required for the HFCTs. The UHF bandwidth is used where the TE11 is the dominant mode and the higher frequencies are more resilient to noise. The UHF measuring system performance significantly decays with the distance due to the reflections causing attenuation and distortion of the higher frequencies.

PDs cause surface currents to flow homogenously along the inside walls of the outer shield of the GIS and travel around the dielectric window as shown in Figure 6.

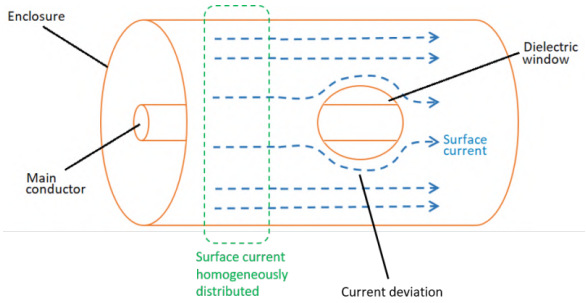

Figure 6: Surface Currents along inside wall of the GIS shield [12].

The principle of magnetic detection involved is detecting the time-varying magnetic field in the dielectric window caused by surface currents. This time-varying field, through Faraday's law, induces a surface electric field. This induced field can be integrated over the closed region to yield an electromotive force (EMF) voltage. To visualize the concept, the induced electric field is shown in Figure 7.

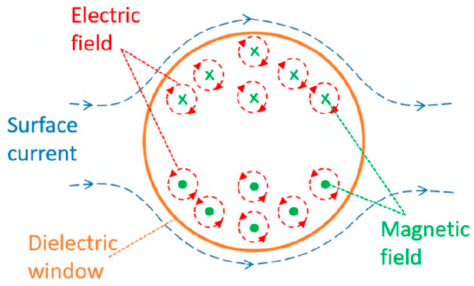

Figure 7: Induced electric field in the dielectric window [12].

In terms of processing the data of the signal detected by the antenna from the induced electric field PD classification is necessary. The antenna signal is classified as a PD if it meets the criteria of the peak occurring around the HFCT time, if the peak amplitude detected is roughly twice the background noise, and that the cumulative instantaneous power indicates a clear pulse [12]. The characterization of the antenna is limited by reflections in the GIS. There are also remaining considerations such as the influence of the number of turns, which in the paper [12] uses 5 turns.

The latest publication considers a single turn antenna for a top and bottom loop. The 5 turn antenna has higher loop inductance and parasitic capacitance creating a resonance peak at 32 MHz. The benefit of a single turn is thus to overcome the bandwidth problem and mitigate signal oscillations [13]. The challenges include time-domain acquisition with large bandwidths and coping with EMI and noise problems associated with it. Algorithms are developed to help recognize PD from noise in an attempt to tackle this issue. TEM waves are detected from the antenna, in the HF and lower end of the VHF range. The loop is formed using the RG179 where the inner conductor is shorted with the screen of the cable to form a loop. The screen is grounded on one size and is floating in the other to provide electrostatic shielding and to prevent short-loop currents which counteract the magnetic field detected by the antenna [13]. This single turn antenna has shifted the resonance peak to 52 MHz from the original 32 MHz from the 5 turn antenna with 5 turns.

The objective is to now continue characterizing and investigating the design of a single turn top and bottom loop magnetic antenna. A workbench is created to investigate the frequency performance and subsequently, the antenna will be tested on the GIS setup.

2.3 Chapter Conclusions

Prior research provided stepping stones to motivate the importance of investigating the HF PD detection over UHF methods. The HF has better noise suppression due to its bandwidth of 30-300 MHz. The damping and dispersion of electromagnetic waves in the GIS components such as spacers, T-shape branches and E-Bends, is remarkable for the higher frequencies [11]. Hence the system measuring within the HF range is beneficial. As a result magnetic antennas are being developed and characterized in this frequency range to detect the TEM mode from the PDs.

3 GIS Workbench

A workbench is designed to characterize the antenna performance and investigate the input pulse in terms of their frequency characteristics. A suitable workbench has to be developed to address the reflections present in the GIS. Minimizing these reflections allows for an undisturbed input signal as a reference. With a clean input, the antenna output voltage behaviour can properly be characterized, as reflections alter the frequency spectrum. Once the input and output are reliable, the transfer impedance can be calculated as their ratio of output voltage upon input current. The initial workbench prepared as a baseline is shown in Figure 8. The developed workbench with resistive wire, termination resistor, and the cone structure is shown in Figure 11 and is subsequently elucidated.

3.1 Initial Workbench

The initial workbench to characterize the magnetic antenna has been constructed. The workbench is shown in Figure 8 and 9. It consists of an outer housing screen and a 0.5 mm diameter inner conductor. A coaxial structure is used with a dielectric window as a slot for the magnetic antenna. This coaxial structure is relevant for the antenna bandwidth and sensitivity due to the antenna and dielectric window interaction. The PD pulse is injected at the beginning with a nanosecond pulse generator. The antenna is placed in the dielectric window of the GIS. When injecting a representative PD pulse from an avalanche pulse generator (See Figure 14), it is observed that reflections occur in this workbench as shown by the waveform in Figure 10. These are reflections as the time separation of peaks of 12 ns are consistent with the dimensions of the workbench and the speed of light.

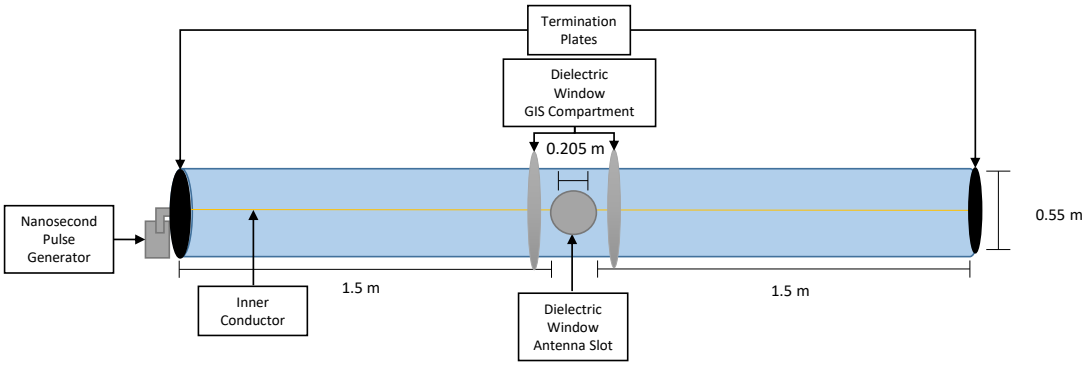

Figure 8: Initial Workbench for Antenna Characterization

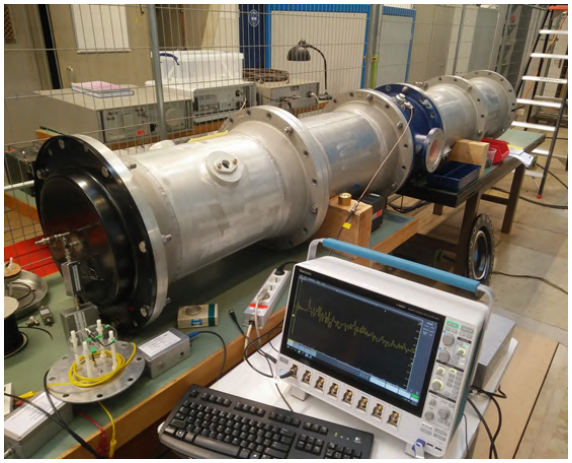

Figure 9: Picture of Initial Workbench for Antenna Characterization

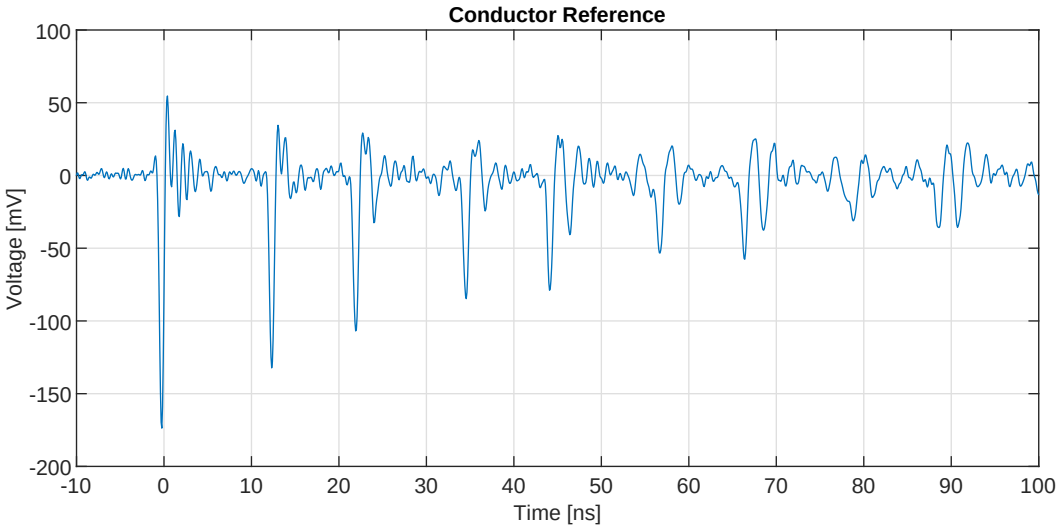

Figure 10: Reflection Reference from Pulse from the Avalanche Pulse Generator on the Initial Workbench Measured using the Bergoz HFCT (Model: FCT-016-5.0)

3.2 Developed Workbench

Measures are explored to address the reflections. After investigating possible solutions to address the reflections, for the thesis the following solutions are implemented:

- Termination resistor
- Cone (Conical elongation on the Injection and Termination sides)
- Resistive wire solution.

The termination resistor would enable impedance matching to cope with reflections. The procedure included selecting a resistor to match the characteristic impedance of the GIS (See Section A.5 for more theory) and then empirically iterating and testing the value until the optimal (330Ω) was discovered.

The implementation of the cone structure was hypothesized to resolve reflections. This geometry would enable the size ratio between the inner conductor and the outer to decrease in order for the characteristic impedance to decay over the distance. This way it also preserves the coaxial structure (the cone is the outer conductor at the injection and termination) and smoothly reduces the characteristic impedance rather than introducing discrete blocks and discontinuities.

The resistive wire is a wire with a uniformly distributed resistance and is used as the inner conductor. It is used to gradually attenuate the pulse and the higher frequencies to decay the reflections.

The developed workbench schematic with the termination resistor, cone structure and resistive wire is presented in Figure 11.

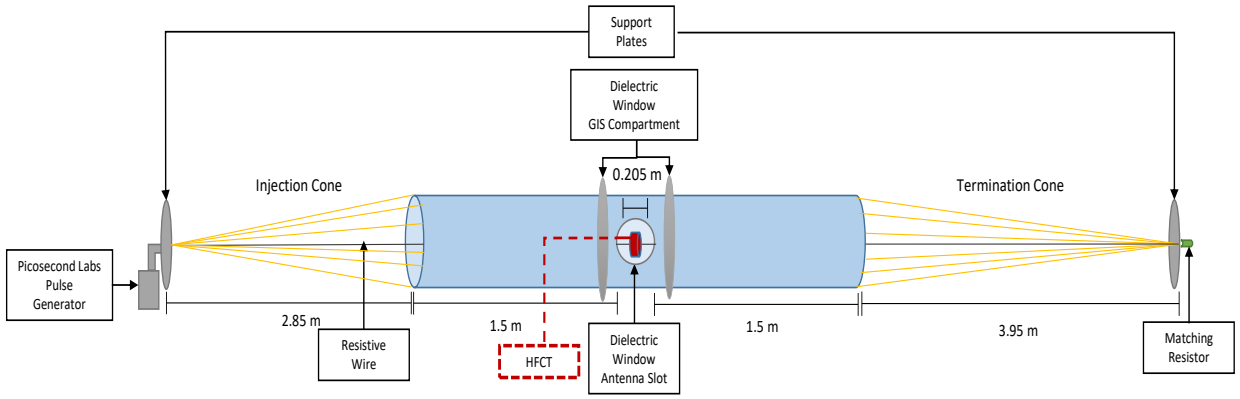

Figure 11: Workbench for Antenna Characterization

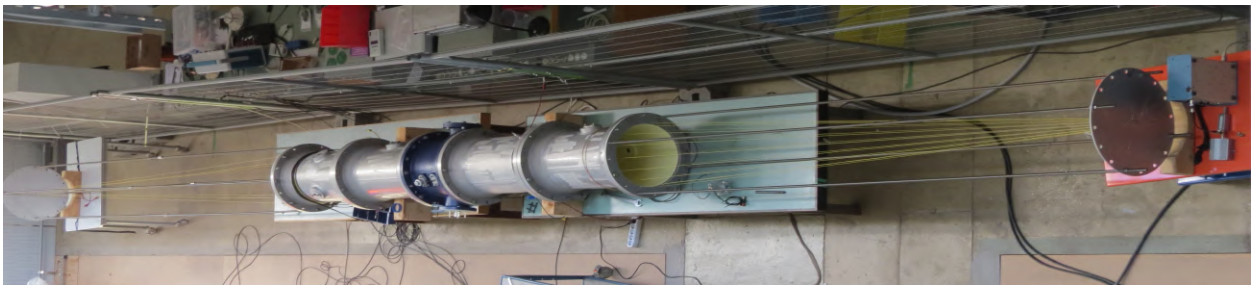

Figure 12: Picture Workbench for Antenna Characterization

On the injection and termination side of the workbench, 16 conducting wires of 0.5 mm diameter are used to connect the grounded outer screen of the GIS to the support plate as shown in Figure 11. This way the continuity of the ground is also sufficiently preserved. Steel bars are also passed through the holes in the GIS as support and connected for the support plate for rigidity and structure. The cone is extended to suit the dimensions of the laboratory. The benefit of extending the cone is two-fold. Firstly, it ensures the decay of the characteristic impedance is more gradual. The conductors are connected to the outerscreen and are fed such that the radius of the outer-screen reduces until the termination. This is done by fixing the outer-screen point and feeding the conductor at an appropriate angle such that the wire reaches the required position at the designed termination plate. Secondly, the increased length provided allows an increased length for the resistive wire and thus increases the damping effect toward reflections. The termination cone is purposefully

larger than the injection cone. The injection cone enables the PD pulse generator and the Nanosecond Pulse generator to both inject adequate pulses in the coaxial structure (See Section 3.3). The termination cone length ensures sufficient attenuation caused by the resistive wire of the reflection before it is detected to the antenna.

The resistive wire chosen is readily available in European markets and applicable for attenuation is the *30531 Resistor Wire 0.3 mm 19.10 Ohm/m, Kanthal*. As mentioned in the name, the diameter of the wire is 0.3 mm and the resistance value is 19.10 Ω/m. This resistive effect should, per transmission theory, attenuate the oscillations and as a result, minimize the reflections. Initially resistive wire of length 1.5 m + 3.95 m is used as the length after the antenna to ensure that the antenna still can read the unimpeded input pulse. It was observed that the high-frequency components are causing an impure pulse and that a small reflection is still present. Hence the resistive wire is also placed in the injection cone for the full length of the workbench smoothening the input signal. The pulses are shown in Figure 16 and Figure 17.

The size ratio of the inner diameter to outer diameter is governed using support plates. The support plate has slots and is designed such that the diameter of the cone created from the wires is 4 cm with enough space for the BNC connections. The diameter ratio of the outer to inner at the support plates and after empirically testing the termination value, results in a matching characteristic impedance of 330 Ω.

3.3 Pulse Generation

An Avalanche pulse generator and a Pulse Generator are explored and used for representative PD pulse generation

Avalanche Pulse Generator
A representative PD pulse is generated using a nanosecond pulse generator. This generator is supplied with an output voltage of 90 V_{DC} and is connected to the input of the ns pulse generator. The generator functions as an Avalanche Pulse Generator as is based on [15]. The circuit parameters are modified for the desired time constant to get a suitable rise time in the order of several hundred picoseconds and hence $C1$ is 14 pF. The output of the pulse generator is connected to the GIS in parallel with a series connection of 93 Ω and 50 Ω resistors that provide a path for the discharge to enter the BNC connection of the GIS and further tune the rise time to an adequate magnitude of 560 ps. This pulse is injected into the conductor which passes through the center of the GIS. It propagates along the wire and reflects at the termination of the GIS.

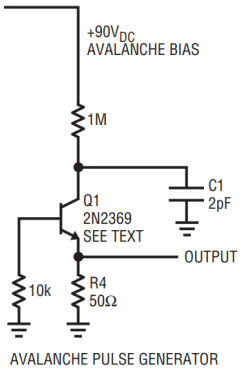

Figure 13: Avalanche Pulse Generator [15]

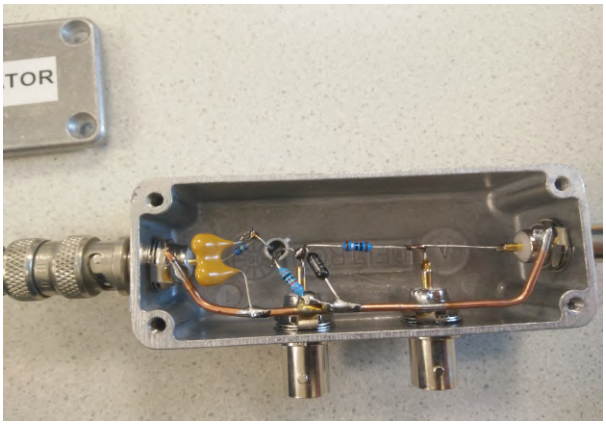

(a) Avalanche Pulse Generator Circuitry

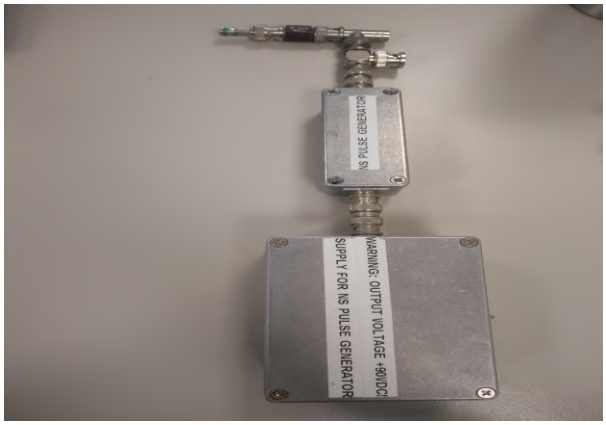

(b) Avalanche Pulse Generator Housing with input resistors

Figure 14: Physical Construction of the Avalanche Pulse Generator

Picosecond Pulse Labs 2000 Pulse Generator

It is observed that the magnitude of the pulse from the avalanche should be increased for further clarity of the frequency characterization of the magnetic antenna. The magnitude of the avalanche pulse generator is insufficient because the voltage amplifier gain is too low resulting in a pulse up to 2.6 mA. This gain is important as the resistive wire used for the developed workbench exponentially attenuates the higher frequencies. In order to provide a larger input pulse, the picosecond pulse lab 2000 is used for this (See Figure 15). The waveforms of the pulse generated from the PPLG are shown in Figure 16 and 17. The rise time is in the order of 730 ps and the peak magnitude is 19.8 mA.

Figure 15: Picosecond Pulse Labs 2000 Pulse Generator

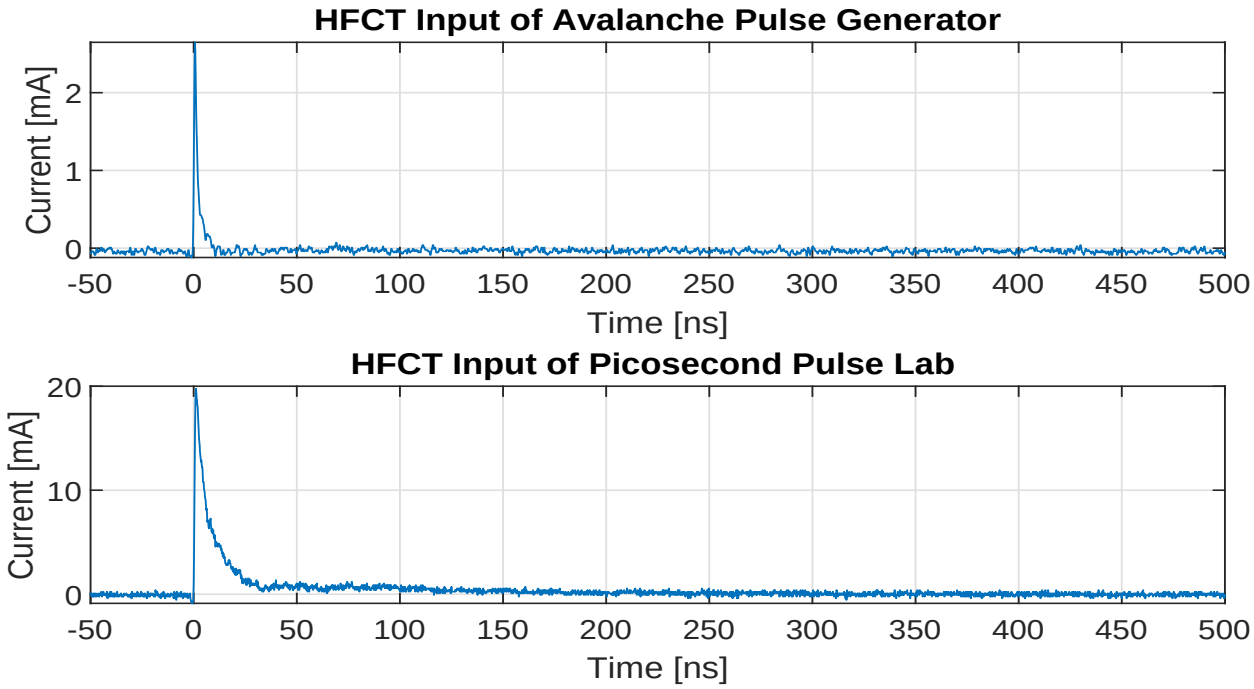

Figure 16: Avalanche Pulse Generator and Picosecond Pulse Lab Generator time domain current waveforms measured by the Bergoz HFCT

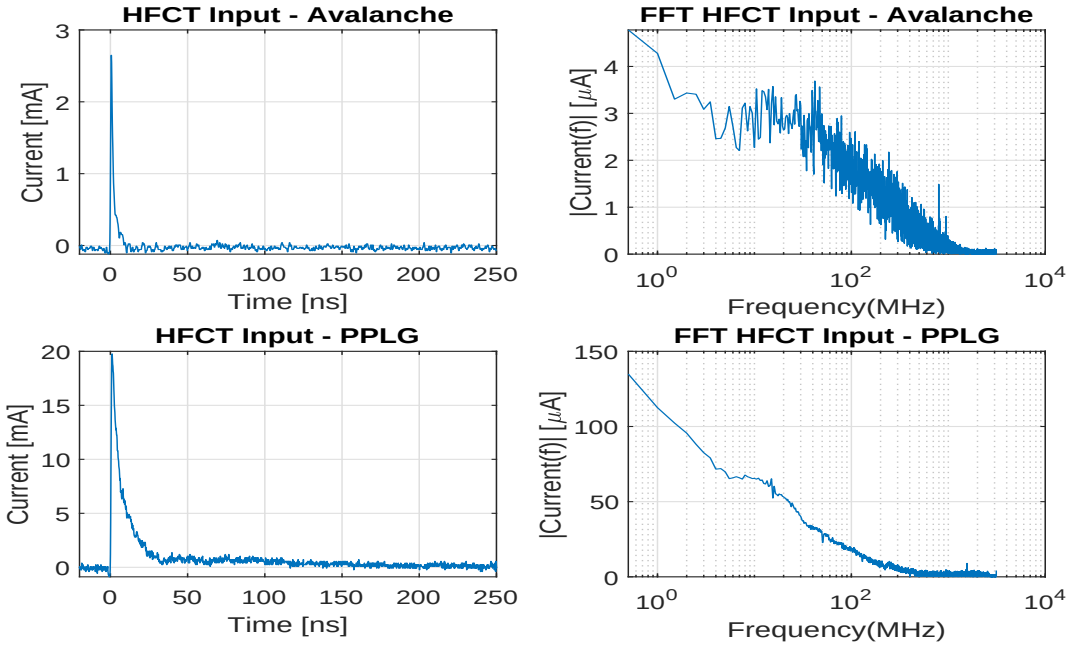

Figure 17: Avalanche Pulse Generator and Picosecond Pulse Lab Generator time domain and frequency domain current waveforms measured by the Bergoz HFCT

Comparing Figure 10 to Figure 16 it is visible that the developed workbench with the termination resistor, cone and resistive wire is able to significantly reduce the reflections. Hence, the termination resistor, cone and resistive wire are suitable for coping with reflections.

3.4 Chapter Conclusions

The initial workbench for the antenna characterization (See Figure 8) is developed (See Figure 11). The resistive termination of 330 Ω, injection and termination cone, resistive wire with a resistance value of 19.10 Ω m is successfully used to cope with reflections as is shown by comparing the input pulses between the initial workbench and the developed workbench which is shown in Figure 10 and Figure 16 respectively. The PD waveforms of the pulse injection methods of the PPLG and Avalanche pulse generator in the developed workbench are shown in Figure 17. From the input response, it is observed that the developed workbench is suitable for characterizing the magnetic antenna.

4 Antenna Design and Characterization

This chapter delves into the designed antenna and its use in the GIS workbench. Its construction is explained and several amplifiers are tested. The antenna response is extracted with different pulse generators and attachments to the antenna. The frequency behaviour of the time domain input current and output voltage is characterized. Furthermore, the transfer function and phase are calculated and represented in bode plots. Finally, an analysis of the results obtained is presented with the chosen configuration of the antenna and its attachments.

4.1 Antenna Construction

The designed and considered antenna is shown in Figure 18. The antenna loops are constructed using the RG179 coaxial cable. This is because the co-axial cable has shielding properties as well as a thin conductor resulting in lower inductance and thus favourable electrical parameters. The inner conductor is connected to the grounded screen to form a loop from a single cable. It is then connected in a clockwise fashion to form the top loop. Likewise the same is repeated for the bottom loop. The ends of the antenna loops are passed to the metal plate and connected using suitable RF SMA connectors. On the outside of the plate, for each loop, an SMA to co-axial adaptor is used to feed the antenna with the amplifiers as shown in Figure 21. This antenna is tuned to detect TEM waves in the HF and low VHF range.

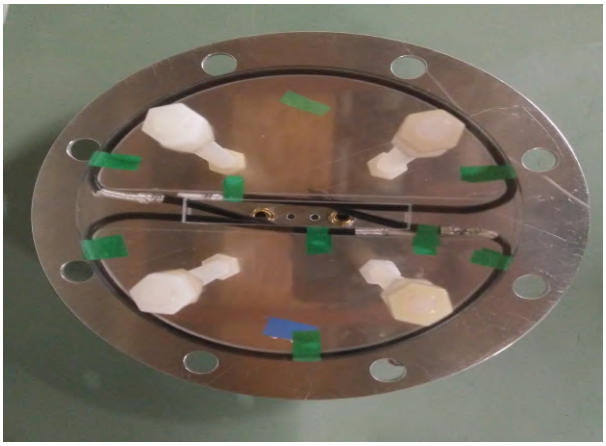

(a) Antenna Aerialview

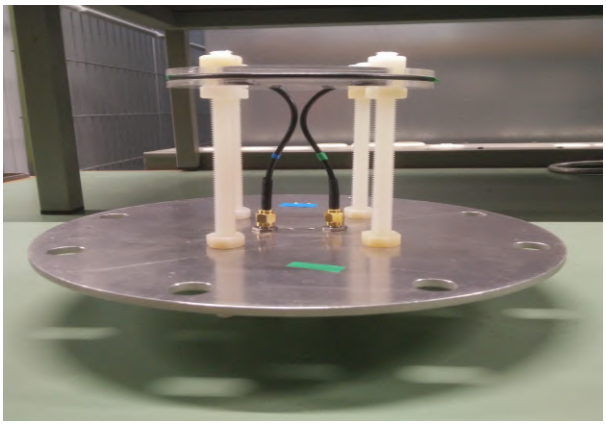

(b) Antenna Sideview

Figure 18: Antenna Side birds-eye view and side-view

4.2 Amplifier Considerations

The workbench is created to identify the frequency response and behaviour of the antenna. This enables the identification of potential resonance peaks and the suitability of the antenna in the HF range. Different amplifiers are used to investigate the spectrum. Desirable properties of the amplifiers include a high gain, high bandwidth with low noise in the output.

In terms of the high gain, a relatively higher gain can ensure sufficient amplification of small pulses which improves the sensitivity. This results in enabling the detection of smaller PDs and achieving the desired sensitivity of 5 pC.

In terms of a high bandwidth, there are multiple considerations. The high bandwidth is desired to characterize the magnetic antenna in the workbench. This wide frequency spectrum allows the detection of resonance

peaks caused by the inductance and capacitances of the antenna and captures the entire spectral behaviour of the antenna. Consequently, the antenna design can be improved and iterated upon to shift the resonances to higher frequency ranges outside of the desired HF detection range. Furthermore, other high-frequency interferences and noise such as the CM influence can be observed. The majority of the charge is in the low MHz range. Increasing the frequency may improve the accuracy of the charge detected because there is more spectral content that can be included in the charge integral. Nevertheless, a concern might be the higher frequency noise introduced which could be more detrimental than the slight improvement in accuracy. Hence noise rejection will also have to be considered. The choice of the appropriate bandwidth for the amplifiers needs to be experimentally verified with the trade-off between the pros and cons of the gain and bandwidth.

The main purpose of the measuring system is to detect the PD and localize the compartment for servicing. Greater accuracy with the charge magnitude and the accuracy of the localization is supplementary. As aforementioned in Section 1), the TEM mode should be detected due to its lower attenuation than TE11. This also infers that the TEM mode, in theory, would be better for localization. Moreover, an essential consideration is that for the TEM mode, the PD pulse travels according to transmission line theory and can be analysed through basic electric circuits. The low frequency (up to 100 s of MHz) could be suitable as frequency components exceeding 500 MHz are significantly damped by spacers, T-shape branches, and E-bends [18]. In theory, the bandwidth of the amplifier up to 300 MHz will be sufficient, it is then a priority to select an amplifier with the highest gain and low noise. In theory, the bandwidth of the amplifier up to 300 MHz will be sufficient. Available amplifiers which are considered are listed in Table 1 with their relevant parameters and are displayed in Figure 19 and Figure 20.

Table 1: Parameters of Amplifiers

Name	Femto 40M-100K	300-70 Mini circuits	300-69 Mini circuits	Femto 400M-5K
Amplification type	Current	Voltage	Voltage	Current
Bandwidth $[MHz]$	40	1000	1000	400
Gain [dB]	100	25.1	25.5	74.0
f_{low} $[MHz]$	0	0.024	0.023	0
f_{high} $[MHz]$	40	1140	1150	400
Input Resistance $[\Omega]$	50	50	50	50

Figure 19: 40M-100K (left) and 400M-5K (right) Femto Current Amplifiers

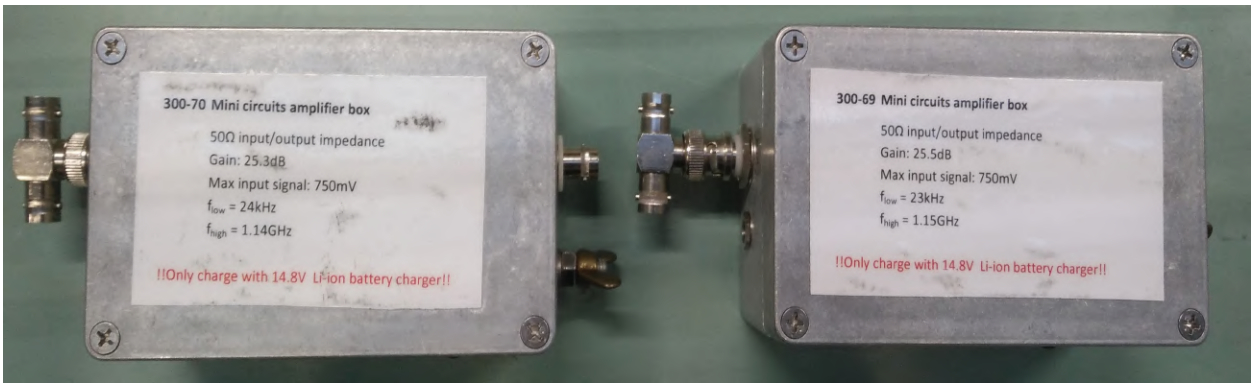

Figure 20: 300-70 and 300-69 Mini Circuits Amplifier boxes

4.3 Antenna Response

The time-domain and frequency response of the antenna are investigated. Several available amplifiers which are listed in Table 1 are compared. The time domain signals of the current of HFCT input and the voltage of the antenna output are measured using the TektronixMSO58 oscilloscope. It is processed in MATLAB and converted from the time domain to the frequency domain through a fast Fourier transform. After the frequency responses are computed, the transfer impedance can be calculated. The spectrum of the transfer impedance can be used to characterize the performance of the antenna in terms of bandwidth, and identify possible resonances. The transfer impedance ratio $H(f)$ is calculated using Equation 1,

$$H(f) = \frac{V_{OutputAntenna}(f)}{I_{InputHFCT}(f)} \tag{1}$$

where $V_{OutputAntenna}(f)$ is the output voltage measured by the antenna at specific frequencies and $I_{InputHFCT}(f)$ is the input current measured by the HFCT at specific frequencies.

The phase of the transfer function is also of interest to investigate the functioning of the magnetic detection. If the top and bottom loop of the antenna have a phase difference of 180 degrees, out of phase, the magnetic flux is detected. This is quickly observed by the top and bottom loop response being symmetric along the x-axis. A bode phase analysis is also suitable to check if the phase diverges from 180 degrees significantly. It is chosen to have an estimated margin of 35 degrees, when this is exceeded it can be concluded that the antenna is receiving electrical signals. As a result, using this parameter observation, it can be determined whether the antenna is functioning as desired.

To investigate the amplifiers, several attachments (PDF, inductive cores) are considered. The attachments are as follows and are also listed in the attachments column in Figure 25.

For the Femto amplifiers, a 115 nF input capacitance is always used to block to supply low-frequency noise as shown in Figure 21.

A PD Filter (PDF) is used to filter frequencies low frequencies below 116.8 kHz and those above 48.2 MHz which would suppress noise and possible undesirable higher frequency resonances (See Figure 22).

The inductive round cable snap-it core 0461164281 ("Core 42") and the round cable snap-it core 0461167281 ("Core 72") are tested as an attachment to investigate its effect on capacitive CM interference. The impedance profile of the cores are shown in Figure 23 and their placements on the antenna are shown in Figure 24.

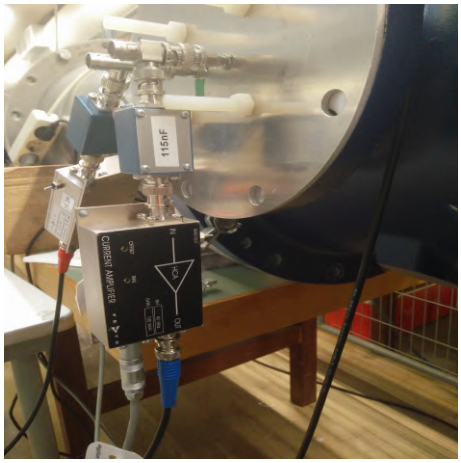

Figure 21: Femto 40M-100K Current Amplifier Connected to the 115nF Input Capacitance Connected to the Antenna in the Dielectric Window.

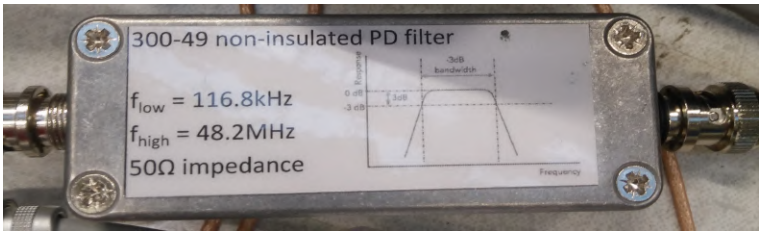

Figure 22: Partial Discharge Filter (PDF) Used

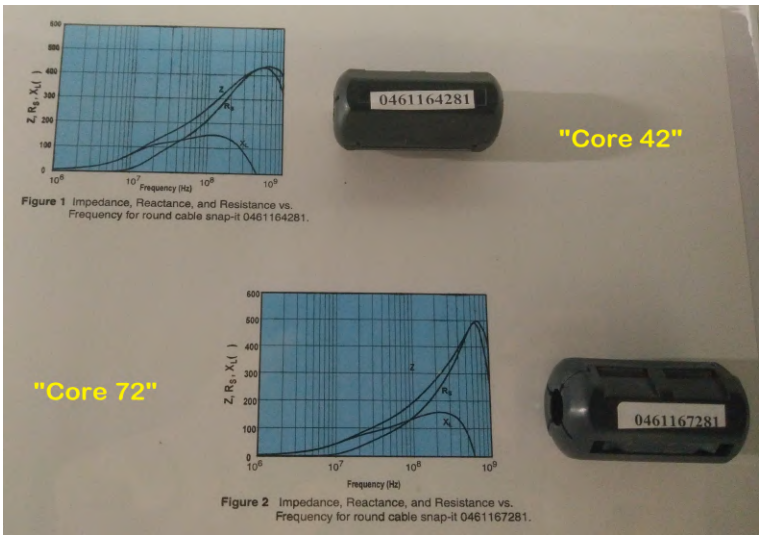

Figure 23: "Core 42" and "Core 72" Profiles

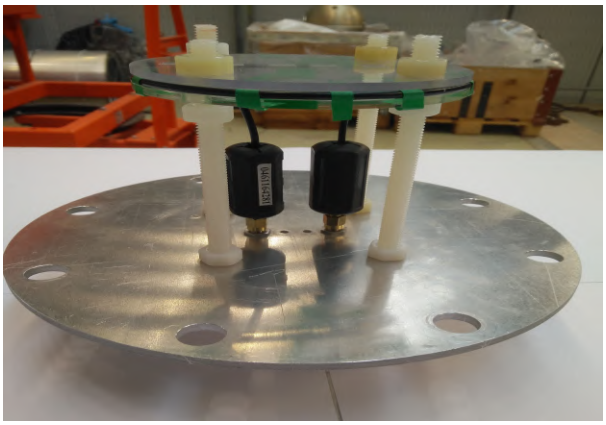

(a) Antenna with the Cores 42

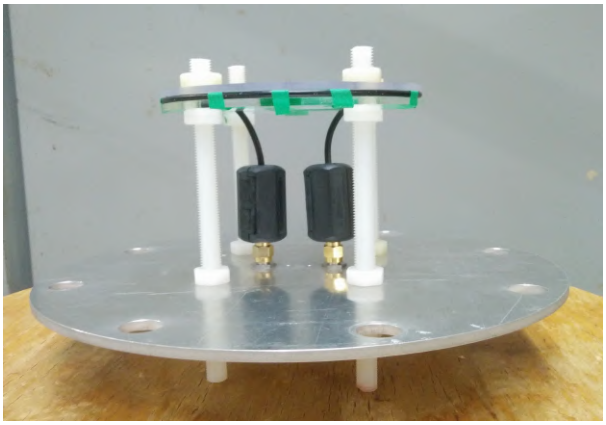

(b) Antenna with the Cores 72

Figure 24: Magnetic Antenna with Attachments

A structured overview of the considered cases of the amplifiers with the pulse generators and attachments for the antenna is provided in Figure 25. Measurements for the input/output and the bode plots are conducted. The bare amplifiers are included in this chapter with the other attachments included in the Appendix see Section A.1.

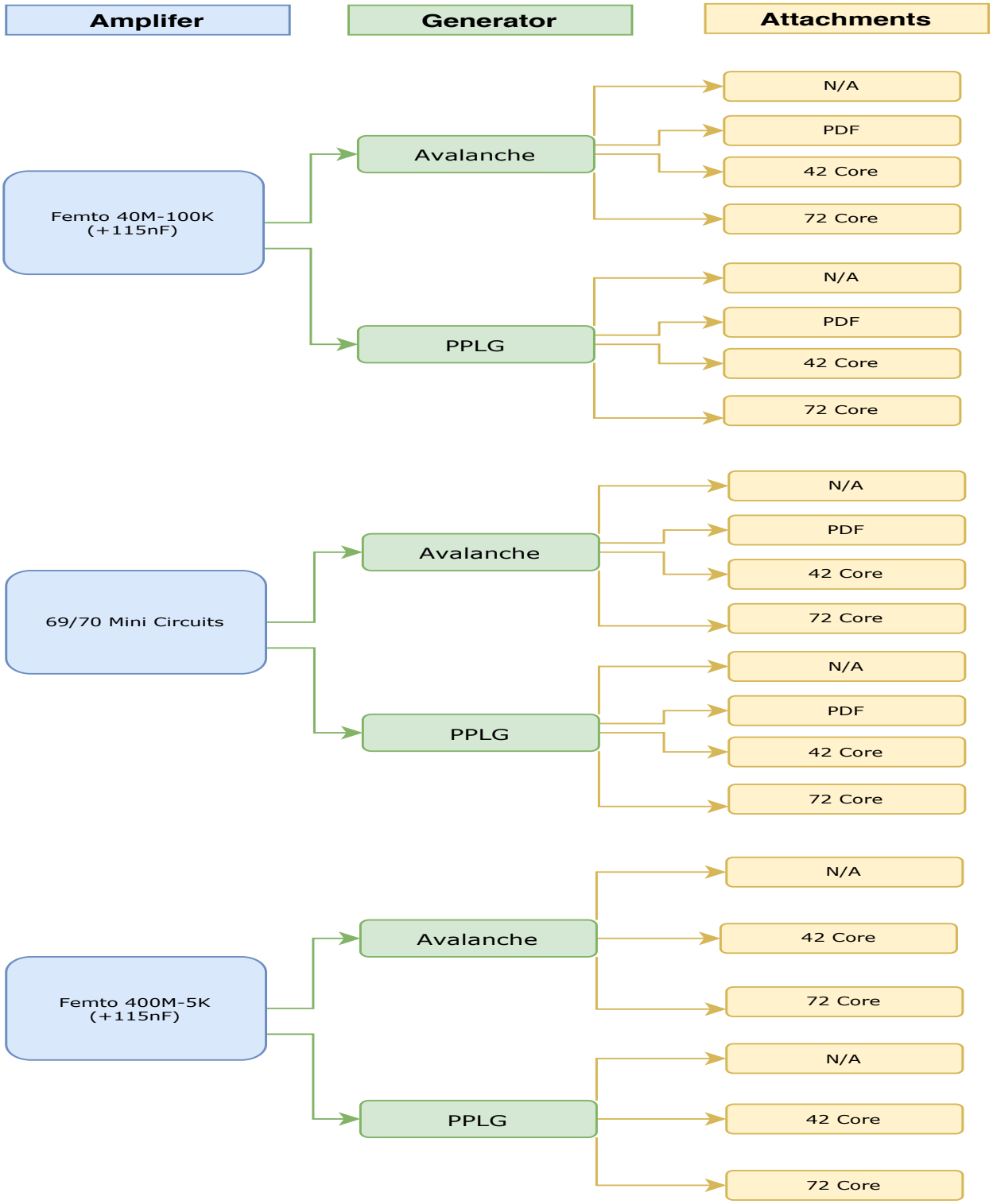

Figure 25: Overview of Investigated Amplifiers with the Possible Pulse Generators and Attachments

The measurements are conducted as in Figure 25. The base amplifier input/output and bode plots with the PPLG are included in the main thesis (See Figures 26, 27, 28, 29, 30, and 31) due to their clarity and relevance. All of the other measurements are included in the Appendix, see Section A.1.

Femto 40M-100K

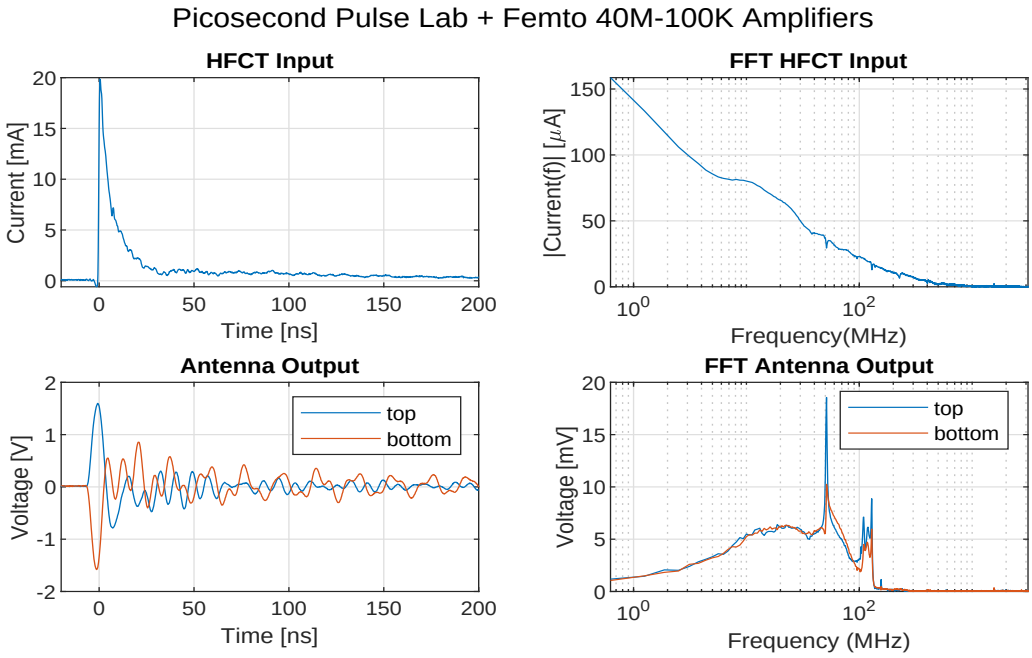

Figure 26: HFCT and Femto 40M-100K Amplifier Top and Bottom Loop Time Domain and Frequency Response of Magnetic Antenna to PPLG Pulse

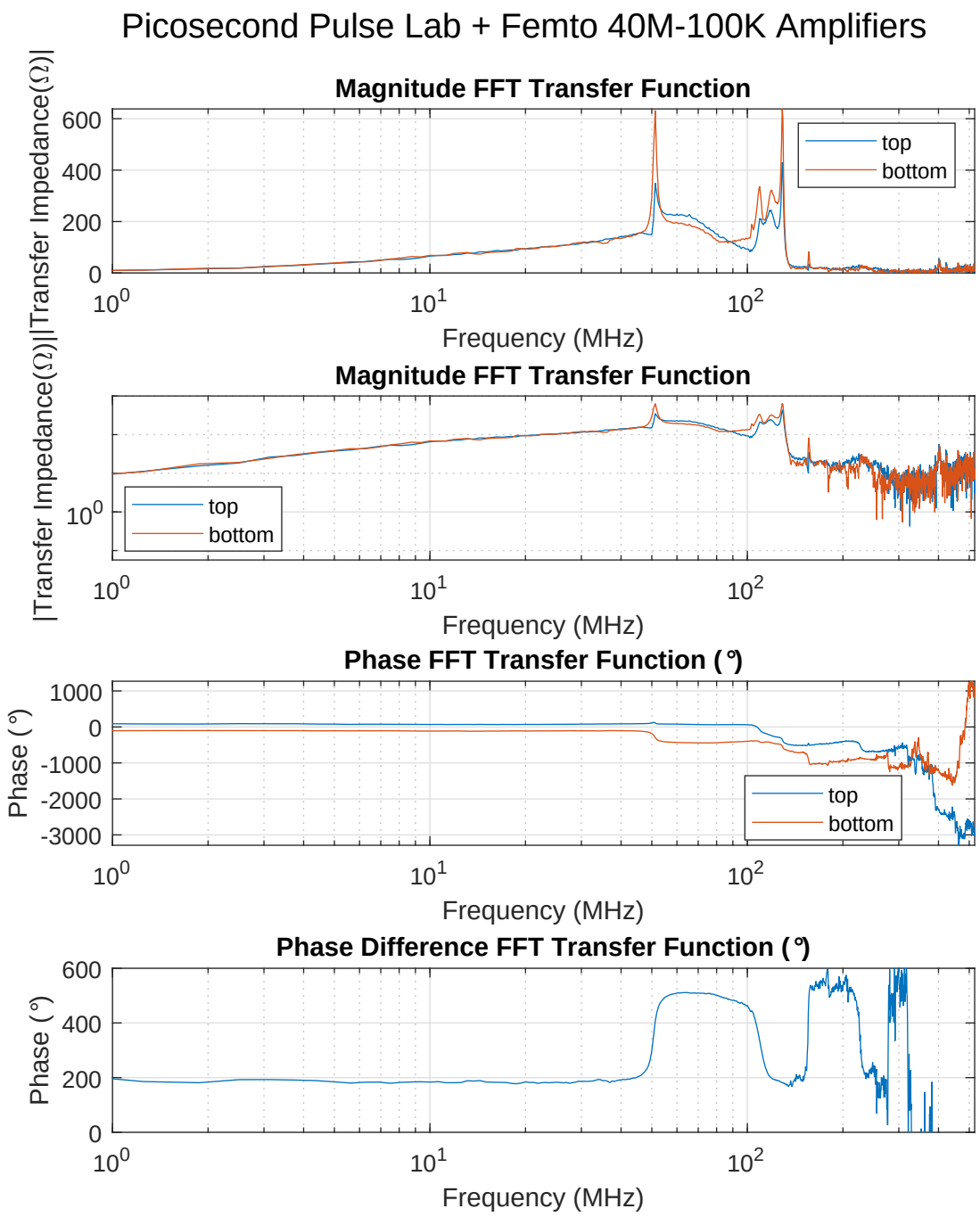

Figure 27: Femto 40M-100K Amplifier Amplifier Bode diagram of Magnetic Antenna loops.

70/69 Minicircuits Amplifier

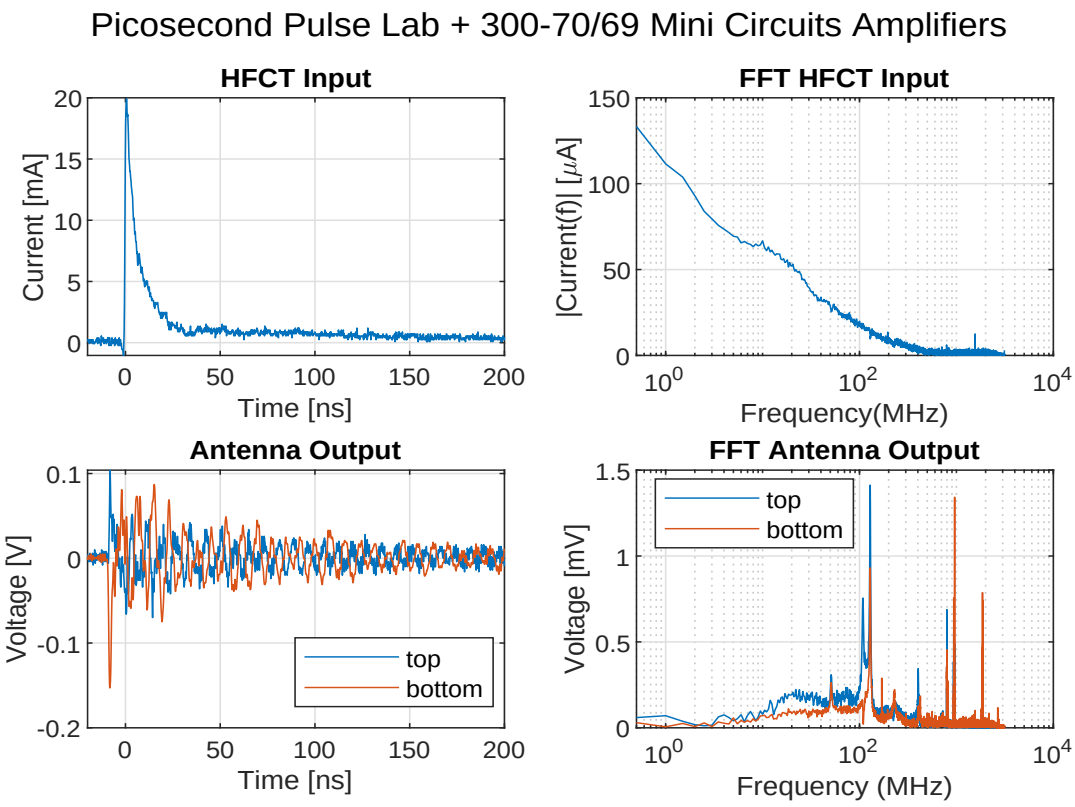

Figure 28: HFCT and 300-70/69 Mini Circuits Amplifiers Top and Bottom Loop Time Domain and Frequency Response of Magnetic Antenna to the PPLG pulse

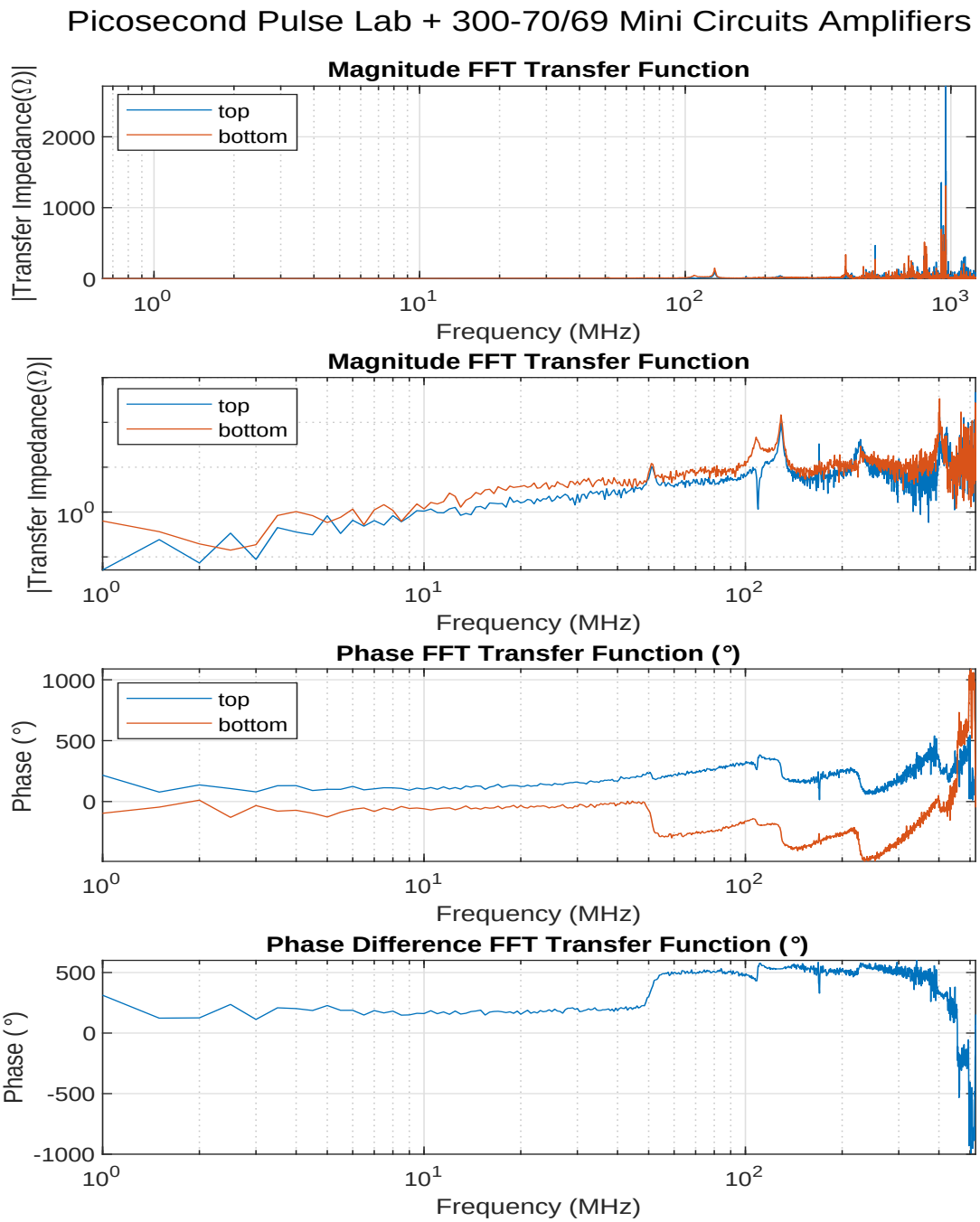

Figure 29: 300-70/69 Mini Circuits Amplifiers Bode diagram of Magnetic Antenna loops.

Femto 400M-5K

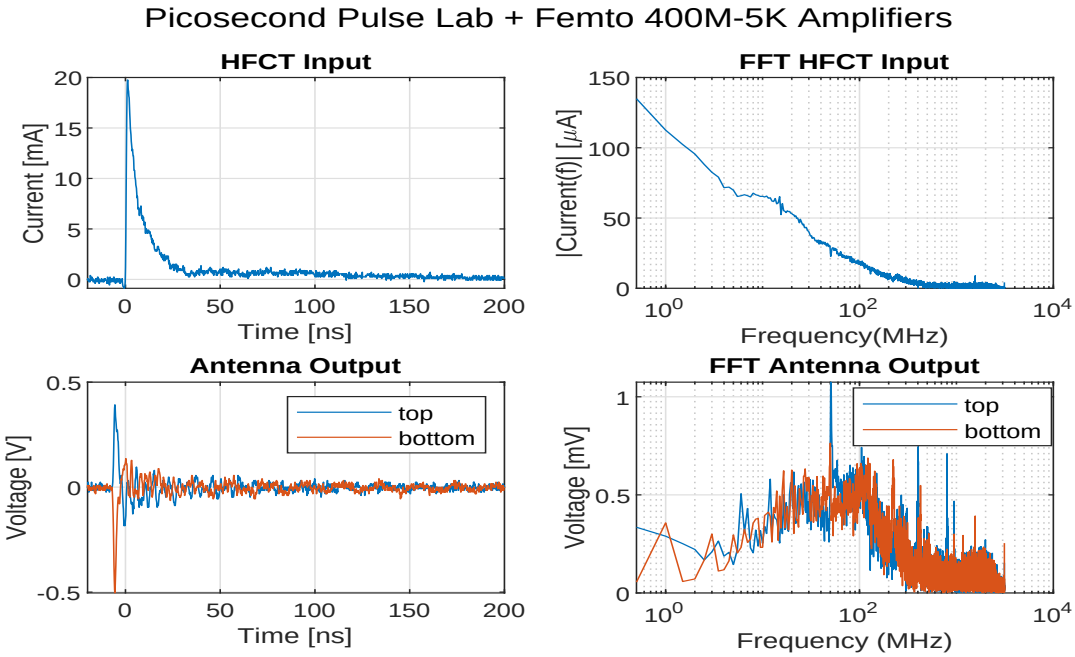

Figure 30: HFCT current (input) and 300-70/69 Mini Circuits Amplifiers Magnetic Antenna voltage (output) measurement in time domain and frequency domain for the top and bottom loop Response to the PPLG Pulse

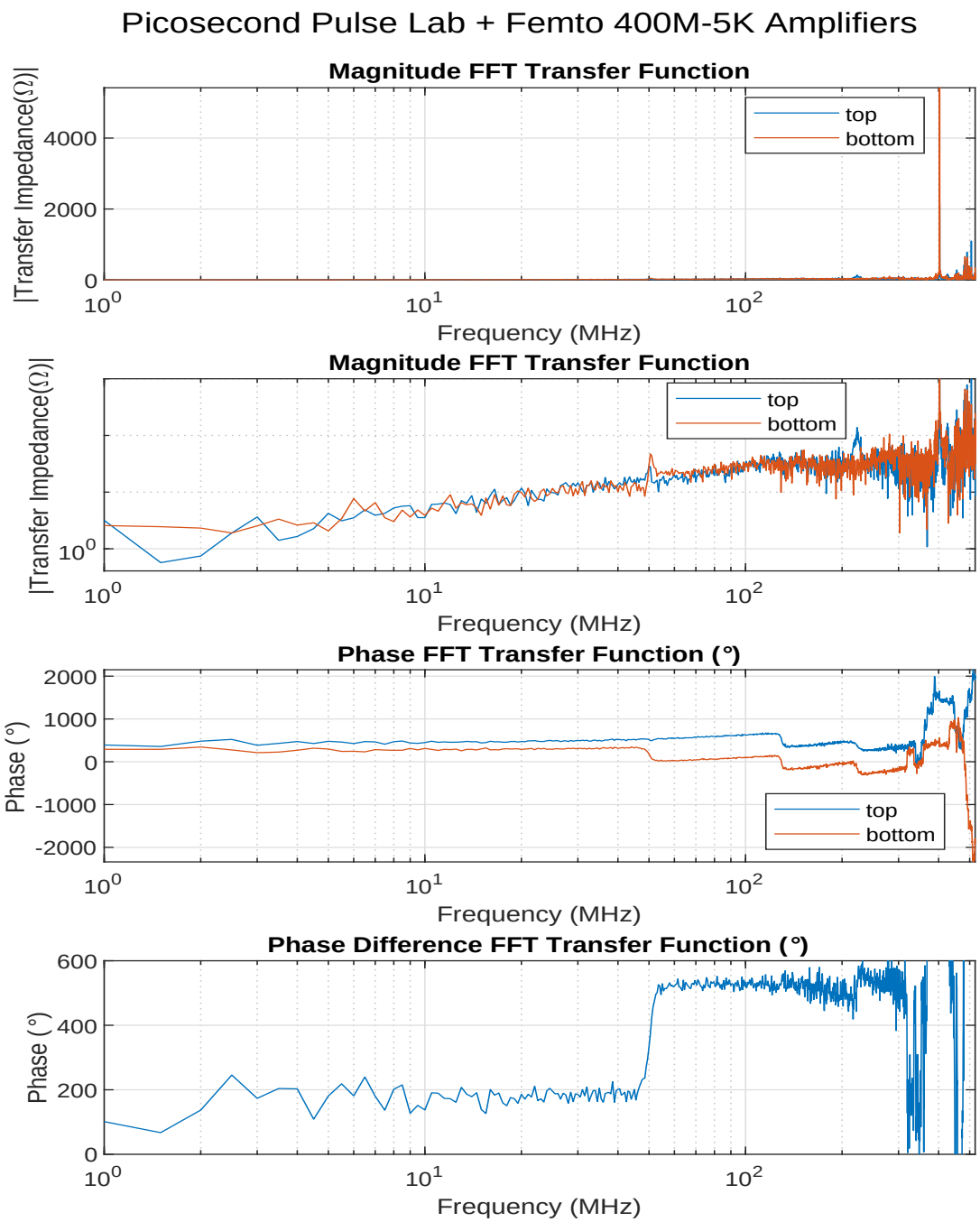

Figure 31: Frequency range until 250MHz of Mini Circuits Amplifier Bode diagram of Magnetic Antenna loops.

4.4 Comparison Top and Bottom Loops with and without Cores

From the frequency characterization measurements, the influence of the cores are investigated. This subsection specifically juxtaposes the plots of the amplifiers with three cases. The "Cap" case is the Femto Amplifiers with the 115 nF capacitor. The capacitor is always used for the Femto Amplifiers. For the Minicircuits, it is bare (without input capacitance). As such the core 42 and core 72 are used accordingly with or without the input capacitor depending on the amplifier choice. The data points are overlaid for a direct comparison of the core's behaviour for both the top and bottom loop. This way conclusions can be drawn about the influence of the cores. All of the comparisons are included in the Appendix in Section A.4. The PPLG plots are included in the main body as shown in Figures 32, 33, 34, 35, 36, and 37.

4.4.1 Femto 40M-100K

Picosecond Pulse Generator

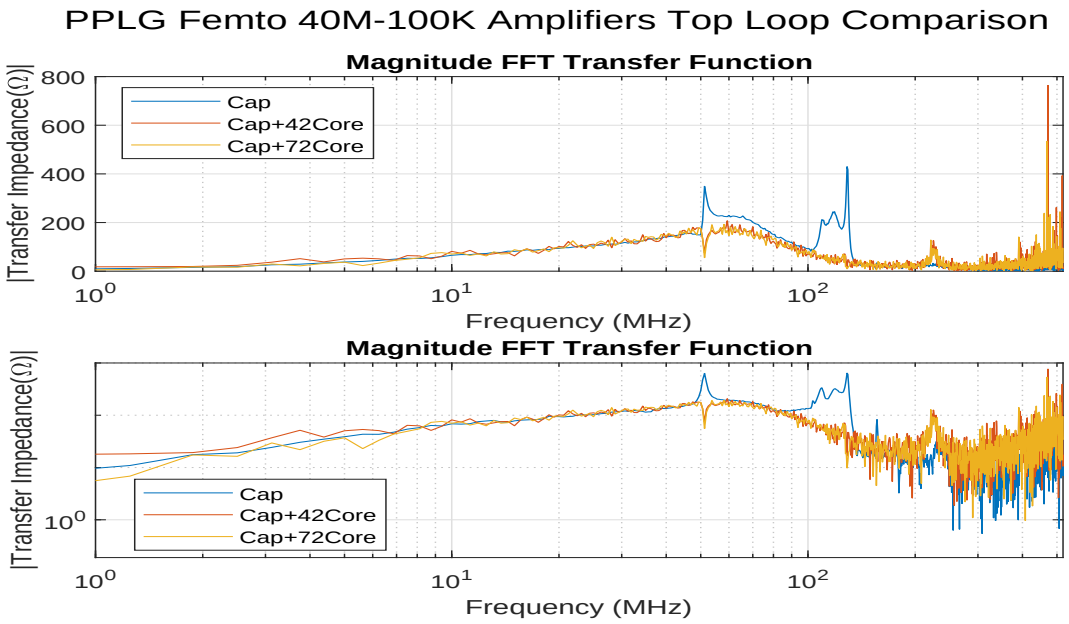

Figure 32: Comparing top loop transfer impedance of base, core42, and core 72 with the Picosecond Pulse Lab Generator and Femto 40M-100K Amplifier

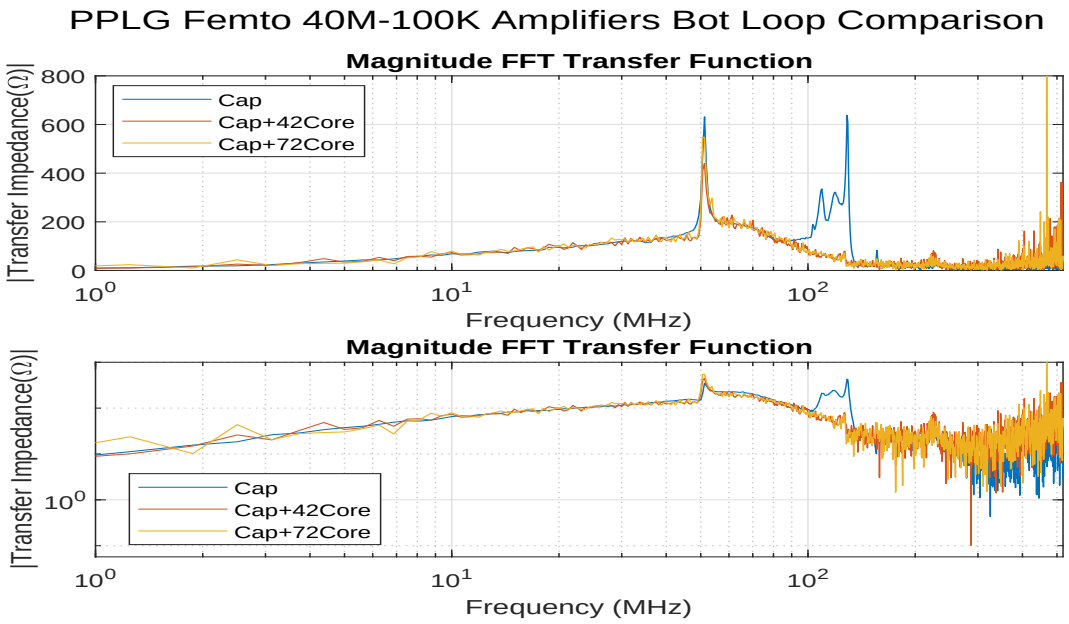

Figure 33: Comparing bottom loop transfer impedance of base, core 42, and core 72 with the Picosecond Pulse Lab Generator and Femto 40M-100K Amplifier

4.4.2 70/69 Minicircuits Amplifier

Picosecond Pulse Generator

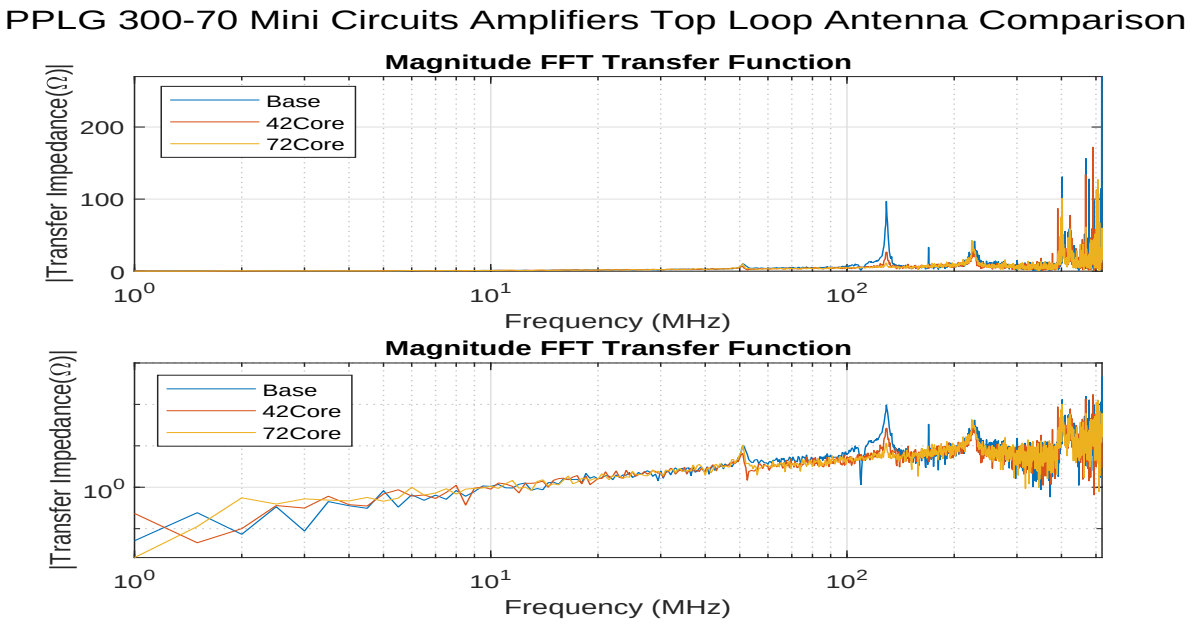

Figure 34: Comparing top loop transfer impedance of base, core 42, and core 72 with the Picosecond Pulse Lab Generator and 300-70 Mini Circuits Amplifier

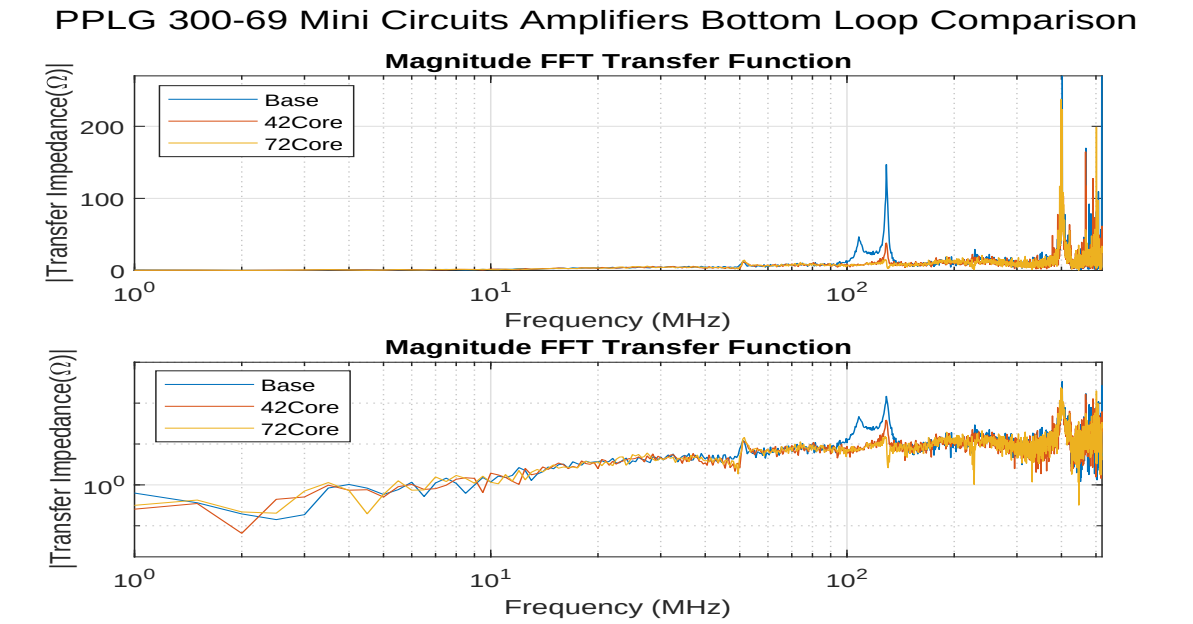

Figure 35: Comparing bottom loop transfer impedance of base, core 42, and core 72 with the Picosecond Pulse Lab Generator and 300-69 Mini Circuits Amplifier

4.4.3 Femto 400M-5K

Picosecond Pulse Generator

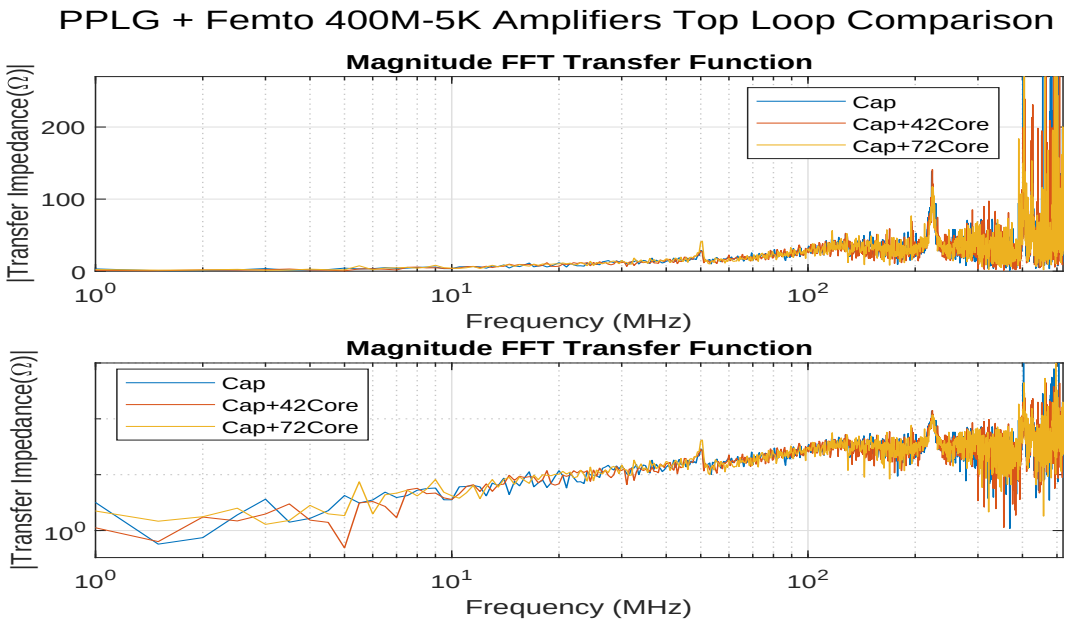

Figure 36: Comparing top loop transfer impedance of base, core 42, and core 72 with the Picosecond Pulse Lab Generator and Femto 400M-5K Amplifier

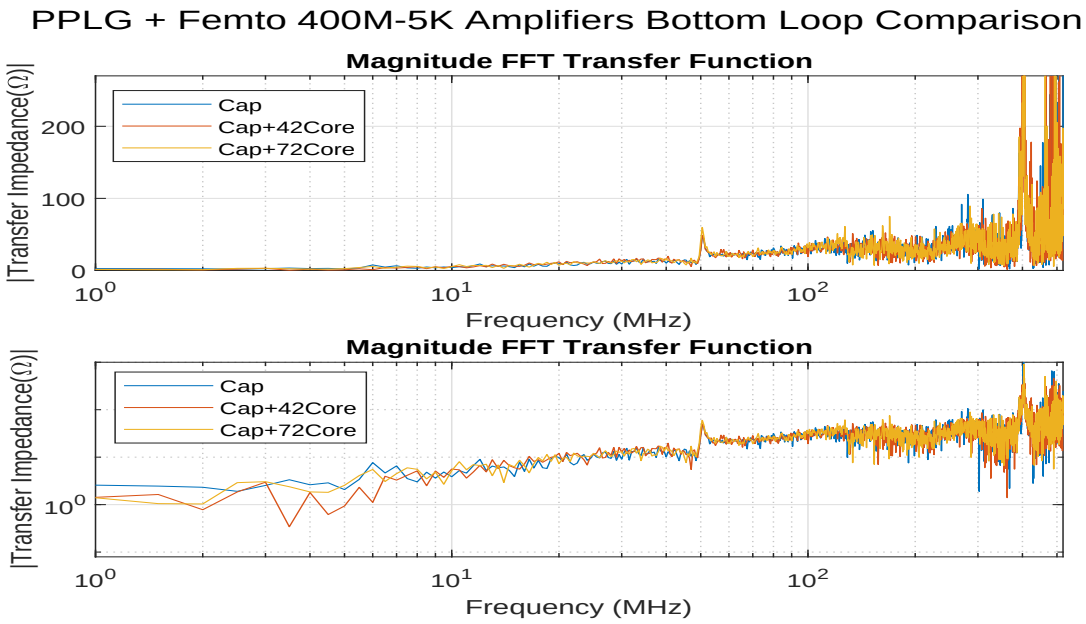

Figure 37: Comparing top loop transfer impedance of base, core 42, and core 72 with the Picosecond Pulse Lab Generator and Femto 400M-5K Amplifier

4.5 Analysis Antenna Response

From the frequency analysis of the Femto 40M-100K (with 115 nF), 70/69 Minicircuits and the Femto 400M-5K amplifiers (with 115 nF), it is apparent that there is a resonance occurring with peaks(s) between 105 and 130 MHz. It is suspected that this is due to a CM current path caused by a stray coupling capacitance in the antenna components and surrounding metal plates and surfaces. To verify if the cause is the CM resonance, an inductive core can be clamped around the straight end portion of the cable connected to the SMA adaptor. The reasoning is that the inductive effect could compensate the influence of the capacitive paths and mitigate the CM current influence. Using this concept, several cores were investigated with the core 42 profile and core 72 profile being considered in the thesis as shown in Figure 23 with the impedance profile. After applying the cores it is clearly evident from the figures displaying comparison of the cases with the core 42 , core 72 and base case that the CM is causing the second resonance.

The resonance peaks are quite apparent in the Minicircuits amplifier, this can be due to these amplifiers being more sensitive to external interference such as the CM noise. A plausible reason could be the poorer construction of the amplifier relative to the expensive and renown Femto amplifiers.

Observing that the CM is the culprit of the 110 MHz resonance peak and the assumption that the 51 MHz resonance peak was caused by the LC resonance, the subsequent conclusion is that adjustments can be made to the antenna design accordingly[1]. PCB designs are being explored which reduce the length of the cables and use other custom-designed amplifiers by DEMO (Dienst Elektronische en Mechanische Ontwikkeling). It can be concluded that the workbench is therefore suitable to characterize the antenna due it to its clean input with insignificant reflections. The clean input yields a clean output which is verified by averaging 30 responses to 30 pulses with the oscilloscope. After checking the performance of the antenna, the following step would be to test it on the GIS system by applying high voltage DC.

Resonance peaks:

1. LC Resonance and influence of HFCT around 51 MHz [2]
2. CM 105-130 MHz ; (It differs per amplifier slightly due to amplifier construction and design)

The Minicircuits is most sensitive to CM noise. A PCB antenna will be designed to push the LC resonance further and to reduce the stray coupling.

4.6 Antenna Amplifier Choice

As aforementioned in Section 4.3, amplifiers should ideally have a low input noise but particularly they should have a high gain and sufficient bandwidth (up to 300 MHz) for the HF range. Considering the trade-offs between the gain and the bandwidth, it was ultimately decided to select the Femto 400M-5K amplifier to be used in the GIS setup. The primary reasons were threefold. Firstly, and most importantly, the amplifier is able is to characterize the antenna in the intended frequency range. Secondly, it is hypothesized that with the higher bandwidth there would be more signal information that could characterize the pC charge value more accurately than when using a 50 MHz. This characterization of magnitude is important because unlike AC, where the phase gives information about the type of PD, for DC the magnitude of the discharge is available. In DC there is not a well-established pattern that can help in identifying the type of PD. For that reason, the charge plays an important role because it gives more information about the nature of the PD. Thirdly, the high bandwidth provides better resolution in the time domain. The 40 MHz gives a time

1 It was later discovered that the 51 MHz resonance was largely caused due to the influence of the HFCT and its grounding connection inside of the GIS. An idea to resolve the issue would be to decouple the measurement of the input and output. Essentially doing these measurements sequentially and separately. The FFT of an average of 100 input signals and 100 measurements of the output would be a reasonable estimate(a larger number of measurements can always be tested if desired). The ratio can be taken from these separate measurements for the magnitude in the Bode analysis.

2 Influence of HFCT, see footnote above

resolution of 25 ns whereas the 400 MHz provides a 2.5 ns resolution. This is useful for localization methods based on the time of arrival method (which are considered in Section 6.1) which translate time into distance using the wave prorogation speed in the medium. This hypothesis of using a larger bandwidth considers that future measures to be researched and implemented would ensure sufficient noise suppression as typically using a larger bandwidth would include more noise and thus could influence the value of the current integral resulting a deviating charge value.

4.7 Chapter Conclusions

The designed antenna is tested in the developed workbench. For the MA, resonances are detected. The peaks around 51 MHz are caused by the LC resonance and HFCT influence of the grounding. The 105-130 MHz peaks are due to the CM interference. This characterization provides valuable information to consider designing the next version of the MA. The chosen amplifier to be used is the Femto 400M-5K amplifier due to its appropriate bandwidth (for charge estimation and the HF range) and time resolution properties which will be valuable for localization. Overall, it was able to successfully characterize the MA with the workbench and investigate its frequency and phase behaviour.

5 GIS Setup

The chapter presents the 380 kV GIS setup at the Delft University of Technology High Voltage Lab. The diagram of the setup with the placement of defects and magnetic antennas are presented. Supporting electrical equipment and considerations of implementations are explored. This setup will ultimately be used for testing the localization capabilities of the setup.

5.1 Topology

The coaxial structure of the GIS provides a waveguide like environment for the PD pulse to propagate. This enabled the previous measurements and characterization of the antenna on the workbench. The workbench measurements were established in a straight GIS tank with cones to prevent reflections in order to properly characterize the antenna. In a GIS system applied in practice, there are several other considerations and compartments. There are other structural parts such as the L-shaped bend, T-shaped branch and various spacers. The GIS setup to be investigated in the TU Delft lab is more representative of a GIS system and thus will provide more meaningful insights which will be applicable in the future to the GIS in field if the measurement system is successful and appropriate for the use case.

The physical topology of the GIS system investigated in the laboratory is shown in Figure 38. The schematic map is shown in Figure 39.

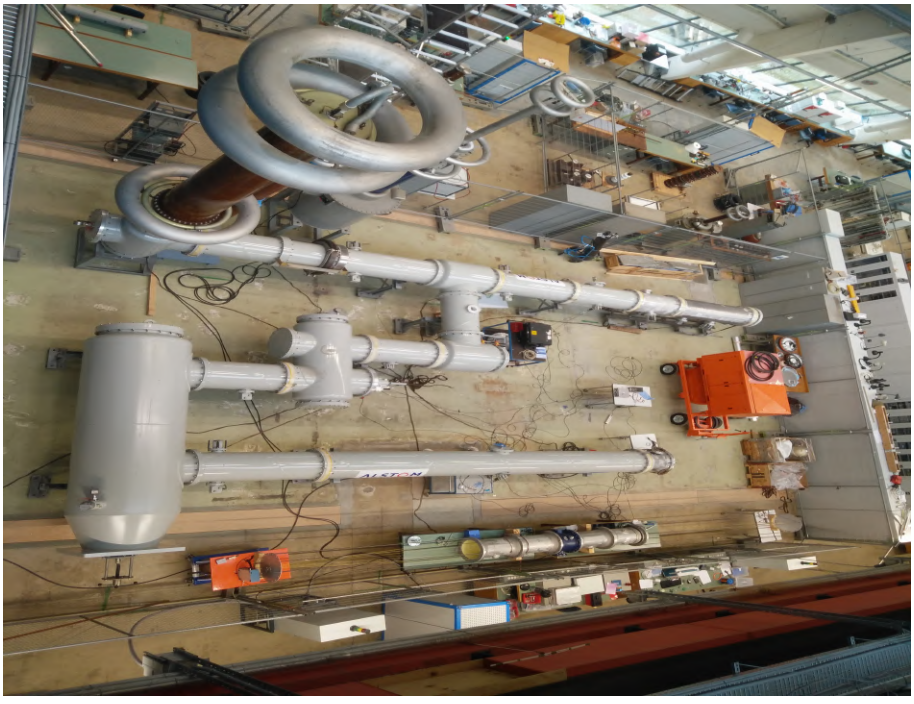

Figure 38: Aerial topology of the physical GIS System

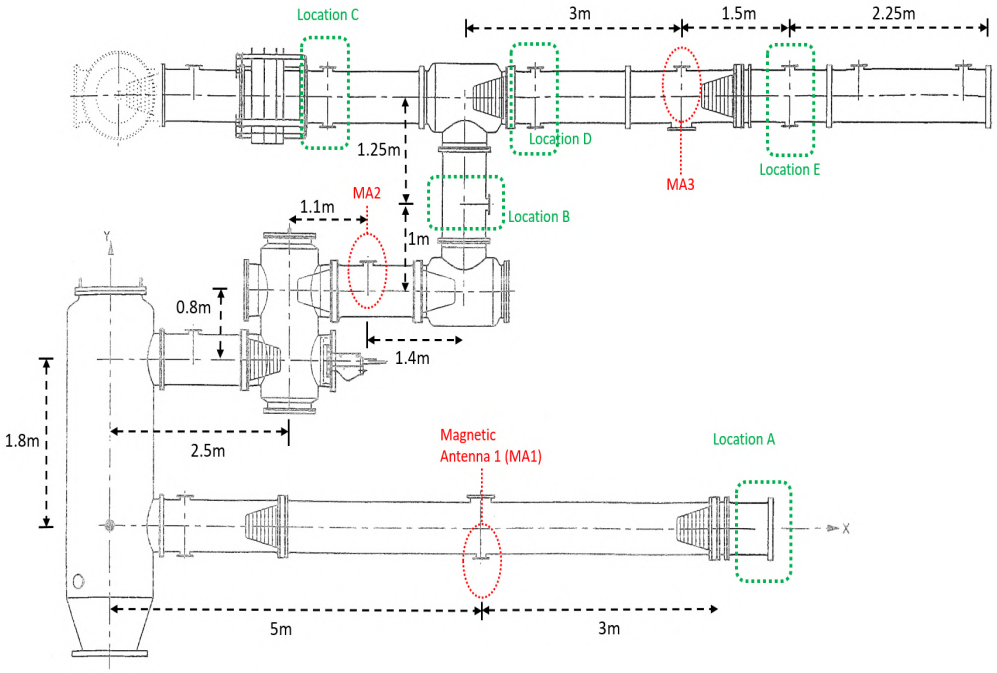

Figure 39: GIS Diagram with Magnetic Antenna (MA) and PD Source placements

5.2 GIS Setup Components and Considerations

The structure of components in the setup will have an impact on the EM propagation process of signals due to a change in transmission media. Factors such as attenuation, the widening of a pulse, reflections, and providing multiple paths for the signal to propagate will be conducive to influencing the behaviour of the pulse and thus what is detected by the magnetic antenna.

A brief overview of some structural components follows:

T Joints: As the name suggests, the T joint is shaped as a T. T Joints are used in a GIS to split the path of the inner components along two directions perpendicular to each other. This provides three extra paths, one reflection at the wall which the initial pulse is incident to and a path to the left and right branches of the T.

L-Bend: The L-Bend is shaped as an L and is designed to bend the construction of the path along a right angle. A reflection occurs here at incidence from the left as well as the pulse propagating at a right angle.

Spacers: Spacers are insulating supports used in the GIS. As the wave propagates through the coaxial structure it encounters the spacers on their path. These spacers could attenuate the signal and provide paths for stray current to flow.

Switchgear: The switchgear compartment is larger than the GIS straight tank components. This causes a change in characteristic impedance and thus reflections occur. Depending on the contents of the larger switchgear compartment, the wave will change as well.

Generation Section: A HVDC source is used and is connected to the bushing which is part of the GIS setup. -17 kV DC is applied to ensure the corona inception voltage is exceeded for the needle which is placed at different locations.

A brief overview of electrical equipment used follows:

Oscilloscope: The oscilloscope used should have a sufficient bandwidth, sampling frequency, and able to acquire data in a sufficient time frame. The oscilloscope used is the Tektronix MSO58. The sampling frequency used is 1.25 GS, with a bandwidth up to 2 GHz or 250 MHz if noise suppression at higher frequencies is desired, and the time frame of acquisition is set to 1.2 μs which is greater than the time needed to propogate from one end of the GIS to the other.

DC Voltage Source: A DC voltage source is used to supply 15 V to the 6 amplifiers which are used for the output of the magnetic antennas.

Amplifiers: For the Magnetic Antennas, the Femto 400M-5K is chosen. These amplifiers provide sufficient gain and cover a large bandwidth out of the aforementioned amplifiers available.

HV Generator: A Sorensen H.V. Supply 1101 is used to supply a DC voltage to the bushing for the GIS.

To structure the setup and provide a clear overview for its users several aspects were implemented. Labels were placed on the antennas and their cables which provided a clear and clean overview when connected to the oscilloscope. Moreover, careful wiring for the amplifiers and their 15 V DC source is implemented.

In terms of the antenna locations, three antennas were available due to limitation of the 6 amplifiers. Hence it was decided to spread them and place them in available dielectric windows as shown in Figure 39.

5.3 Antenna Modifications For the System

The magnetic antenna for the system is the same design as that which was tested on the workbench as shown in Figure 18. For practical reasons a readily available coaxial cable with a pre-soldered SMA connection is used. This allows for the antennas to be constructed faster due to the troublesome SMA pin soldering and also should mitigate human error in production providing a more consistent response. Slight modifications are therefore introduced however, this will not drastically change the antenna frequency characterization. This antenna is shown in Figure 40.

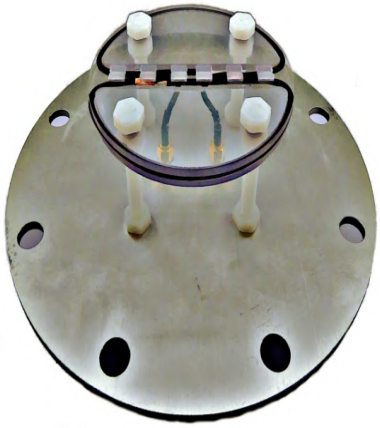

Figure 40: Antenna GIS with copper tape for connecting the ends of the individual loops

The magnetic antenna is inserted in the dielectric window of the GIS enclosure with a 2 mm clearance of

the antenna loop diameter with the inner walls. This enables the antenna to overcome the internal bump produced by the perimeter welding of the window pipe to the GIS compartment. The antenna diameter is 103 mm and the distance to the mounting plate is 53 mm.

5.4 Defects & Placements

5.4.1 Test Cell Charge Preparation

A test cell containing a sharp needle and SF6 Gas at 1 bar is prepared as shown in Figure 41. This test cell is placed at location A (see Figure 39). A voltage of -10 kV was sufficient to generate PDs.

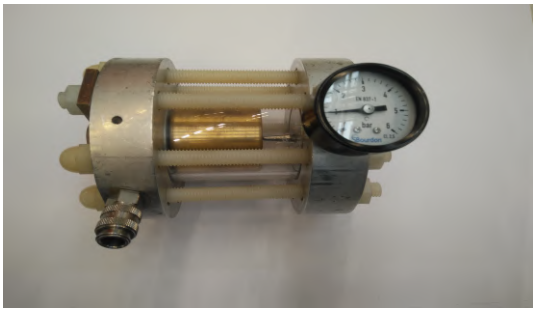

Figure 41: SF6 Test Cell with Needle

This test cell is created in preparation to check the sensitivity performance of the Magnetic Antennas. To check the apparent charge of the PDs generated by the test cell, the Bergoz HFCT (Model: FCT-016-5.0) is used. Data is processed with `PDFlex` software to inspect the value of the charge. The prepared SF6 test generated the majority of PDs in the range of 20-50 pC as shown in Figure 42. The magnitude of the discharge is dependent on the sharpness of the needle, with a sharper needle able to create finer discharges with a smaller magnitude. Ultimately, it is desired to check discharges in the order of magnitude of 5 pC. To achieve these smaller PDs, the needle can made sharper, used for shorter time intervals (or replaced more frequently), as the applied DC stress degrades the needle over time. The set up and cell was used for the charge estimation analysis on the charge magnitude and error in the CIGRE paper [3].

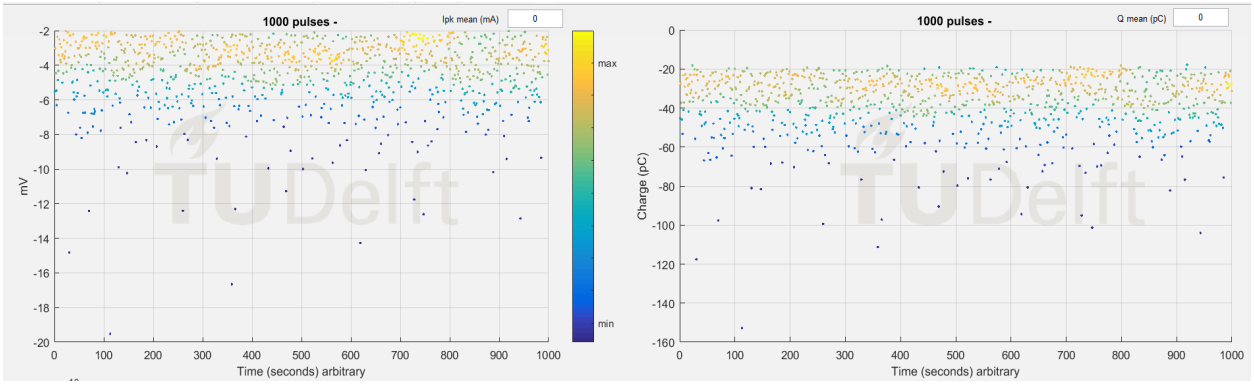

Figure 42: `PDFlex` Analysis of the magnitude of charge of the SF6 Test cell with the HFCT gain of 5 mV/mA and gain of 25.5 dB.

3 CIGRE Paris 2020 on "A NEW PARTIAL DISCHARGE MEASURING SYSTEM IN HVGIS BASED ON MAGNETIC FIELD ANTENNAS"

5.4.2 Corona Discharge Needle

A sharp needle is used to instigate corona discharges. It was observed that below -17 kV, PDs were observed on the oscilloscope through the magnetic antennas. The antennas measure the signal and it is stored on the oscilloscope. These measurements are acquired as the needle is sequentially placed in locations B, C, D and E as shown in Figure 39. An example pulse detected by the closest antenna (MA2) to the needle at Location B is shown in Figure 43 where the symmetric behaviour at the arrival of the pulse is apparent at 0.366 μs.

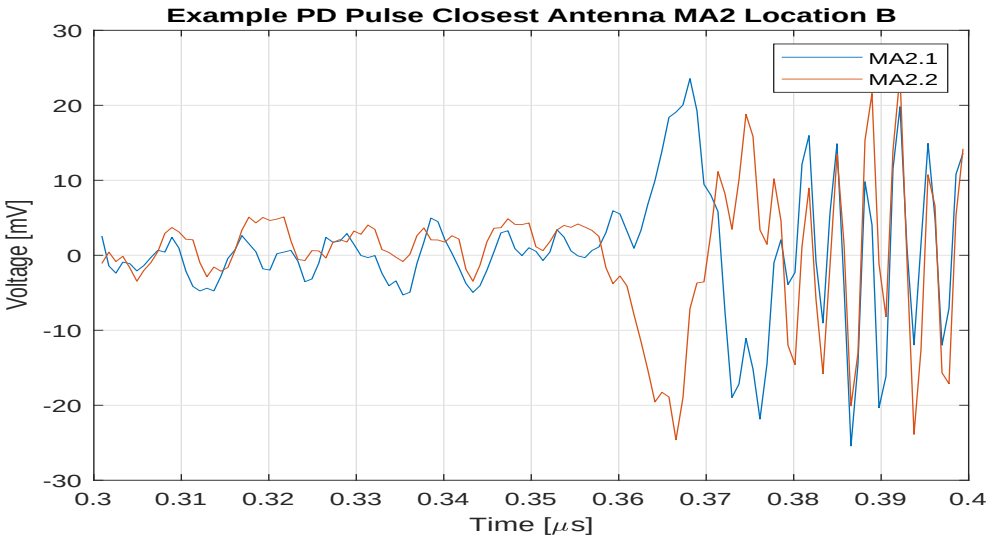

Figure 43: MA2 Response to example PD at Location B in the GIS Setup

5.5 Chapter Conclusions

The GIS setup is explained and the topology of it with the placed defects at specific locations is shown in Figure 39. Slight modifications were made to the MA for it to fit in the dielectric windows of the setup. A corona test cell is prepared and corona needles were placed in the GIS. An example of a PD at Location B detected by MA2 shows that the measurement system is functional and able to acquire the required pulses as is shown in Figure 43.

6 Algorithms for Partial Discharge Source Localization

To monitor the operation security of the GIS, PDs should be monitored. The localization of the PDs is essential in order to perform appropriate maintenance measures to maintain the operation security. Actions are taken based on the asset management policy which structurally decides and executes plans to optimize the balance between performance, efforts and risk. Localizing the PD provides information to the service providers where service is needed or may be needed.

Localization in the GIS is possible in both the longitudinal direction and the axial circumferential direction. For practical reasons, only the longitudinal direction is required to identify the compartment(s) involved. An accuracy of 1.5 m is desired to locate and thus isolate the smallest specific compartment.

Three methods are investigated and evaluated. The investigated methods are the:

1. Threshold Peak Detection,
2. Energy Criterion, and
3. Phase Method.

These methods all apply localization in the time domain. More specifically the time of arrival method (TOA) is applied as explained in Section 6.1.

In terms of data acquisition, 100 pulses are acquired for processing for both the top and bottom loop antenna.

6.1 Time of Arrival Method

The time of arrival method (TOA) is based on comparing the time difference between wavefronts arriving at two magnetic antennas which indicates the location of the PD source [20]. The concept is illustrated in Figure 44 where sensor 1 and sensor 2 are the two antennas closest to the defect.

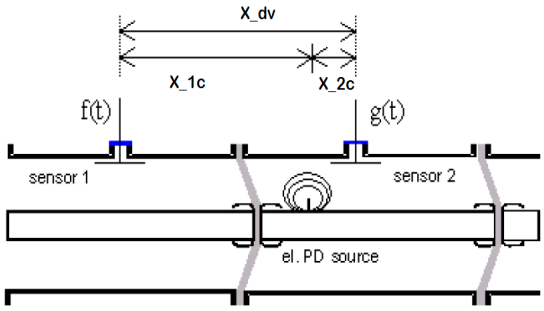

Figure 44: Longitudinal Section of GIS with TOA Concept Adapted from [20].

The distances of the defect with respect to the antenna are labelled x_{1c} and x_{2c} as shown in Figure 44. The TOA equations to calculate the distances are:

$$x_{1c} = \frac{x_{dv} - c \cdot \Delta T_{1c}}{2} \tag{2a}$$

$$x_{2c} = \frac{x_{dv} - c \cdot \Delta T_{2c}}{2} \tag{2b}$$

where x_{dv} is the pre-known (longitudinal) distance between the two antennas, c is the speed of light representative of the PD wave propagation speed in the GIS, and ΔT_{1c} and ΔT_{2c} is the difference in time of arrival difference between right and left sensor and difference between left and right respectively. *For the explanation, the terminology left and right are used to prevent ambiguity with the enumeration/number of the antennas.* The sign conventions for x_{1c} and x_{2c} are with respect to the localization defect, with left being negative and right being positive.

The implementation of the algorithm in MATLAB is elucidated in figure 45 with a subsequent elaboration of each step.

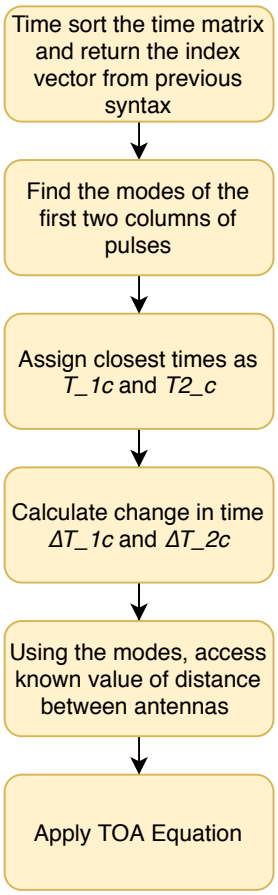

Figure 45: Flowchart Time of Arrival Algorithm

The three investigated algorithms output a time matrix which contains the information of the time of arrival at the Magnetic Antennas. With the time matrix, the elements are sorted in ascending order such that the first two times of the closest antennas can be extracted. Indices are stored which are representative of the number of the magnetic antenna (MA1, MA2 or MA3).

The time values of the two closest values are accessed from the time sorted matrix.

The time difference ΔT_{1c} and ΔT_{2c} is calculated as the difference in time of arrival between the right and

left sensor and difference between left and right respectively.

The previously stored index representing the number of the antenna is used to compute the mode of the indices for the first two columns of the sorted time matrix. The values are extracted so that the x_{dv} is also selected based on the two antennas. This is done after a conditional if statement based on the mode of the first two columns of the index time matrix.

Now that x_{dv}, ΔT_{1c} and ΔT_{2c} are known, the TOA equation, see Equation 2, is applied to calculate the distance of the defect from the antennas.

6.1.1 Limitations of TOA Method

With the three antennas used in 39, Location B and Location D are only able to be investigated as the defect has a magnetic antenna on both sides (the defect is between two sensors) which is a prerequisite for the TOA method. More antennas are required for monitoring of the PDs at different locations, or the antennas would have to be moved. [*Due to the unfortunate circumstances with COVID-19 it was not possible to explore all the locations. However, the algorithms are developed to be applicable to any location and can thus be investigated. A thorough analysis of Location B and Location D is therefore present in the report with the configuration of the antennas as shown in Figure 39.*]

Another limitation is that the accuracy of the TOA distance is limited by the resolution in time determined by the sampling frequency. A sampling frequency of 1.25 GS/s is used which when applying the speed of light for propagation of a wave, translates into a longitudinal distance resolution of 0.23 m. This is more than sufficient for the intended 1.5 m specification as aforementioned.

6.2 Threshold Peak Detection

The implementation of the Threshold Peak Detection (TPD) method algorithm in MATLAB is elucidated in Figure 46 with a subsequent elaboration of each step. The left path in the flowchart is the preprocessing and training of the parameter to set the threshold level. The right path is applying the TPD calculations using the pretrained threshold value as input.

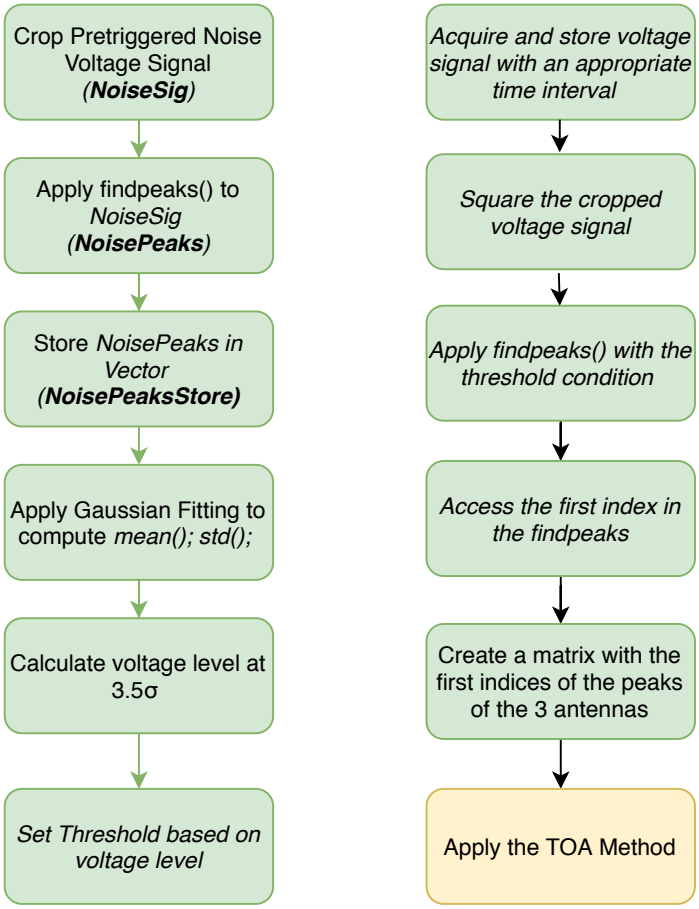

Figure 46: Flowchart Threshold Peak Detection Algorithm, left flow path is for preprocessing, the right flow path is the live process.

The TPD method sets a voltage threshold which if a local maxima exceeds this value, a PD pulse is detected. The time index of the first peak which exceeds the threshold is accessed and then the TOA method is applied.

TPD Pretraining Threshold Value (left flow path):
Firstly, the measurement acquired at the oscilloscope is cropped before the trigger of the pulse. This cropped region is representative of the noise of the signal.

The `findpeaks()` function is applied to the cropped noise signal. This returns the values of local maxima of the noise.

The values of the peaks from `findpeaks()` are stored in a vector for further processing.

A gaussian analysis is conducted on the stored value of the peaks. This is because the noise appears to be additive gaussian white noise and is representative of the peak magnitude. The fitting computes the mean and standard deviation of the vector storing the peaks of the noise.

The upper voltage level of the noise (which will be the lower threshold of the signal, which when exceeding it will register the signal as a PD) is computed at $3.5\,\sigma$ away from the mean. This ensures that 99.98% of voltage values from the peaks of the noise are below the threshold.

The threshold is set based on the voltage level received from the gaussian analysis. This value can be then used as a pretrained value to speed up the overall algorithm, rather than calculating the threshold every time before running the right flow path in Figure 46.

TPD Live Process (right flow path):
The acquired voltage signal from the antennas is cropped. This is done to limit the time interval in order to reduce the number of data points that need to be processed which as a result reduces the time required for computations. The cropped time interval is [0.35 0.5] μs. The begin time is just before the trigger at 0.38 μs. The end boundary is determined by translating the maximum possible distance a wave can propagate in the GIS, with a margin, into time using the speed of light as the propagation speed. This distance is 24.6 m with a large margin of 20 m in case reflections are of interest in subsequent analysis and thus results in 0.15 μs. The interval can easily be reduced to reduce the data points by instead applying a margin of 10 m. However, the computation times of the algorithms were in the order of minutes, and thus it was deemed unnecessary.

The cropped voltage signal is squared. This enables the PD pulse peaks to be clearly distinguished from the noise peaks due to the quadratic multiplicity causing a greater difference between the PD peak and noise peak. As a result, the threshold which will be set is less likely to be exceeded by noise.

The `findpeaks()` function is applied, with a threshold condition which is the value determined by the TPD Pretraining, to the cropped voltage signal containing the PDs. This returns the values of local maxima of the peaks.

Access the first index in the `findpeaks()`. This first index (x-axis, representing time) represents the value of when the PD has arrived as it has exceeded the threshold value (y-value, voltage).

The data is stored in a time matrix with the first time indices of the 3 antennas from the previous access. This is done for all the 100 pulses.

Once this matrix is created, apply the TOA method as outlined in Section 6.1 to calculate the distance of the defect from the antennas. The distances resulting from the top and bottom loop for a specific antenna can also be averaged for further interpretation.

6.2.1 Results

Location B and Location D are tested.

An example PD pulse is shown in Figure 47. The cropped signal is shown in Figure 48 and the squared signal to help distinguish the PD peak from the noise peak is in Figure 49.

A histogram analysis is conducted with bins corresponding to the resolution in distance from the sampling frequency of 1.25 GS/s. This is the reciprocal of the sampling frequency multiplied by the speed of light which ensures a resolution of 0.23 m. The histogram analysis for the top antenna pair (two closest to defect as outlined in the TOA method see Section 6.1), as well as, the bottom pair is shown in Figure 50 and Figure 51 respectively. To combine the use of the two available loops, an average is also calculated and plotted in Figure 52.[4]. The results of the average distance from the defect for the 100 pulses is summarized in Table 2.

Location B
An example PD pulse is shown in Figure 47. The cropped signal is shown in Figure 48 and the squared signal to help distinguish the PD peak from the noise peak is in Figure 49.

A histogram analysis is conducted with bins corresponding to the resolution in distance from the sampling frequency of 1.25 GS/s. This is the reciprocal of the sampling frequency multiplied by the speed of light which ensures a resolution of 0.23 m. The bins represent the difference in the actual location of the PD and the distance the algorithm resulted in. The histogram analysis for the top antenna pair (two closest to defect as outlined in the TOA method see Section 6.1), as well as, the bottom pair is shown in Figure 50 and Figure 51 respectively. To combine the use of the two available loops, an average is also calculated and plotted in Figure 52. The results of the average distance from the defect for the 100 pulses is summarized in Table 2.

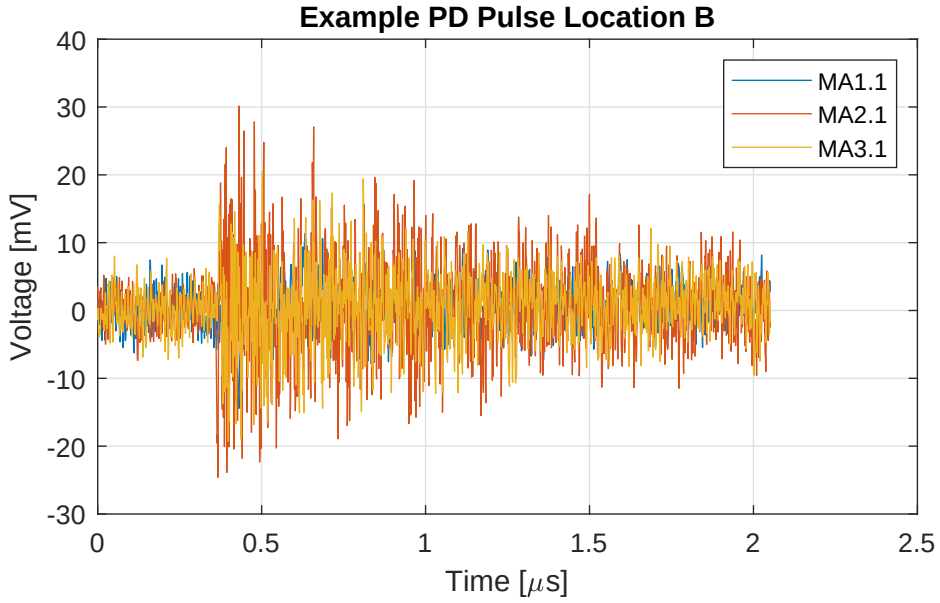

Figure 47: Top Antenna Responses to 1 of the 100 PD pulses acquired - Location B

4 The full-scale Histogram plots are shown in the Appendix A.6 due to the variance in a few outlier data points caused by abnormal noise levels causing the scaling the plot not to fit in the main section of the thesis.

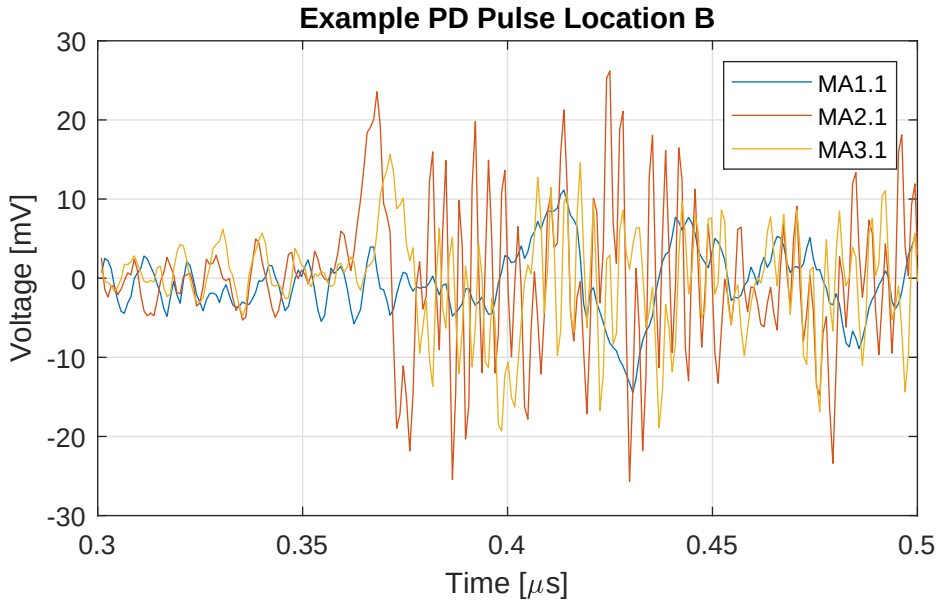

Figure 48: Time cropped signal including pretrigger of the Top Antenna Responses to 1 of the 100 PD pulses acquired - Location B

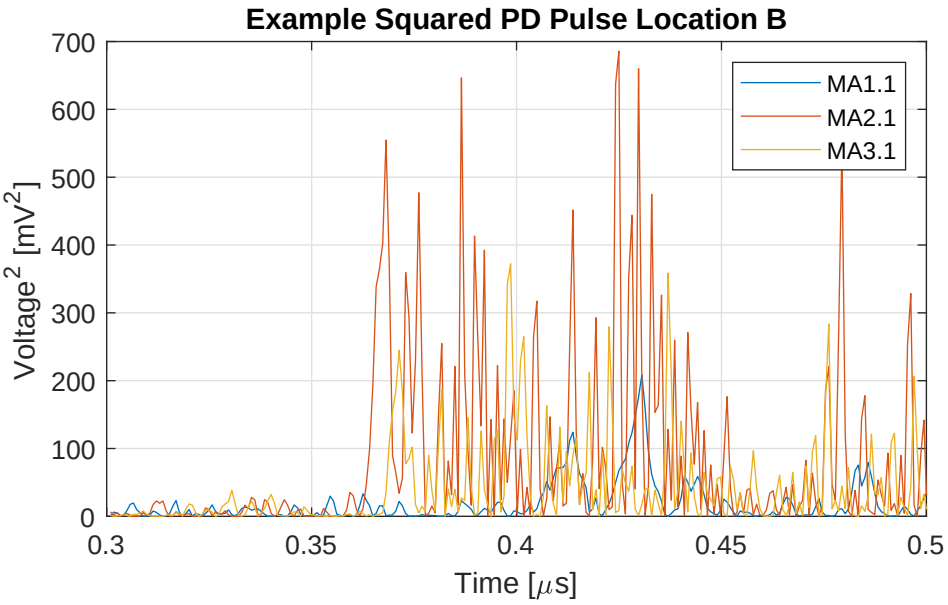

Figure 49: Squared Time cropped signal of the Top Antenna Responses to 1 of the 100 PD pulses acquired - Location B

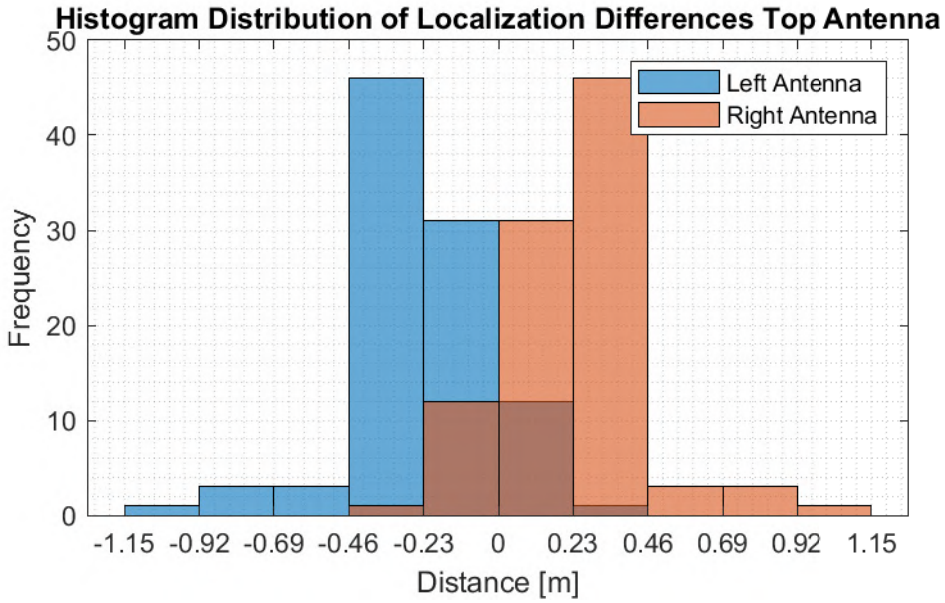

Figure 50: Histogram of Distance Distribution of Top Antenna for the TPD Method - Location B

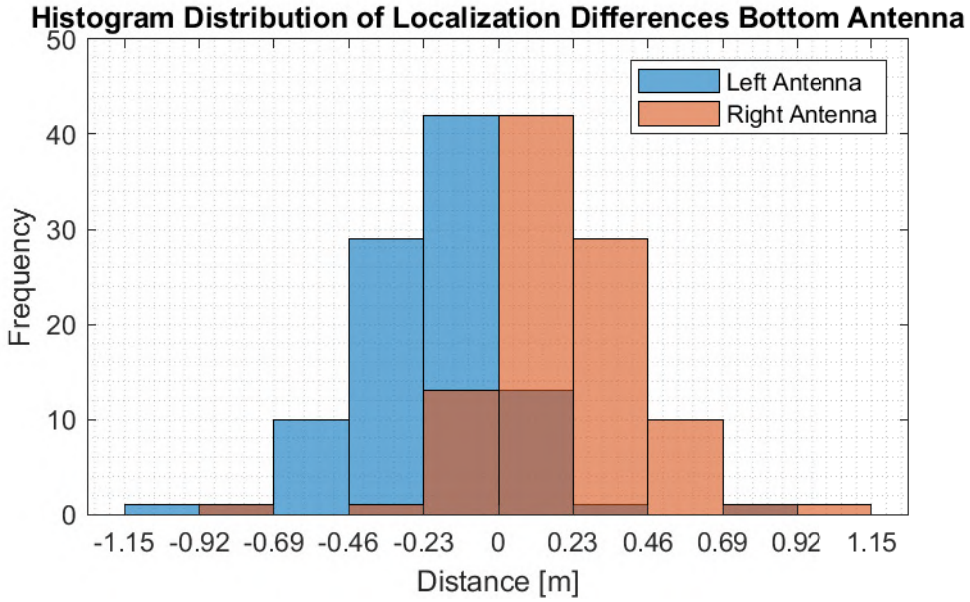

Figure 51: Histogram of Distance Distribution of Bottom Antenna for the TPD Method - Location B

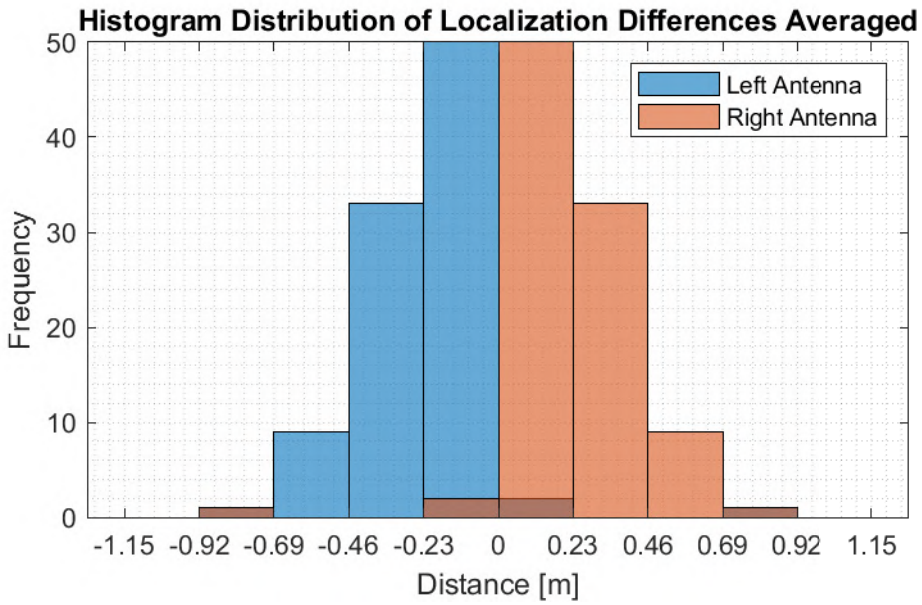

Figure 52: Histogram of Average Distance Distribution of the Top & Bottom Antenna for the TPD Method - Location B

Table 2: Summary of average distance from the defect for the 100 pulses of the top loops, bottom loops and the average of the top and bottom loop applying the TPD algorithm. - Location B

	Distance (m)
Top Antennas	0.12
Bottom Antennas	0.16
Average of Antennas	0.14

Location D

The histogram analysis for the top antenna pair (two closest to defect as outlined in the TOA method see Section 6.1), as well as, the bottom pair is shown in Figure 53 and Figure 54 respectively. To combine the use of the two available loops, an average is also calculated and plotted in Figure 55. The results of the average distance from the defect for the 100 pulses is summarized in Table 3.

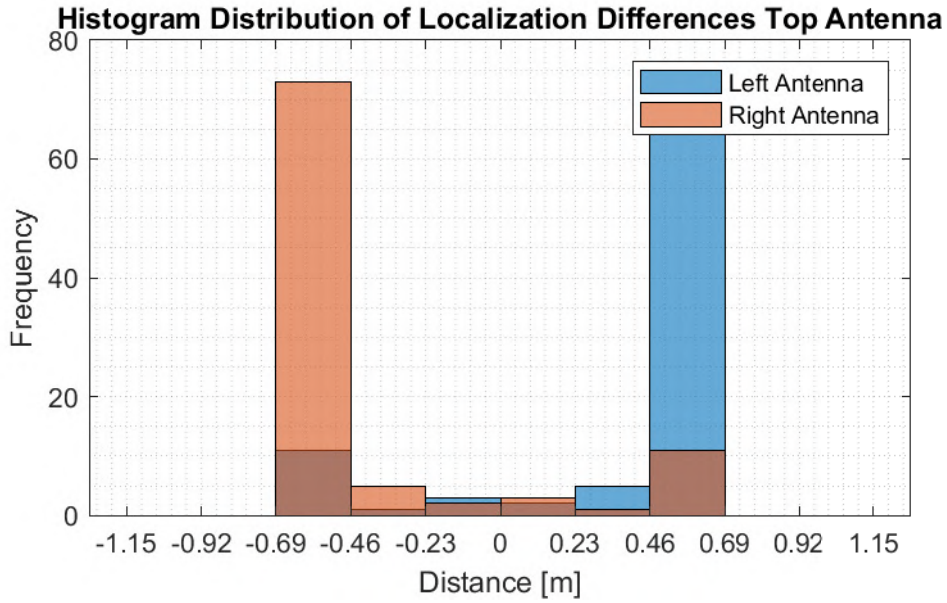

Figure 53: Histogram of Distance Distribution of Top Antenna for the TPD Method - Location D

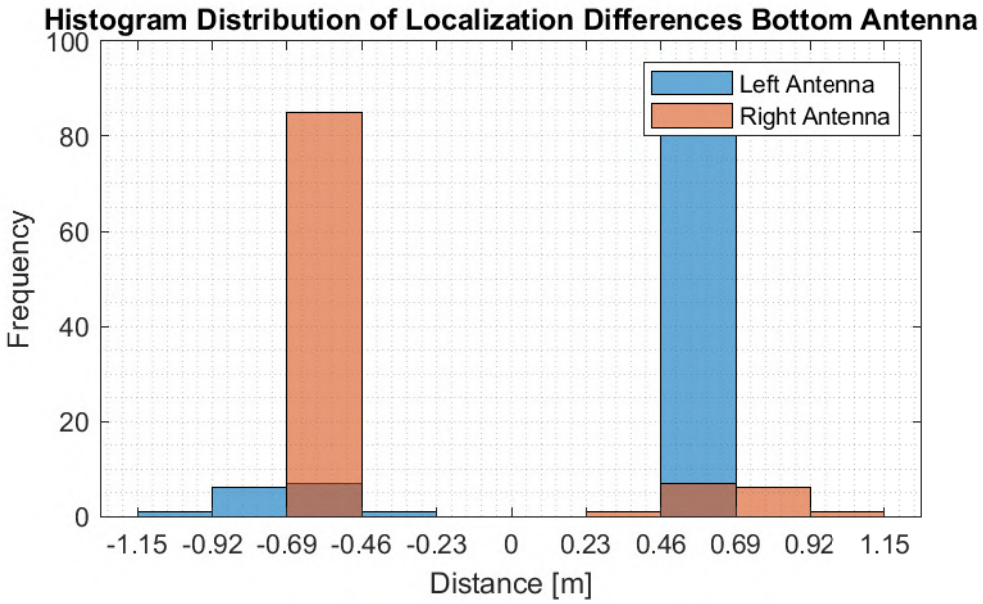

Figure 54: Histogram of Distance Distribution of Bottom Antenna for the TPD Method - Location D

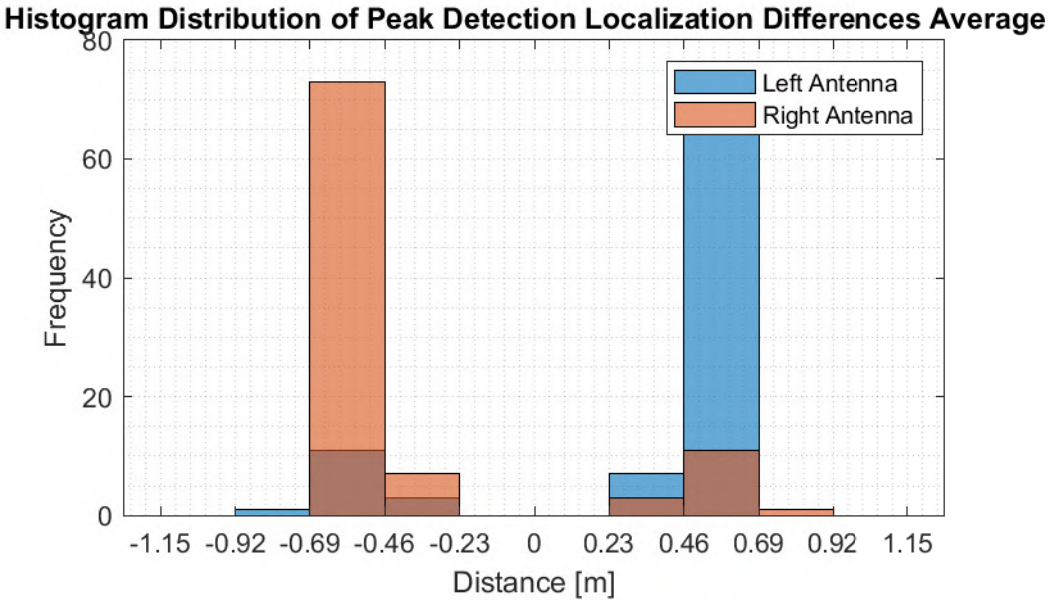

Figure 55: Histogram of Average Distance Distribution of the Top & Bottom Antenna for the TPD Method - Location D

Table 3: Summary of average distance from the defect for the 100 pulses of the top loops, bottom loops and the average of the top and bottom loop applying the TPD algorithm. - Location D

	Distance (m)
Top Antennas	0.64
Bottom Antennas	0.35
Average of Antennas	0.50

Runtime

The MATLAB Profiler is used to determine the execution time of the program. For all of the algorithms, the same number of data points are used (cropped signal) and the same time consuming `saveas` *statement is used to store the histogram of the average distance distribution. Time optimizations could have been made by for example preallocating vectors before for loops but the idea is to get an order of magnitude estimation as a comparison between the methods.*

The runtime for the TPD method is 15.0 seconds. This is a reasonable execution time and the order of magnitude less than a minute is not of concern.

6.2.2 Method Conclusions

Several pros and cons have been identified during the process of implementing and observing the results. These are:

Pros

- Simple Algorithm and Implementation
- Location B: 95 % of measurements within 1.5 m requirement.

- Location B: Average difference between defect and localization is 0.14 m
- Location D: 95 % of measurements within 1.5 m requirement.
- Location D: Average difference between defect and localization is 0.50 m
- Appropriate runtime of 15.0 s.

Cons

- High sampling synchronization required.
- Resolution is limited by sampling frequency.
- Low noise environment is desired, at least a 2x gain of PD vs background noise is desired.
- Peaks are subject to inaccuracies caused by noise.
- Pretraining is required to set the threshold.
- Requires the TOA method which requires two antennas and the defect should be between the antennas.

6.3 Energy Criterion

The implementation of the Energy Criterion (EC) method algorithm in MATLAB is elucidated in Figure 56 with a subsequent elaboration of each step.

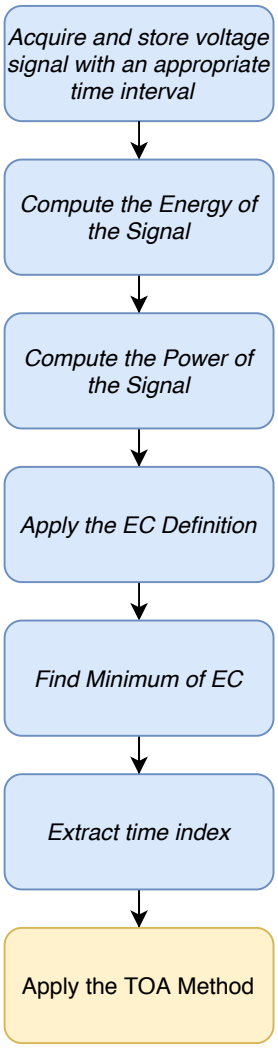

Figure 56: Flowchart Energy Criteria Algorithm

The EC concept revolves around the concept that the arrival of a pulse causes a change in energy relative to the base energy level. The EC method finds the minima and then accesses this value to be used for the TOA method.

The voltage signal is acquired by the oscilloscope with a predefined time interval. The time interval could be from a margin before the trigger at 0.35 μs to the maximum distance a wave can propagate with a margin which is 0.5 μs. This minimizes the data needed to be processed and provides. (To also investigate the signal and the influence of increasing the signal length when applying the EC equation (see equation 7) a larger interval is also investigated which is from 0 μs until 1.65 μs.)

The energy of the signal E_x is computed as

$$E_x = \sum_{k=1}^{N} x_k^2 = \sum_{k=1}^{N} s_k^2 + \sum_{k=1}^{N} n_k^2 = E_s + E_n \tag{3}$$

where k is the index of the number of samples, N is the total number of samples, x_k is the voltage signal acquired, s_k is the voltage signal of the PD, n_k is the voltage signal of the noise, E_s is the energy of the PD signal and E_n is the energy of the noise signal [21]. The discrete values of the voltage signal vector are element-wise squared and then summed.

The power of the signal P_x is computed as

$$P_x = \frac{E_x}{N} = \frac{E_s}{N} + \frac{E_n}{N} = P_s + P_n \tag{4}$$

where P_s is the PD signal power and P_n the noise power [21]. This is implemented by dividing the energy of the signal E_x by the number of samples.

The EC concept revolves around the concept that the arrival of a pulse causes a change in energy relative to the base energy level. An initial downward trend in the EC (See Equation 5) is apparent due to the criteria combining partial energy of the signal up until that point and the product of the index and the total power of the signal [22].

$$EC_k = E_{x,k} - k \cdot P_x \tag{5}$$

$$E_{x,k} = \sum_{i=1}^{k} x_i^2 \tag{6}$$

The noise dependency has no significant influence on the localization accuracy and is assumed to be time-invariant [21].

$$EC_k = E_{s,k} + E_{s,k} - k \cdot P_s - k \cdot P_n = E_{s,k} - k \cdot P_s \tag{7}$$

The minimum of the EC (See Equation 5), is found through the `min()` function. Mathematically it is expressed as

$$\frac{\partial EC_k}{\partial k} = 0 = x_k^2 - P_s \tag{8}$$

The mathematics, see Equation 8, can explain the idea behind the EC method. Conceptually, a change in the EC is observed as there is a sudden increase in the energy as the PD pulse arrives. This results in an increase in the energy and thus a change in the direction of the gradient. This change results in a global minimum which is indicative of the time of arrival of the pulse as this is when the energy is detected. The `min()` function returns the time index of the data point.

Apply the TOA method as outlined in Section 6.1 using the returned time indices from the minima to calculate the distance of the defect from the antennas. The distances resulting from the top and bottom loop for a specific antenna can also be averaged for further interpretation.

6.3.1 Results

An example PD pulse is shown in Figure 57. The cropped signal is shown in Figure 59 and the squared signal to help distinguish the PD peak from the noise peak is in Figure 49.

The histogram analysis for the top antenna pair (two closest to defect as outlined in the TOA method see Section 6.1), as well as, the bottom pair is shown in Figure 60 and Figure 61 respectively[5]. To combine the use of the two available loops, an average is also calculated and plotted in Figure 62. The results of the average distance from the defect for the 100 pulses is summarized in Table 4.

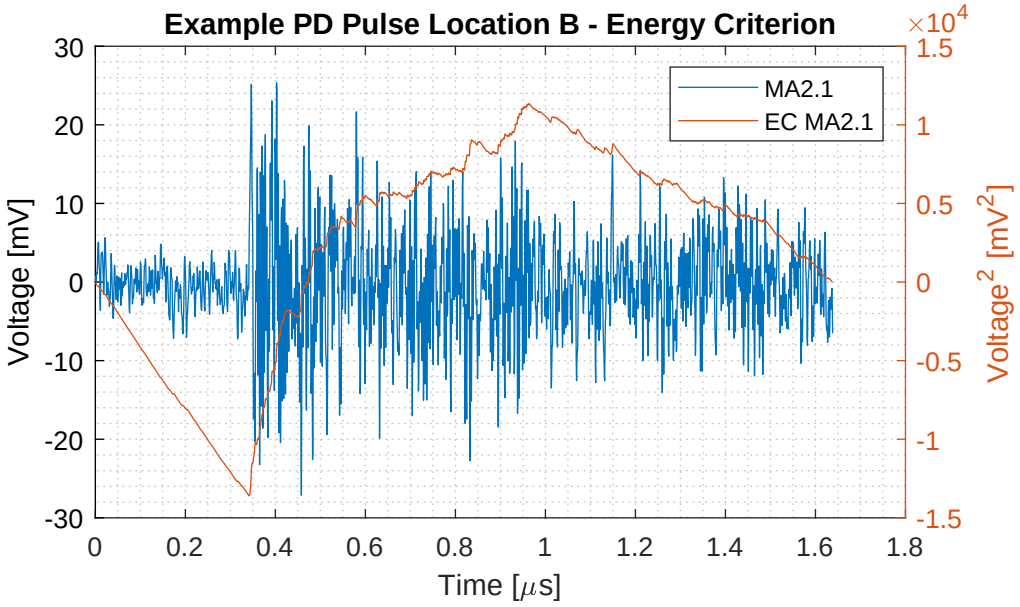

Figure 57: Example MA2.1 Response to 1 of the 100 PD pulses acquired with the EC Applied - Location B

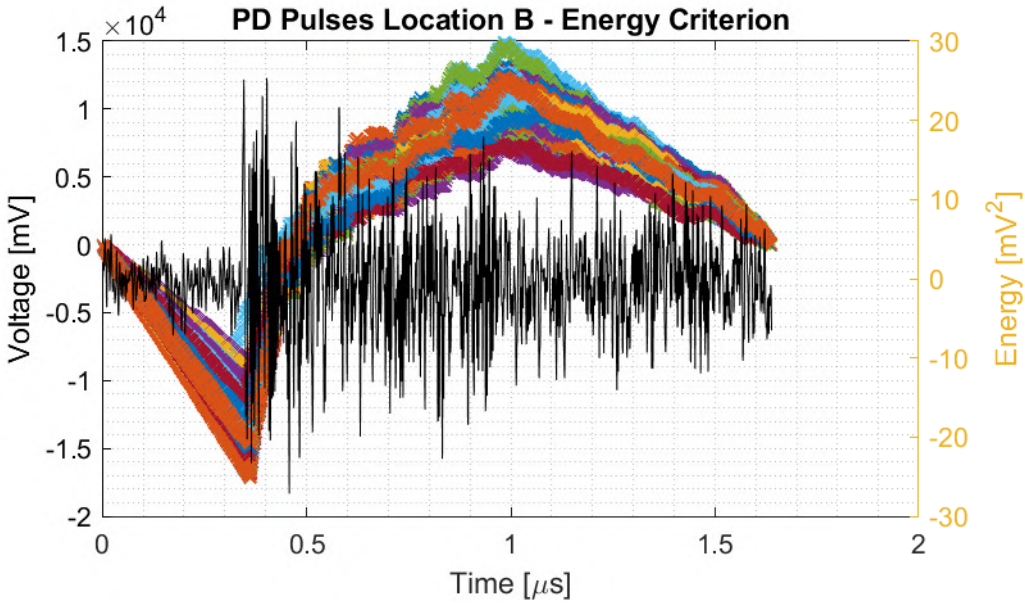

Figure 58: Example MA2.1 Response to 100 PD pulses acquired with the EC Applied - Location B

5 The full-scale Histogram plots are shown in the Appendix A.6 due to the variance in a few outlier data points caused by abnormal noise levels causing the scaling the plot not to fit in the main section.

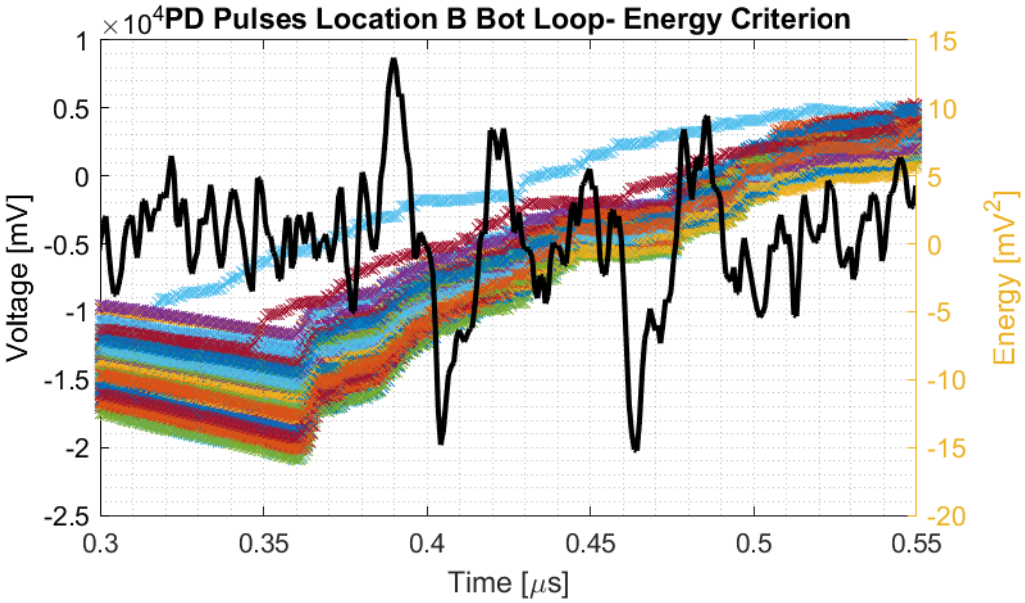

Figure 59: MA2.1 Example Cropped Pulse with EC lines of 100 PD pulses - Location B

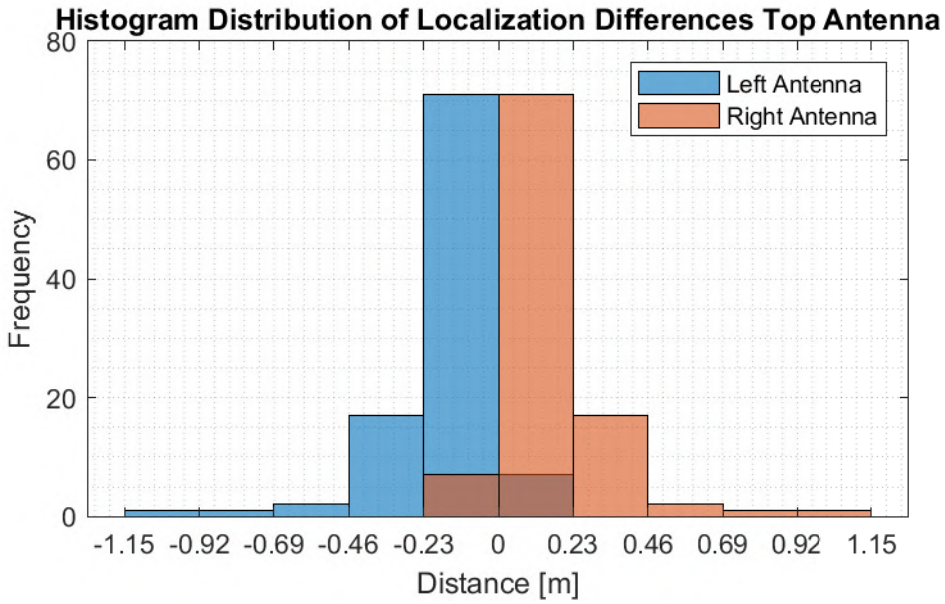

Figure 60: Histogram of Distance Distribution of Top Antenna for the EC Method - Location B

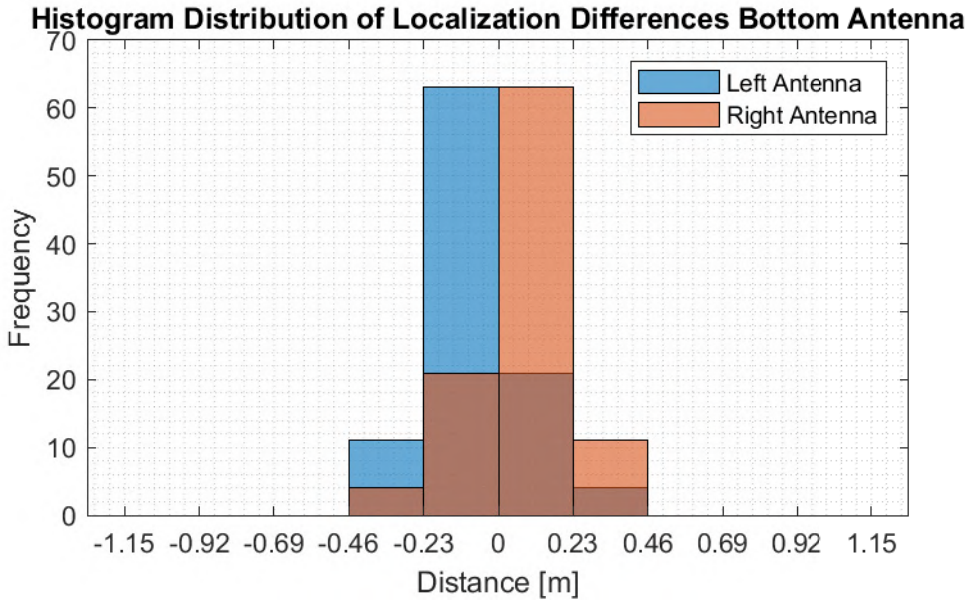

Figure 61: Histogram of Distance Distribution of Bottom Antenna for the EC Method - Location B

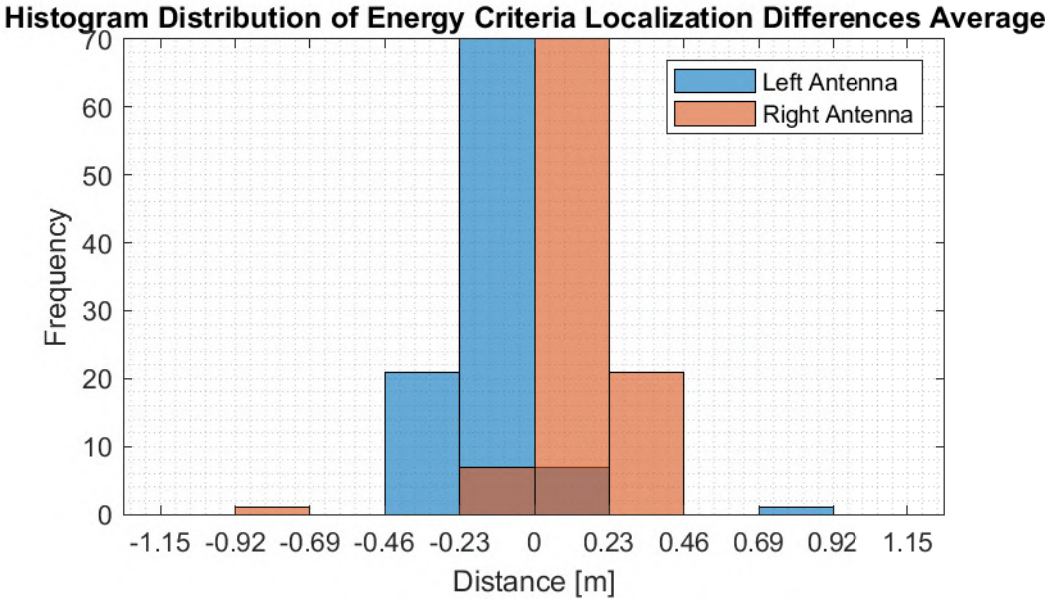

Figure 62: Histogram of Average Distance Distribution of the Top & Bottom Antenna for the EC Method - Location B

Table 4: Full acquired signal Summary of average distance from the defect for the 100 pulses of the top loops, bottom loops and the average of the top and bottom loop applying the EC algorithm. - Location B

	Distance (m)
Top Antennas	-0.14
Bottom Antennas	-0.09
Average of Antennas	-0.11

Table 5: Cropped Signal Summary of average distance from the defect for the 100 pulses of the top loops, bottom loops and the average of the top and bottom loop applying the EC algorithm. - Location B

	Distance (m)
Top Antennas	-0.19
Bottom Antennas	0.29
Average of Antennas	0.05

Location D

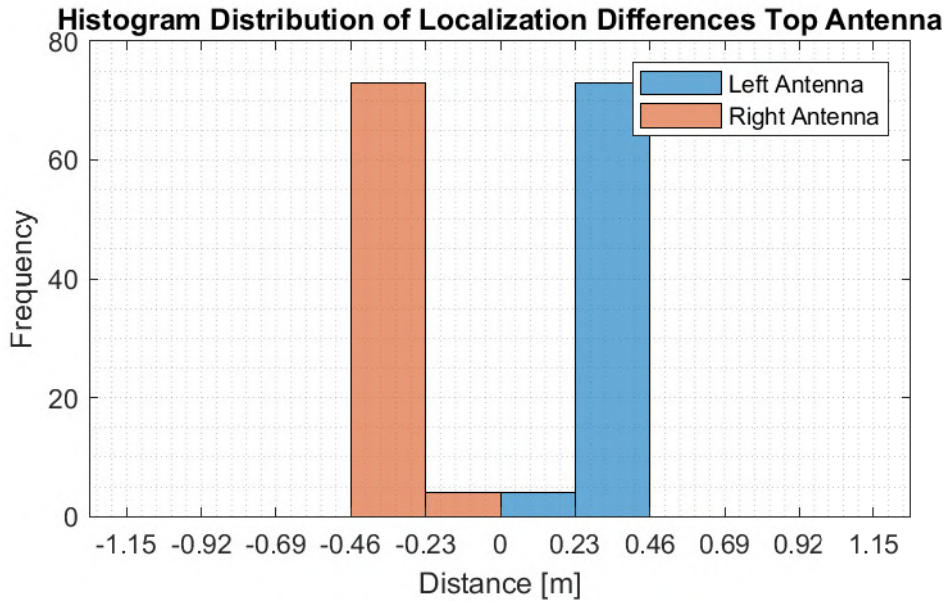

Figure 63: Histogram of Distance Distribution of Top Antenna for the EC Method - Location D

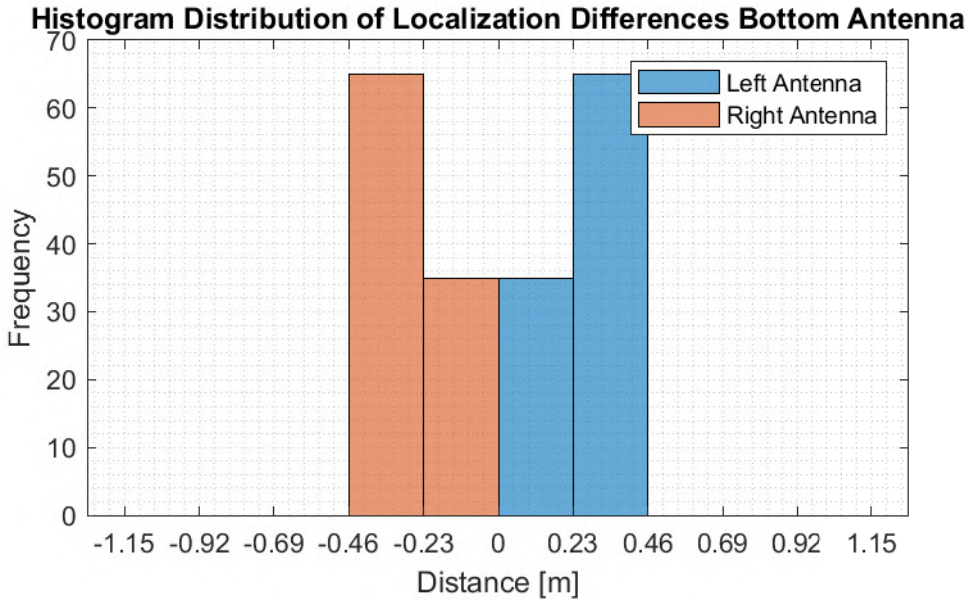

Figure 64: Histogram of Distance Distribution of Bottom Antenna for the EC Method - Location D

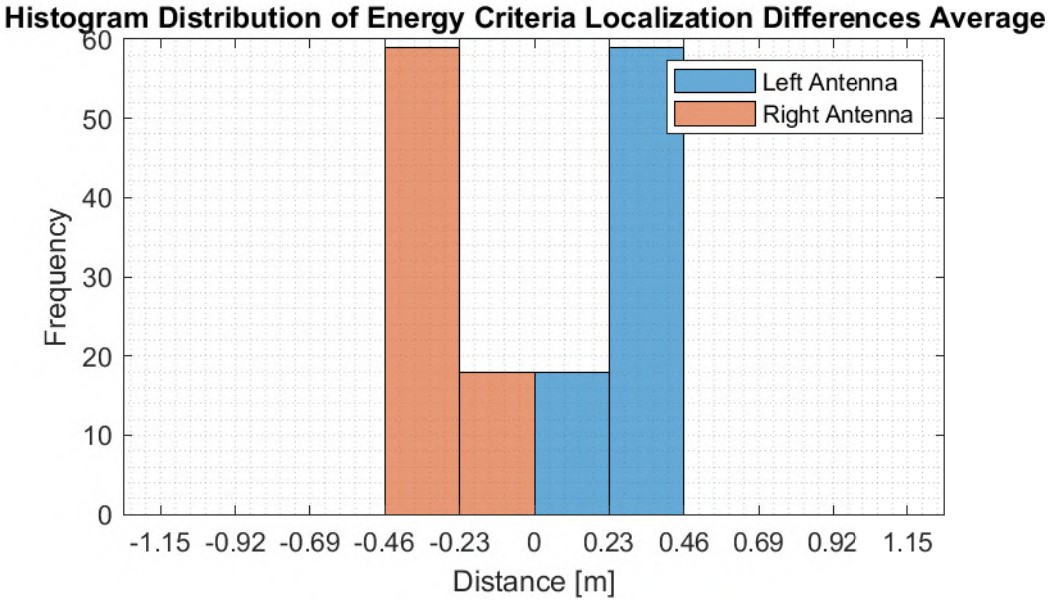

Figure 65: Histogram of Average Distance Distribution of the Top & Bottom Antenna for the EC Method - Location D

Table 6: Summary of average distance from the defect for the 100 pulses of the top loops, bottom loops and the average of the top and bottom loop with the cropped acquired signal applying the EC algorithm. - Location D

	Distance (m)
Top Antennas	1.22
Bottom Antennas	0.42
Average of Antennas	0.82

Runtime
The MATLAB Profiler is used to determine the execution time of the program. For all of the algorithms, the same number of data points are used (cropped signal) and the same time-consuming `saveas` *statement is used to store the histogram of the average distance distribution. Time optimizations could have been made by for example preallocating vectors before for loops but the idea is to get an order of magnitude estimation as a comparison between the methods.*

The runtime for the EC method is 14.2 seconds. This is a reasonable computation time and the order of magnitude less than a minute is not of a concern.

6.3.2 Method Evaluation

Pros

- No pretraining is required as compared to the TPD method.
- Less sensitive to rise time and dispersion of the traveling pulse from compartments in the setup than the TPD peak detection.
- Location B: 90 % of measurements within 1.5 m requirement.
- Location B: Average difference between defect and localization is 0.05 m
- Location D: 85 % of measurements within 1.5 m requirement.
- Location D: Average difference between defect and localization is 0.82 m
- Appropriate run time of 14.2 s.

Cons

- High sampling synchronization required.
- Resolution is limited by sampling frequency.
- Low noise environment is desired, less than TPD though.
- Minima can be subjected to inaccuracies caused by noise and outliers.
- Some reflections are considered in the time interval after the arrival of the PD which affects the value of P_s and E_s which effect the minima location.
- Requires the TOA method which requires two antennas and the defect should be between the antennas.

6.4 Phase Method

The implementation of the Phase Method (PM) algorithm in MATLAB is elucidated in Figure 66 with a subsequent elaboration of each step.

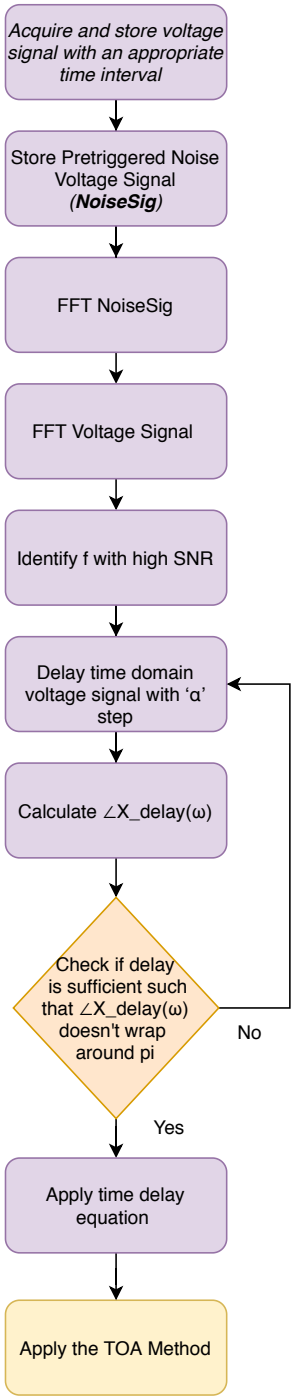

Figure 66: Flowchart Phase Method Algorithm

The method retrieves the phase for a frequency with the highest SNR. It is checked if the phase wraps around $\pm\pi$ and if it does, a delay is applied in the time domain for the voltage signal. The procedure is repeated until for the chosen frequency, the phase does not wrap around $\pm\pi$. The time delay is then converted into the time of arrival (applying Equation 9.)

The voltage signal is acquired by the oscilloscope with a predefined time interval. The time interval would be from 0 μs (the PM delays the signal until the peak is detected, hence the pretrigger is used) to the maximum distance a wave can propagate in the setup with a margin which is 0.5 μs.

The first 0.35 μs (the pretrigger) is cropped and is a representative sample of the noise.

The `FFT()` is applied to the entire voltage signal.

The `FFT()` is applied to the cropped pretrigger representative noise signal.

The ratio of the $\frac{FFT(VoltageSignal)}{FFT(Noise)}$ is observed as an approximation for the Signal to Noise Ratio (SNR) (as extracting the noise from the signal was not feasible). The frequency which yields the highest ratio is where the PM will most likely be reliable. This is observed roughly at $f = 50$ MHz as read from Figure 67.

The time domain signal is delayed with a step α.

The phase of the delayed signal is calculated using `angle()` and is plotted as shown in Figure 69.

A check is placed to verify if the delayed signal wraps around π at the chosen frequency. To verify this, its value is also compared to the original signal as shown in Figure 70. If the delay is insufficient (it wraps around pi), another α step is incremented and it is checked again. This is repeated until the signal does not wrap around π.

When the delay is sufficient, the value of the delay is stored as τ_{ch}. Equation 9 is applied

$$t_{oa} = \tau_{ch} - \tau \tag{9}$$

where t_{oa} is the time of arrival, and τ is defined as the arrival time as expressed in Equation 10 where

$$\tau = -\frac{\angle X(\omega_c)}{\omega_c} \tag{10}$$

the $\angle X(\omega_c)$ is the phase angle of the original signal at the specific angular frequency, and ω_c is the angular frequency.

The time of arrival is defined as the difference between the delay time and the arrival time [21]. Apply the output of Equation 9 in the TOA method as outlined in Section 6.1 to calculate the distance of the defect from the antennas. The distances resulting from the top and bottom loop for a specific antenna can also be averaged for further interpretation.

6.4.1 Results

The FFT of the voltage signal and noise of an example pulse is shown in Figure 67. The original signal and its delayed version is shown together with the signal phase frequency behaviour in subplots in Figure 69. For clarity purposes, this is also split into four subfigures as shown in figure 68.

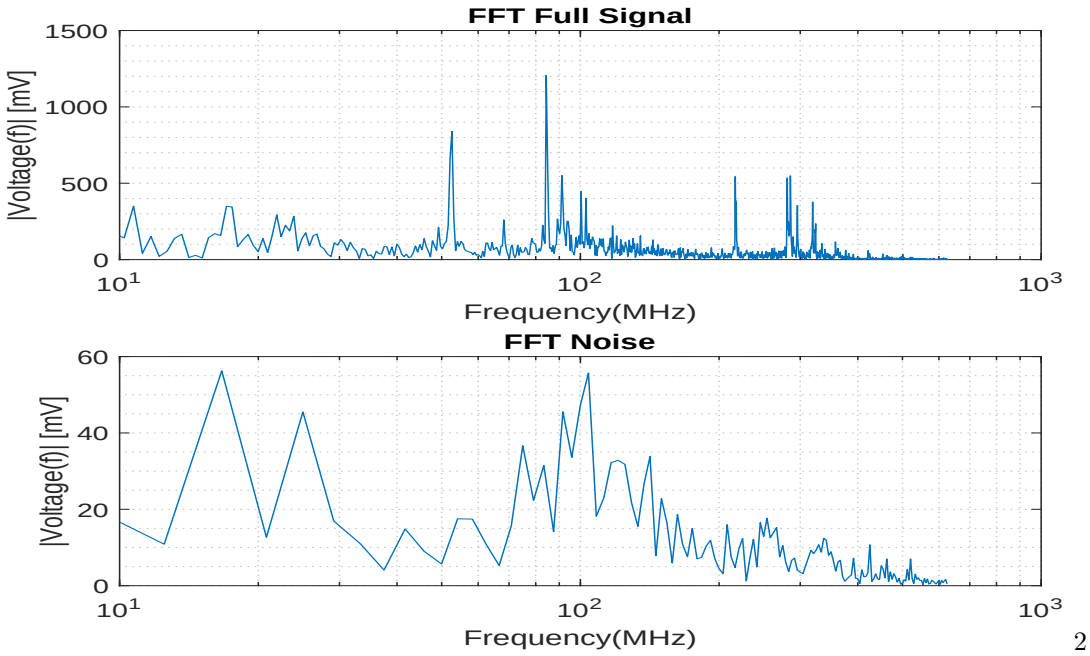

Figure 67: FFT of Voltage Signal + Noise (top subplot) and FFT of Noise Signal (bottom subplot)

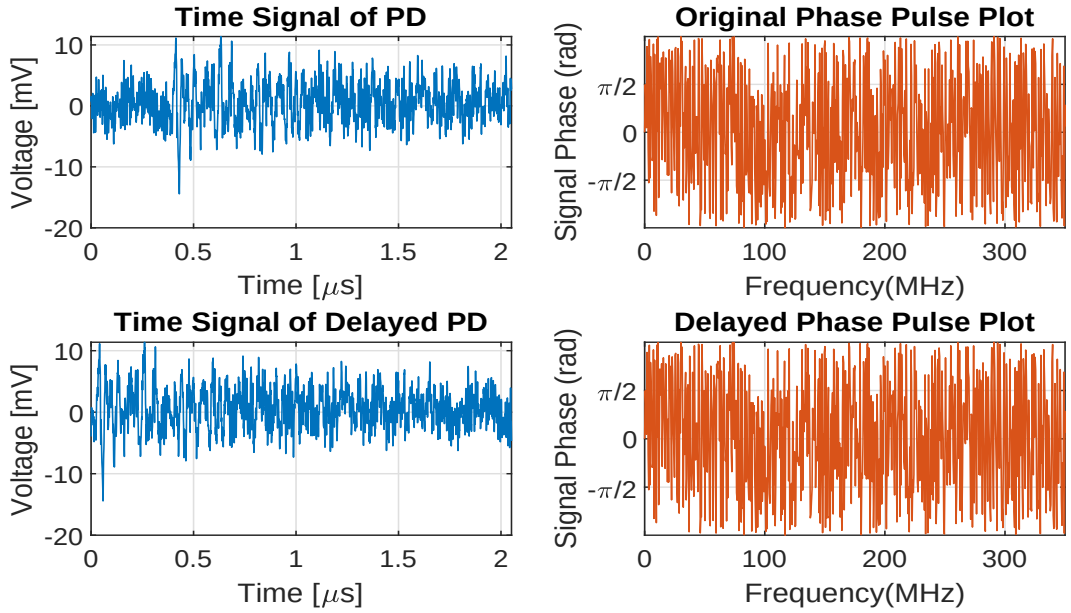

Figure 68: Original voltage time signal of PD pulse for MA 2.1 - Location B and the delayed version with their corresponding

Specific frequency bands according to interesting high SNR estimates are investigated to investigate the if the signals wraps around $\pm\pi$. These are presented in Figures 69 and 70.

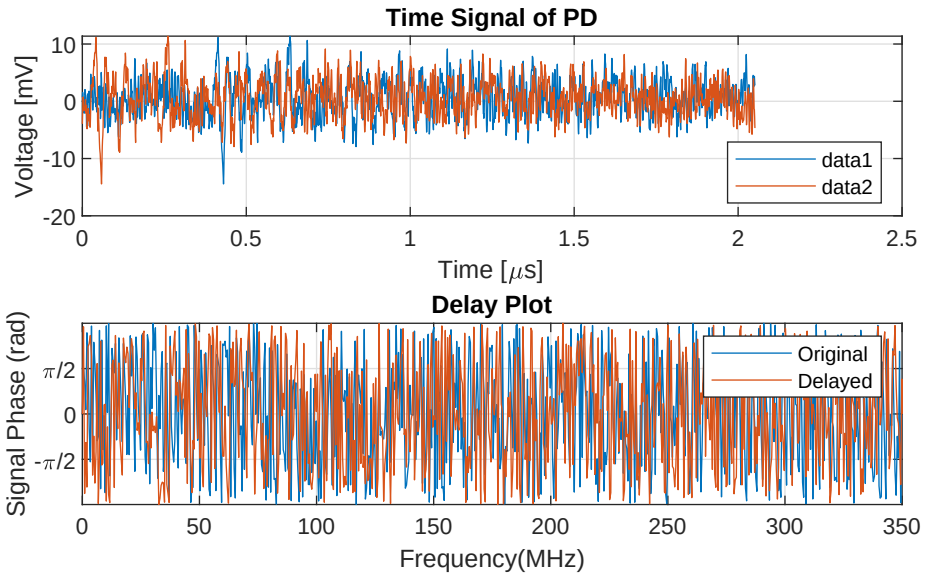

Figure 69: Inspecting Frequency ranges after maximum delay, Phase Method MA2.1 - Location B

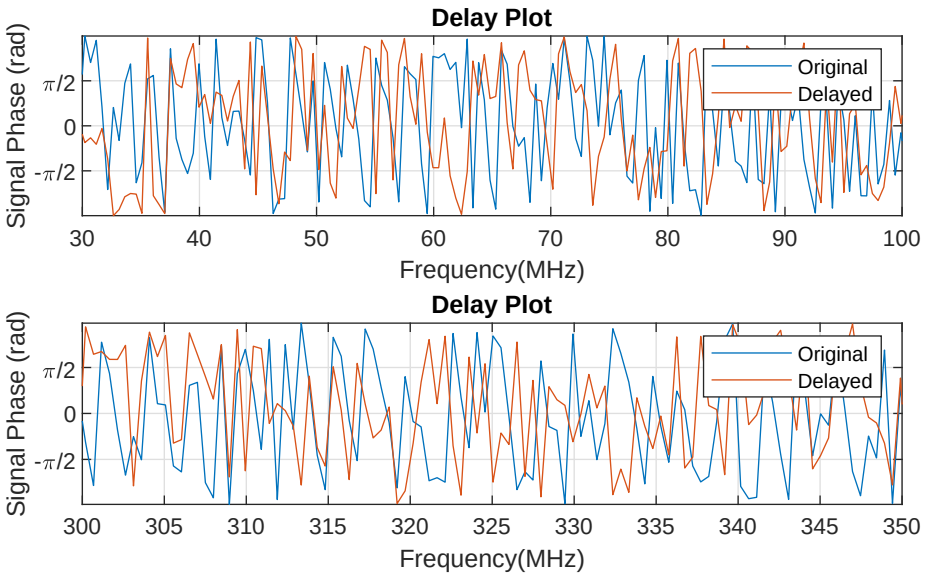

Figure 70: Inspecting Frequency ranges after maximum delay, Phase Method MA2.1 - Location B

It is observed from Figure 70 that delaying the signal does not prevent the signal from wrapping around $\pm\pi$. The method is thus tested to verify its functionality with a theoretical PD Pulse. This pulse is mathematically generated and then delayed. The pulse and its delayed version is shown in Figure 71.

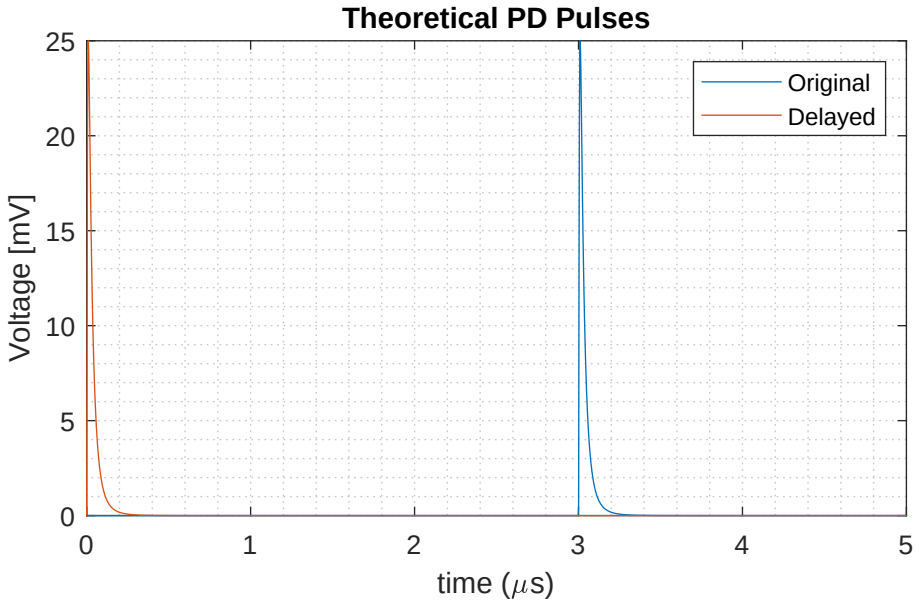

Figure 71: Inspecting Frequency ranges after maximum delay, Phase Method MA2.1 - Location B

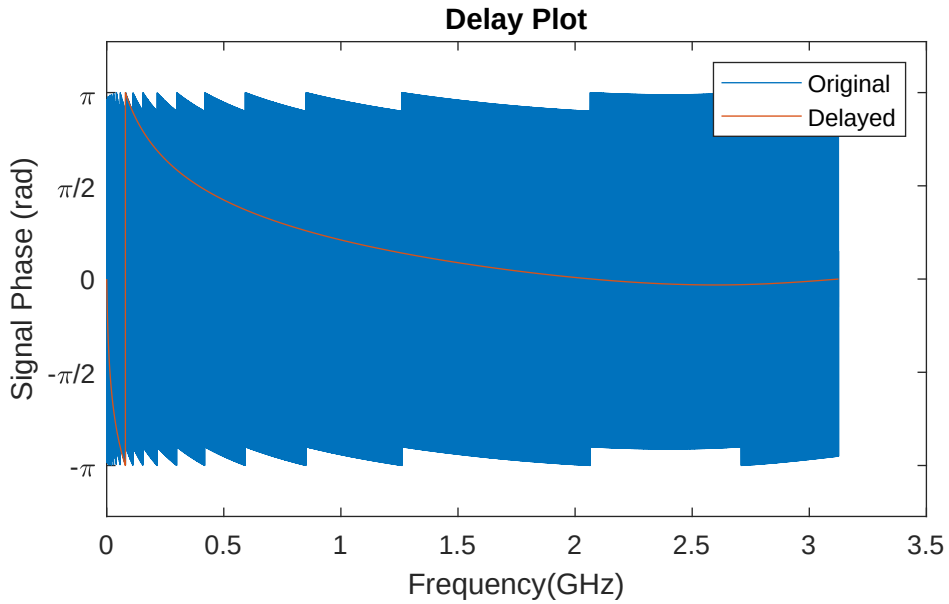

Figure 72: Inspecting Frequency ranges after maximum delay, Phase Method MA2.1 - Location B

As shown in Figure 72, the implementation of the PM algorithm is working as the phase of the delayed signal does not wrap around π. This verifies the theoretical functionality of the algorithm and its implementation.

6.4.2 Method Evaluation

The PM is unsuitable for detecting the time of arrival of the PD pulse with the used measurement system. It is observed that the PM theoretically functions for a clean PD pulse. This theoretical pulse has no noise and reflections. The behaviour of the detected pulse and noise influence varies for each pulse. The frequency

components of the PD pulse measured and noise vary and influence the phase content of the signal. The phase retrieved at the frequencies with the highest SNR estimate still wraps around $\pm\pi$. It is mentioned in the paper [22] that the method is sensitive to noise and reflections but is advantageous as it is not influenced by dispersions and attenuation. The noise levels and reflections in the GIS setup are too significant for the method to be used. Noise rejection methods or using an amplifier with a lower bandwidth (at the cost of time resolution) could be investigated and then the method could be tested again. The profiler provides a runtime in the order of 36.3 s. Due to its non-functionality caused by sensitivity to noise and reflections as well as the run time being significantly higher than the alternative TPD and EC methods around 15 s, the PM is deemed unsuitable for localization in the setup and should be rejected.

6.5 Evaluation of Methods

The methods can be compared with the criteria of: percentage of signals within 1.5 m margin, accuracy (how close the value is to the defect) and execution time. The objective of the measurement setup was to verify if the MAs could suitably be used for localization. The conclusion is that they can indeed be used for localization purposes with the TPD and EC method. The TPD method has the greatest percentage of pulses within the 1.5 m margin, at 95 % for both locations B and D. This is the most important criteria and thus the TPD method is deemed most suitable. The drawbacks of the TPD are that it might be more problematic in noisy environments where pre-training and setting an appropriate threshold level would be challenging. The EC appears to be in that sense it more dynamic and considerate of the base noise level. The EC has the most accurate localization for location B and the TPD is most accurate for location D. Why this is the case needs to be researched. Possible ideas and investigations include the influence of the distance on the closest antenna to the source and the spacer close to location D. Other considerations include the investigating sensitivity of reflections and attenuation in the T and L branches which influence the signal to be detected. All of these insights will aid with eventually creating guidelines to determine the spacing of MAs in a setup.

General improvements to the measurement system would be to understand the influence of external noise on the antennas. This is currently being investigated (out of the scope of the thesis) by introducing an electrical radiator and conducting a spectrogram analysis. This way the noise interference can be categorized and filters could be designed for the use case. The influence of noise is significant and could cause the chosen localization method to be different. Perhaps even a combination of the two methods depending on the topology of specific parts of the GIS where one algorithm consistently outperforms the other (since run time is in the same order of magnitude).

A quick aspect to investigate would be to investigate the influence of the resolution of the signal which is currently is limited to 0.23 m due to the 1.25 GS/s sampling frequency. Another practical implementation to deal with outliers would be to make conclusions based on a large number of pulses. If the antenna positioning, spacing and resolution have been experimentally verified with a large sample of data, the estimation of the localization can be improved by accordingly rejecting highly improbable outliers. An example in the EC analysis included a localization value of 7.36 m when the average distance was in the order of 0.5 m. Another idea would be to introduce a criterion which selects the most frequently occurring distances for a given number of discharges (for example investigating the mode of the histogram bin which would be 0.23-0.46 for the EC location D) occurring within the 1.5 m could be used for interpretation. Then the outliers and other data can accordingly be rejected potentially improving accuracy. These ideas can be checked and experimentally verified for their validity and consistency.

6.6 Chapter Conclusions

Localization of a corona PD is possible in the setup with the TPD and EC method. The PM is unsuitable due to its sensitivity to reflections and noise and thus is unable to localize the defect. The TPD method can localize a defect within $\pm$1.5 m 95% of the time for location B and D. The EC method can localize a defect

within ±1.5 m 90% and 85% of the time for location B and D accordingly. The run time magnitude of the TPD and EC method for 100 pulses are in the same order of magnitude of 15 s and thus both good options from computation time. Both the TPD and EC are observed to be sensitive to noise and further research on noise rejection would be fruitful. Overall, the priority is given to the TPD as it has the highest number of pulses within ± 1.5 m as this was desired in order to localize the compartment for servicing.

7 Conclusion

The overarching goal was to develop and characterize a magnetic antenna measurement system in the HF range to measure and localize PDs. As part of the research goals, the goals have been achieved. The conclusions which can be drawn are:

1. A workbench has been built and developed to characterize the magnetic antennas using the Avalanche pulse generator PPLG as input pulses. The resistive termination of 330 Ω, injection and termination cone, resistive wire with a resistance value of 19.10 Ω m is successfully used to cope with reflections in the workbench.

2. The Workbench has been used to measure the antenna response and the data has been processed to determine the frequency characteristics. The peaks around 51 MHz are caused by the LC resonance and HFCT infuence of the grounding. The 105-130 MHz peaks are due to the CM interference.

3. A conference paper, "A NEW PARTIAL DISCHARGE MEASURING SYSTEM IN HVGIS BASED ON MAGNETIC FIELD ANTENNAS", has been accepted with contributions from the thesis to the CIGRE 2020 Paris session.

4. The 380 kV GIS measurement setup has been developed and is suitable for placing the magnetic antennas and defects at several locations. This measurement setup enabled the measurement and acquisition of data of the discharges using the magnetic antennas.

5. The TPD, EC and PM localization methods are investigated and implemented for localization. The PM is unable to localize the pulse due to its sensitivity to noise and reflections. The TPD and EC are both suitable with the TPD being the preferred method due to its high 95% accuracy of localizing the defect within $\pm$ 1.5 m.

Overall, the magnetic antennas have been successfully developed and characterized. They were able to be used in a measurement system for localizing PDs defects in the GIS setup. Chapter specific conclusions have been presented at the end of every chapter for a brief overview of the contents of the chapter.

7.1 Recommendations for Future Research

For the developed workbench, research into deciding how the input pulse can be measured without the HFCT influencing the magnetic antenna frequency response. It was discovered that the 51 MHz resonance was largely caused due to the influence of the HFCT and its grounding connection inside of the GIS. An idea to resolve the issue would be to decouple the measurement of the input and output. Essentially conducting these measurements sequentially and separately. The FFT of an average of 100 input signals and 100 measurements of the output would be reasonable. The ratio can be taken from these separate measurements for the magnitude in the Bode analysis.

Another recommendation would be introducing band-pass filters at the CM frequency bands or any appropriate noise filters would be interesting to investigate and perhaps relevant when applying the MA into the GIS setup. This would assist with the accuracy of determining the discharge magnitude of the PD when when calculating the charge.

As a prerequisite for future research in charge estimation, the needle for the GIS test cell should be sharpened to produce smaller PDs. This would be beneficial for the sensitivity checks in the future.

Another recommendation would be to introduce different MA positions. This would be useful as the TOA method requires the defect to be situated between two antennas. With different MA positions, various locations (of defects) can be investigated. This results in more data also about the influence of the spacing

between the magnetic antennas which can be used to develop rules of thumb for antenna placement.

In terms of other methods for future research into localization, a time frequency analysis could be considered [23] (instead of the TOA method). The essential steps include computing the time and frequency of the PD pulse. Then the double integral of the frequency with respect to time yields the energy distribution of the pulse. Subsequently, the Canny Algorithm is applied for edge detection and then these features are extracted. From these edges, the longitudinal localization can be investigated [23]. The influence of the spacing between the closest antenna and the defect is also of interest. Furthermore, the influence of sensitivity of reflections and attenuation in the T and L branches would be of interest guiding in determining rule of thumbs for MA spacing. The influence of noise is being investigated by introducing a horizontal electric dipole connected to a signal generator [24] and conducting a spectrogram analysis. This way the noise interference can be categorized and data processing techniques such as the cross wavelet transform and the SVM classifier can be used to suppress CM disturbances [24] on the MA.

A Appendix

A.1 Antenna Plots Input/Output + Bode Workbench - Femto 40M-100K

A.1.1 Avalanche Nanosecond Pulse Generator

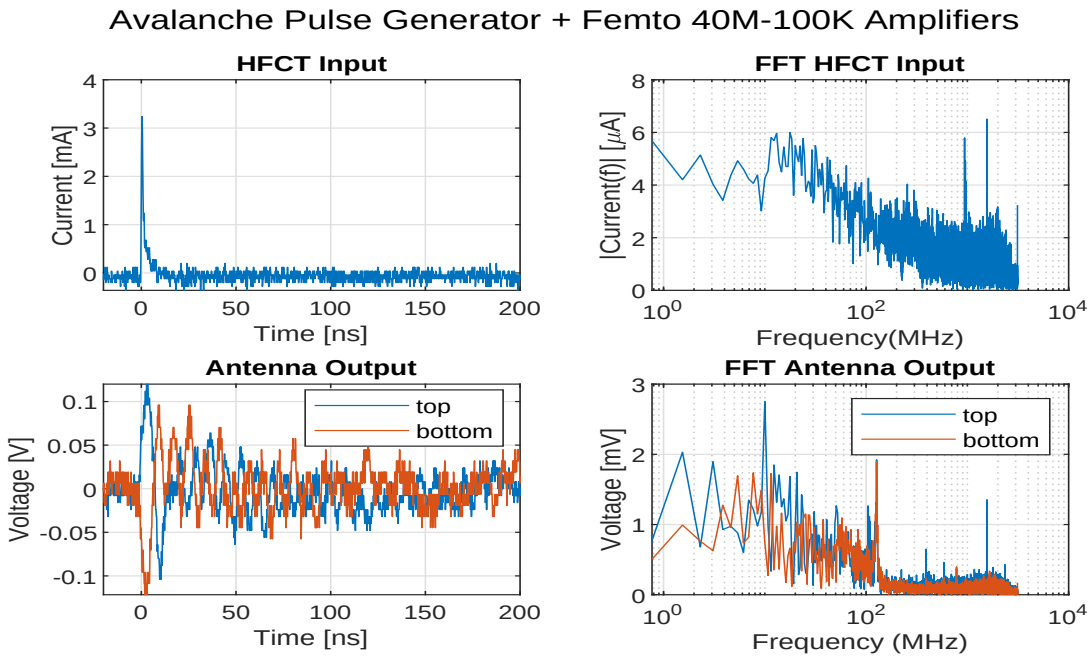

Figure 73: HFCT and Femto 40M-100K Amplifier Top and Bottom Loop Time Domain and Frequency Response of Magnetic Antenna to Avalanche pulse

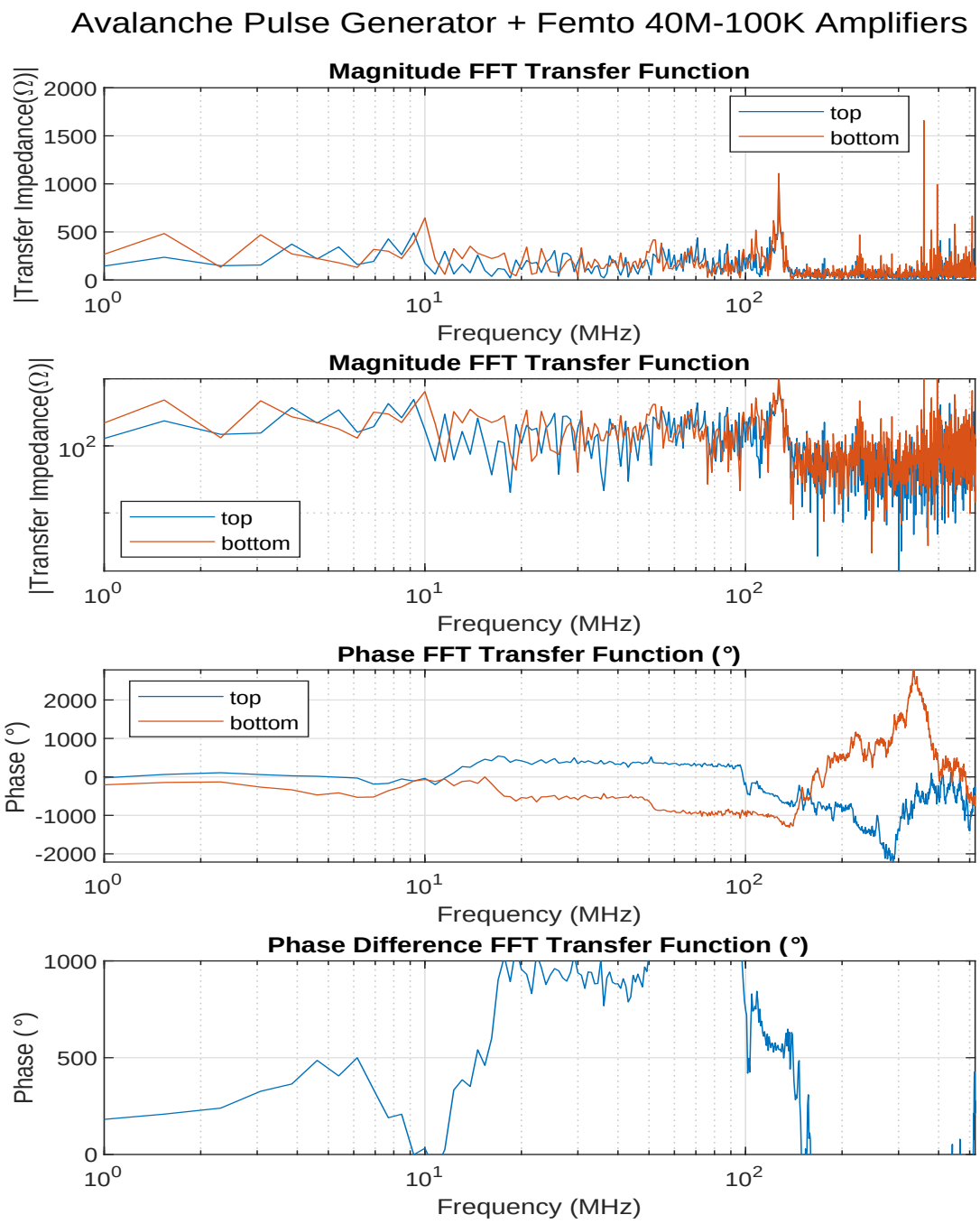

Figure 74: Femto 40M-100K Amplifier Amplifier Bode diagram of Magnetic Antenna loops.

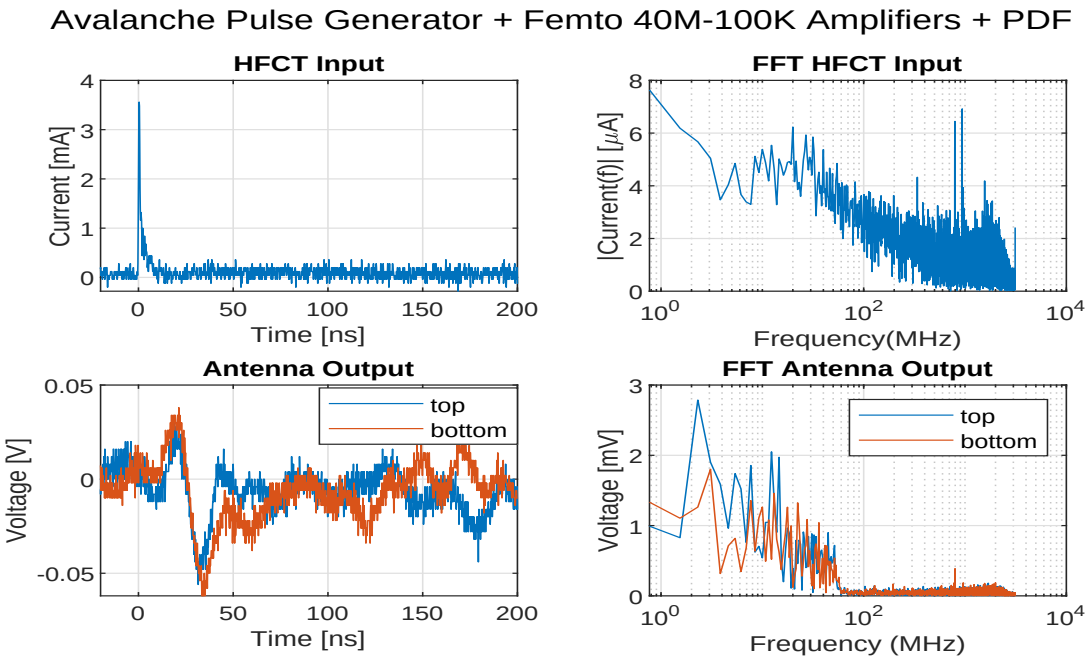

Figure 75: HFCT and Femto 40M-100K Amplifier with PDF Top and Bottom Loop Time Domain and Frequency Response of Magnetic Antenna to Avalanche pulse

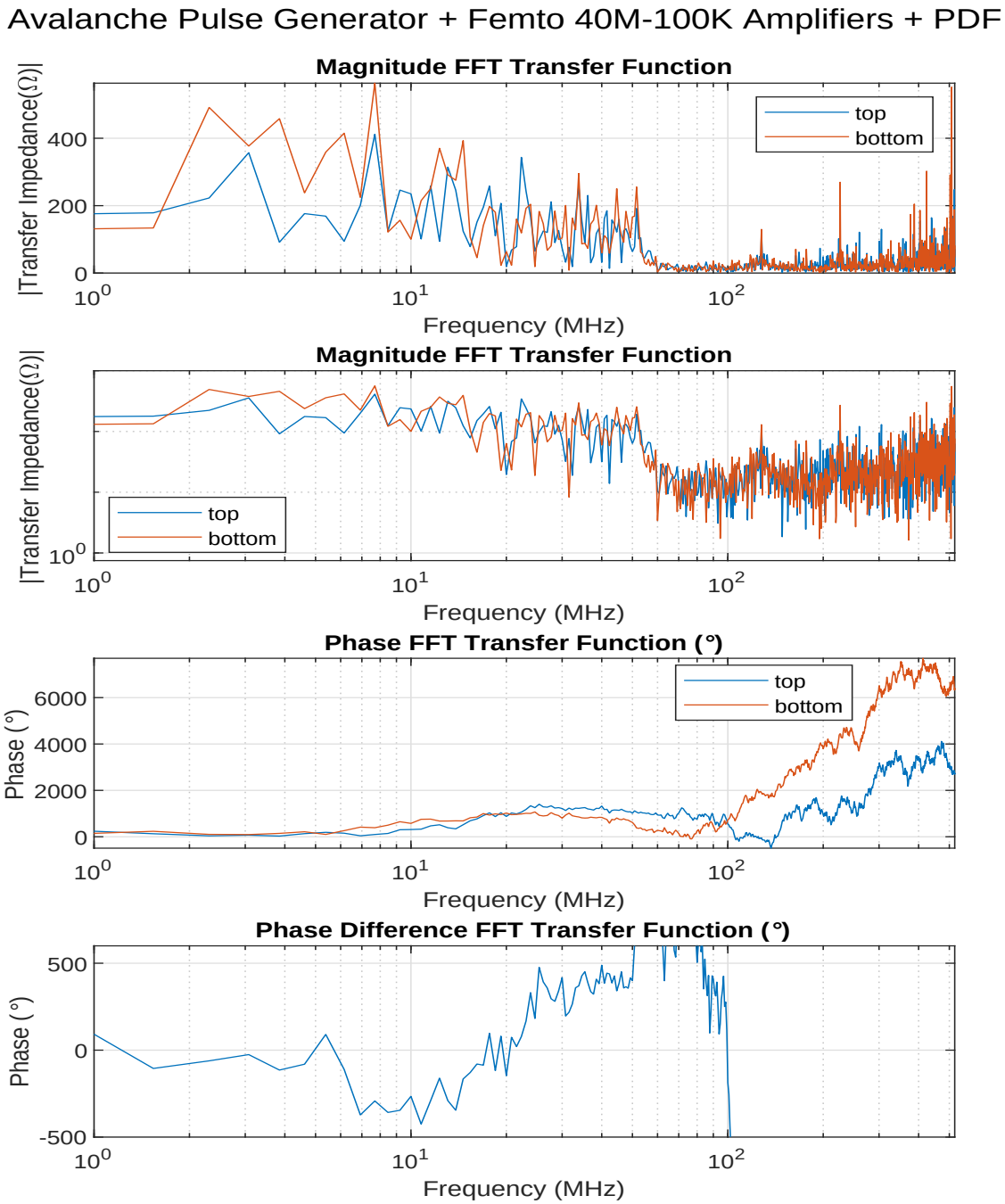

Figure 76: Femto 40M-100K Amplifier with PDF Bode diagram of Magnetic Antenna loops.

A.1.2 Antenna Plots Input/Output + Bode Workbench - Picosecond Pulse Labs Generator

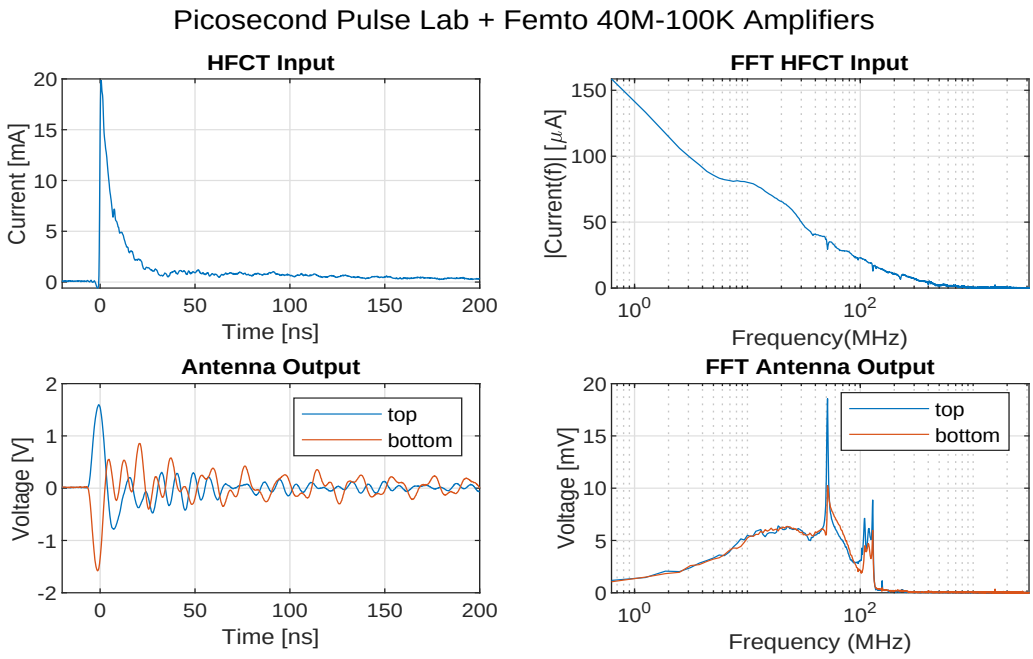

Figure 77: HFCT and Femto 40M-100K Amplifier Top and Bottom Loop Time Domain and Frequency Response of Magnetic Antenna to PPLG Pulse

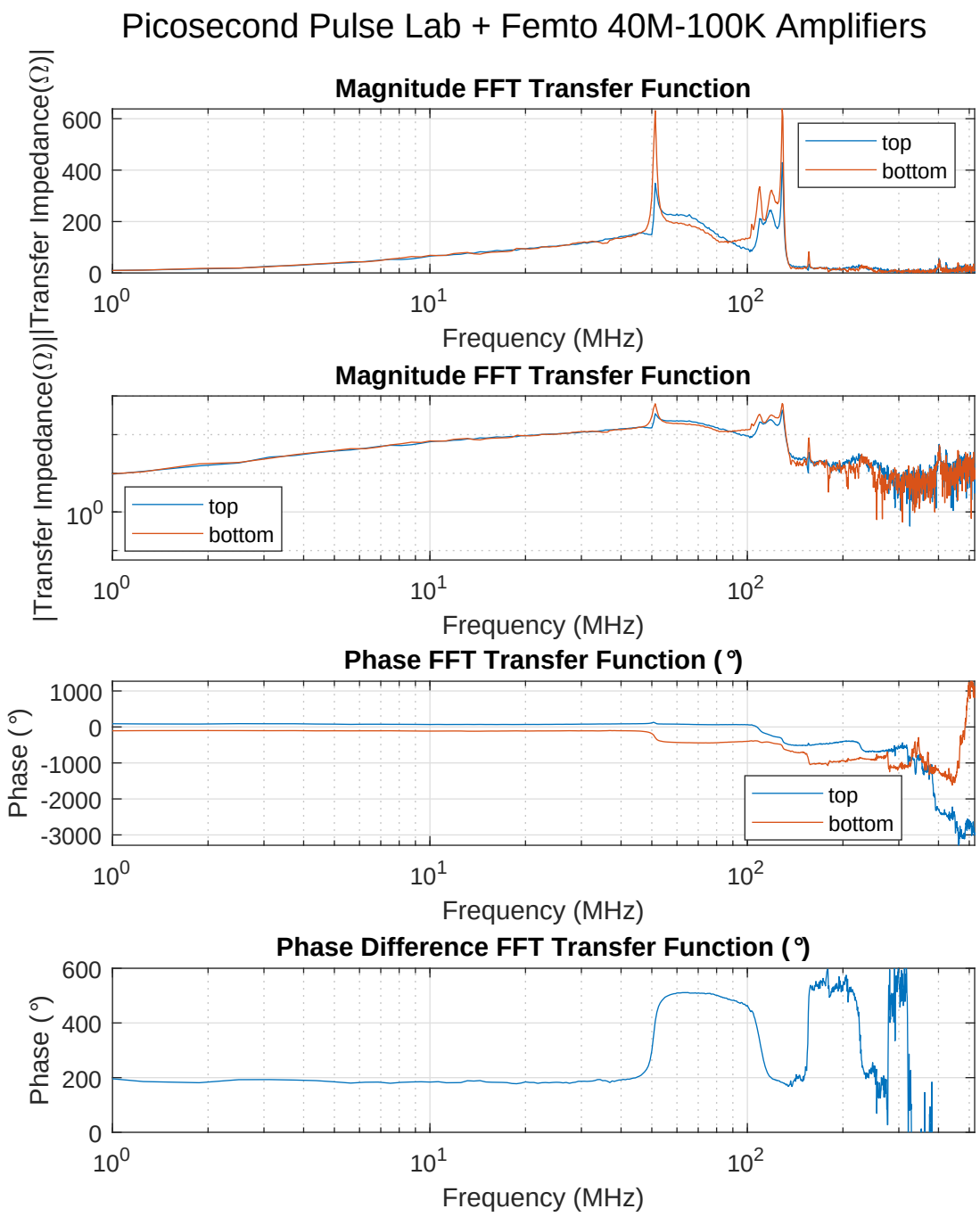

Figure 78: Femto 40M-100K Amplifier Amplifier Bode diagram of Magnetic Antenna loops.

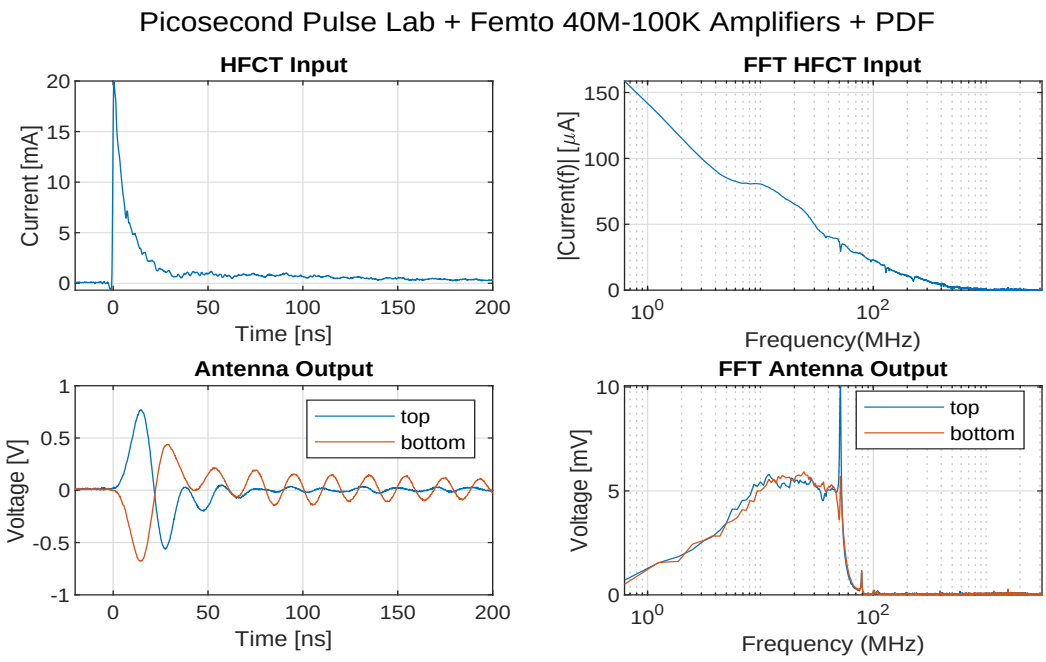

Figure 79: HFCT and Femto 40M-100K Amplifier with PDF Top and Bottom Loop Time Domain and Frequency Response of Magnetic Antenna to PPLG Pulse

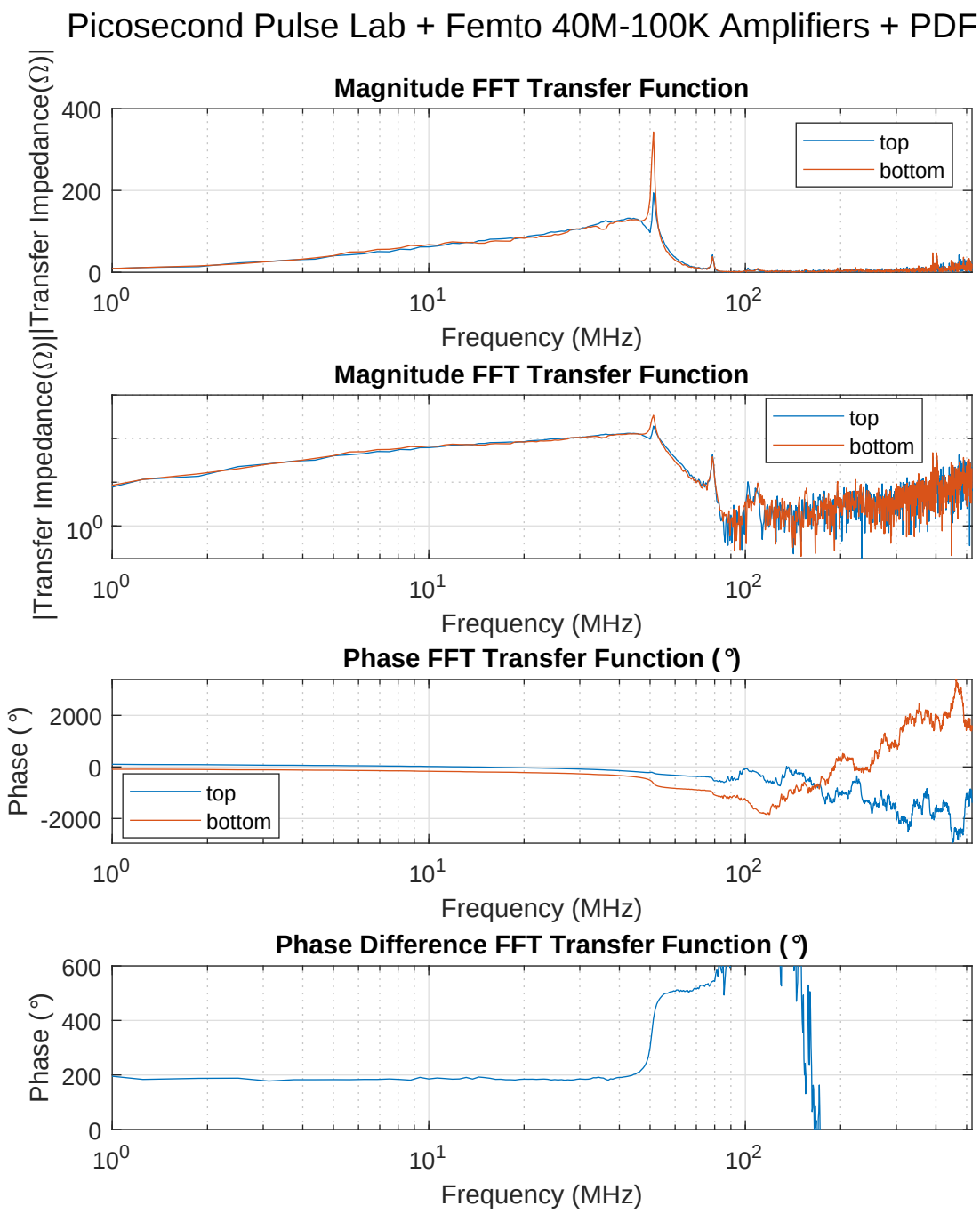

Figure 80: Femto 40M-100K Amplifier with PDF Bode diagram of Magnetic Antenna loops.

A.2 Antenna Plots Input/Output + Bode Workbench - 300-70/69 Mini Circuits Amplifiers

A.2.1 Avalanche Nanosecond Pulse Generator

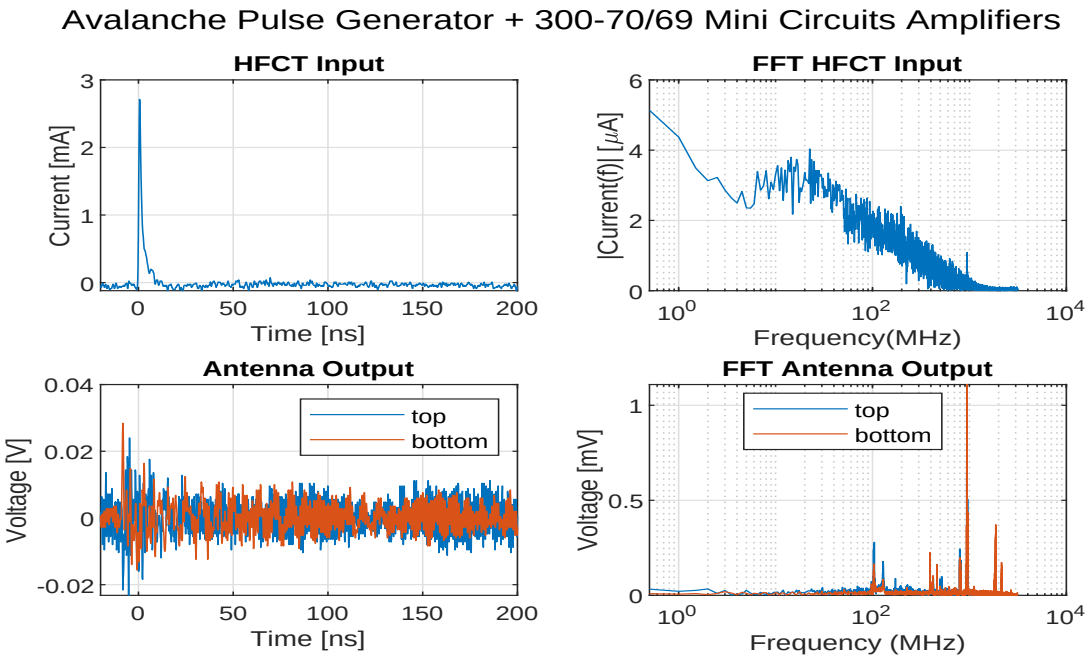

Figure 81: HFCT and Femto 300-70/69 Mini Circuits Amplifiers Top and Bottom Loop Time Domain and Frequency Response of Magnetic Antenna to Avalanche pulse

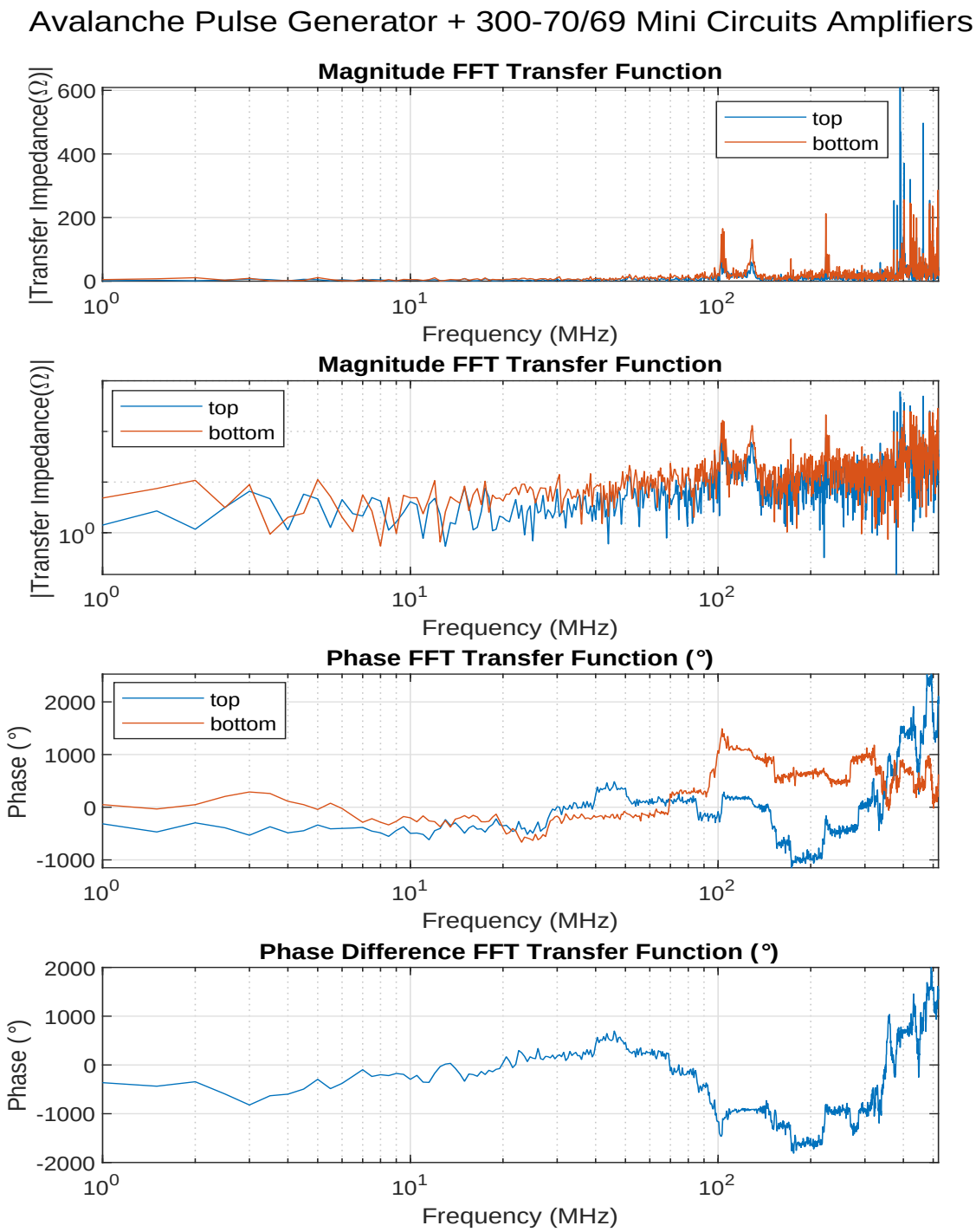

Figure 82: Bode Diagram of Magnetic Antenna Loops using 300-70/69 Mini Circuits Amplifiers

Applying a PD filter:

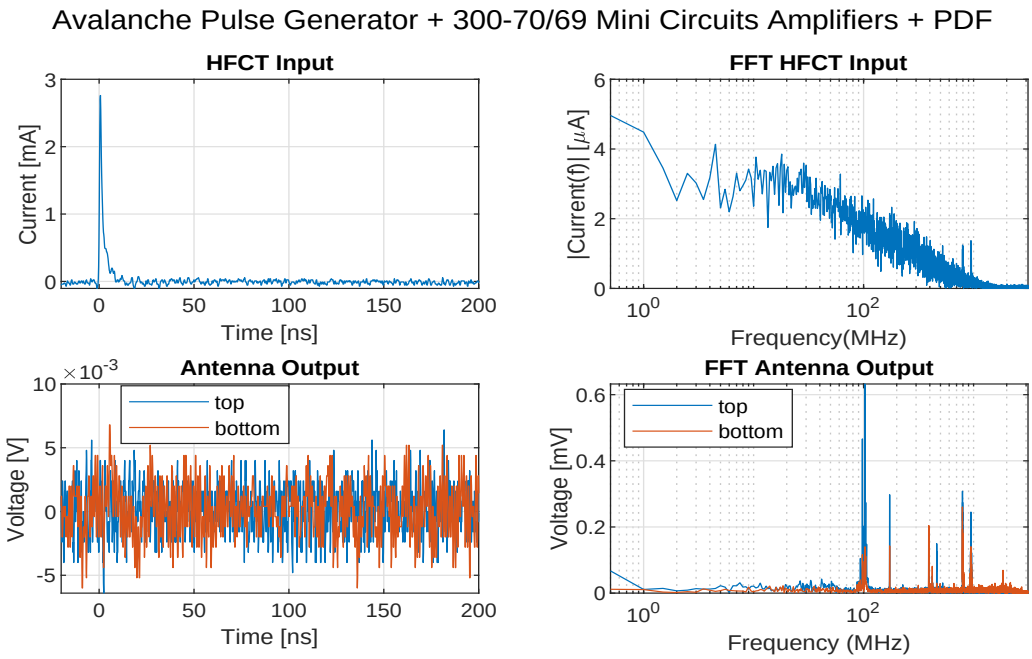

Figure 83: HFCT and Femto 300-70/69 Mini Circuits Amplifiers with PDFs Top and Bottom Loop Time Domain and Frequency Response of Magnetic Antenna to the Avalanche pulse

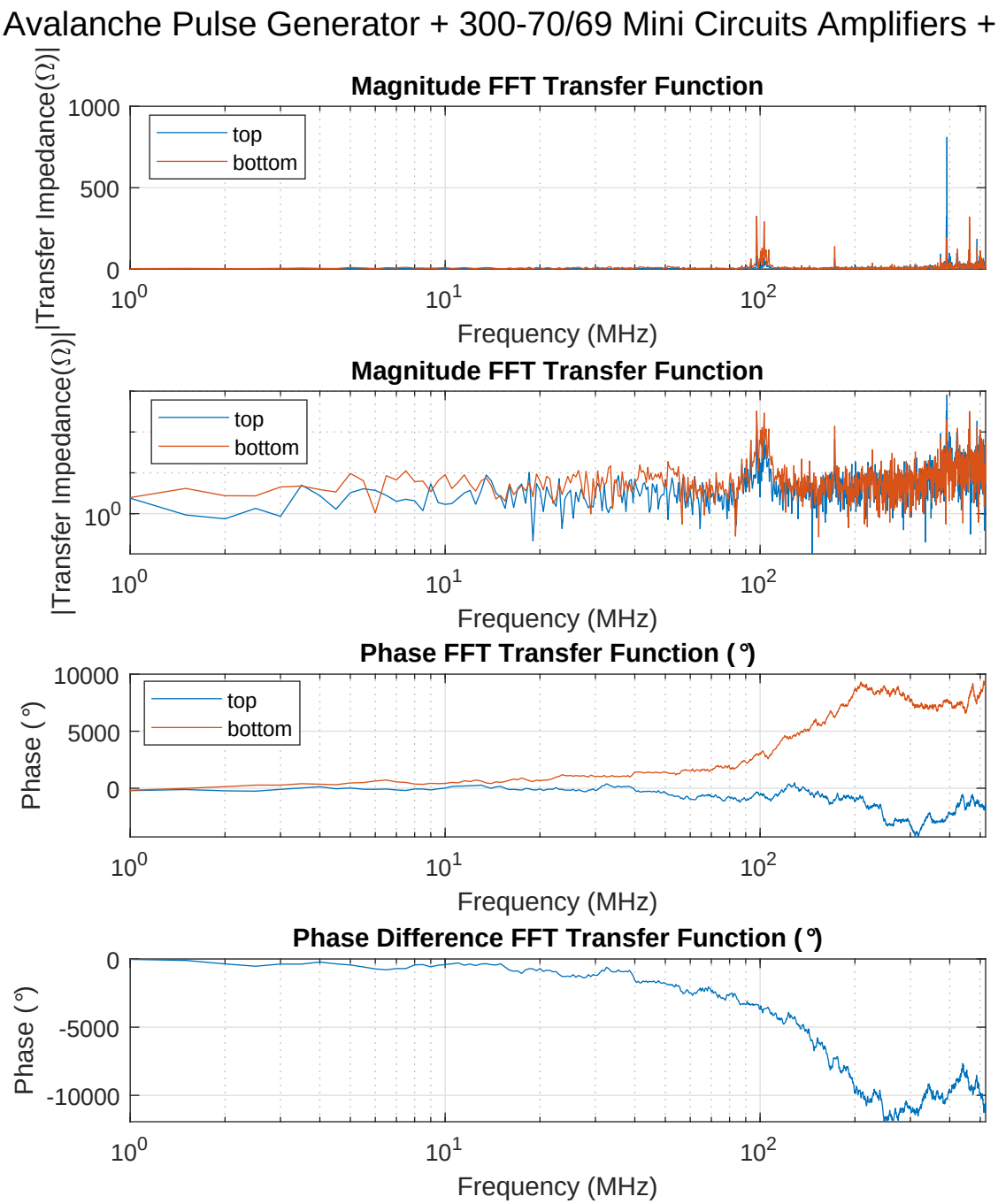

Figure 84: Bode Diagram of Magnetic Antenna Loops using 300-70/69 Mini Circuits Amplifiers with PDFs

Using Cores-42

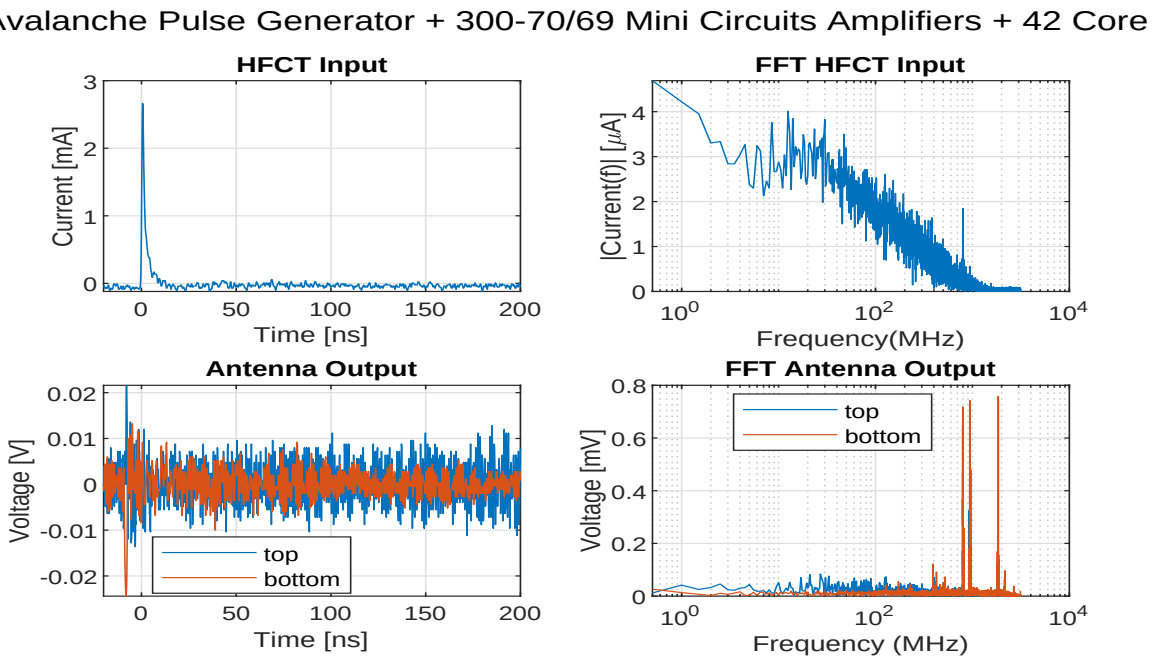

Figure 85: HFCT and Femto 300-70/69 Mini Circuits Amplifiers Top and Bottom Loop Time Domain and Frequency Response of Magnetic Antenna with the 42 Cores to the Avalanche pulse

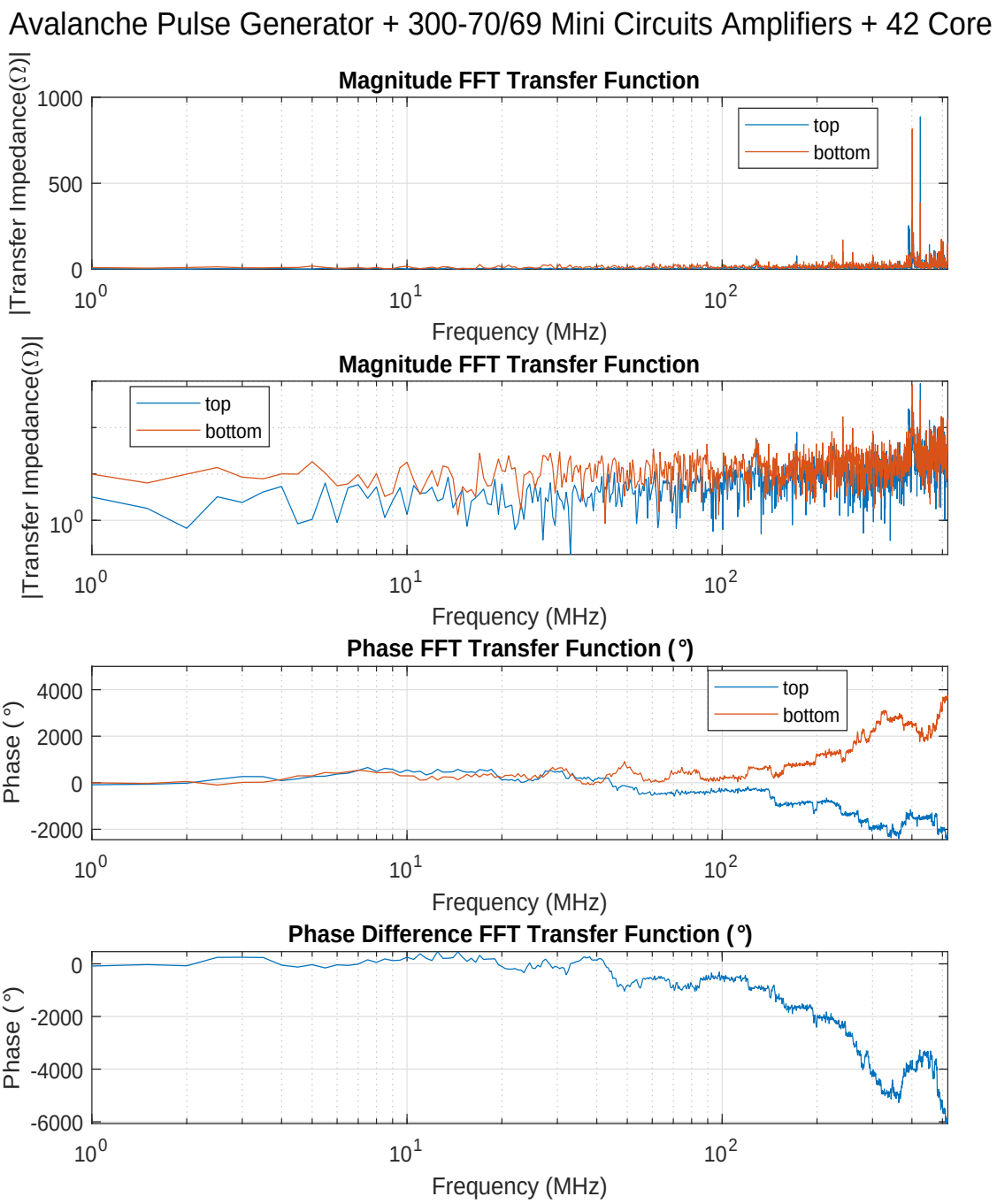

Figure 86: Mini Circuits Amplifier with 42 Core Bode diagram of Magnetic Antenna loops.

Using Cores-72

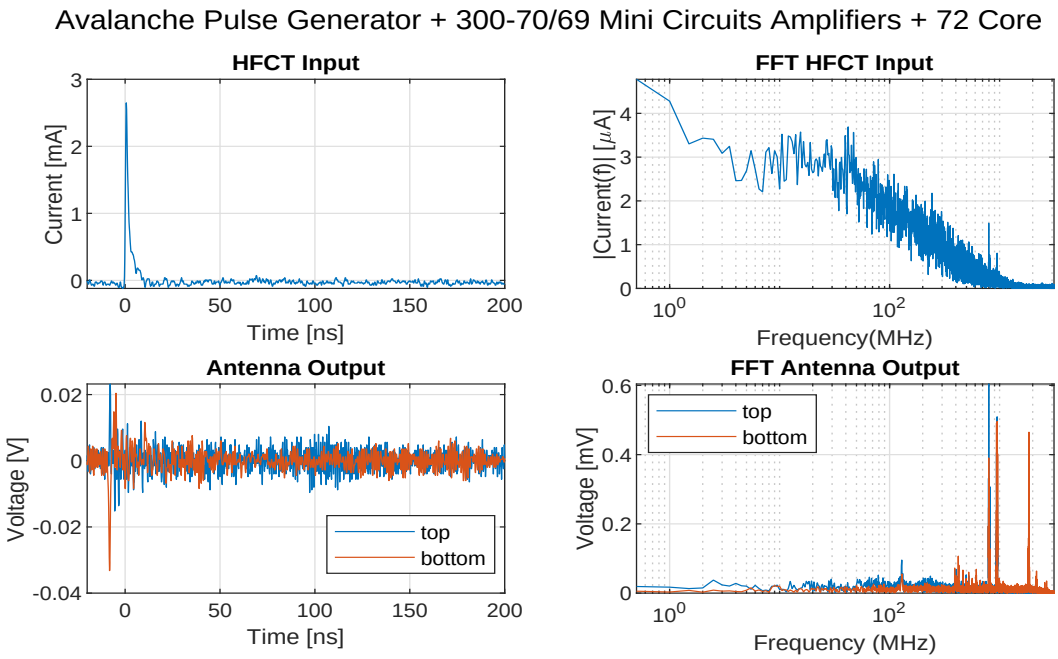

Figure 87: HFCT and Femto 300-70/69 Mini Circuits Amplifiers Top and Bottom Loop Time Domain and Frequency Response of Magnetic Antenna with the 72 Cores to the Avalanche pulse

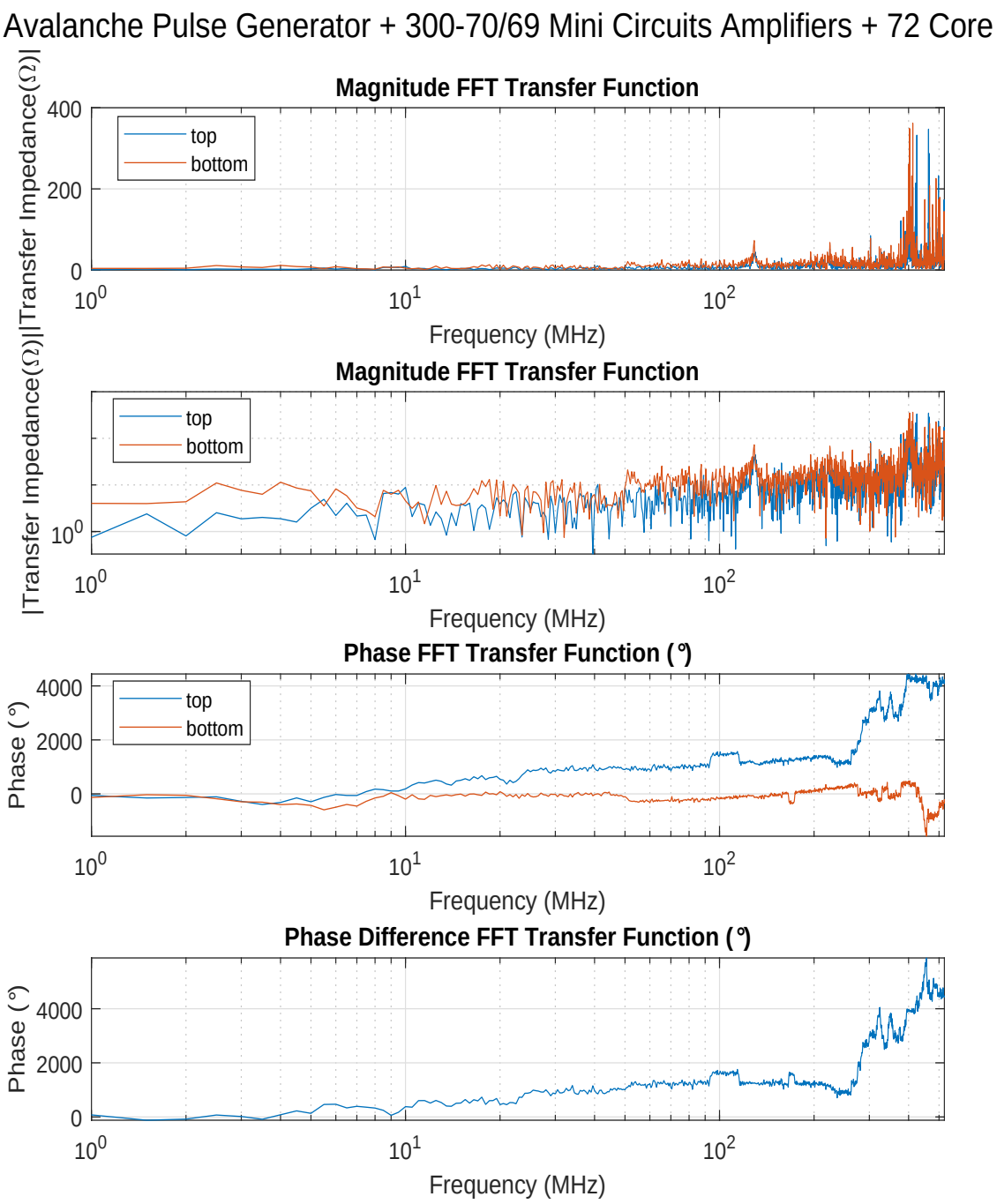

Figure 88: Mini Circuits Amplifier with 72 Core Bode diagram of Magnetic Antenna loops.

A.2.2 Picosecond Pulse Labs Generator

Base Minicircuits

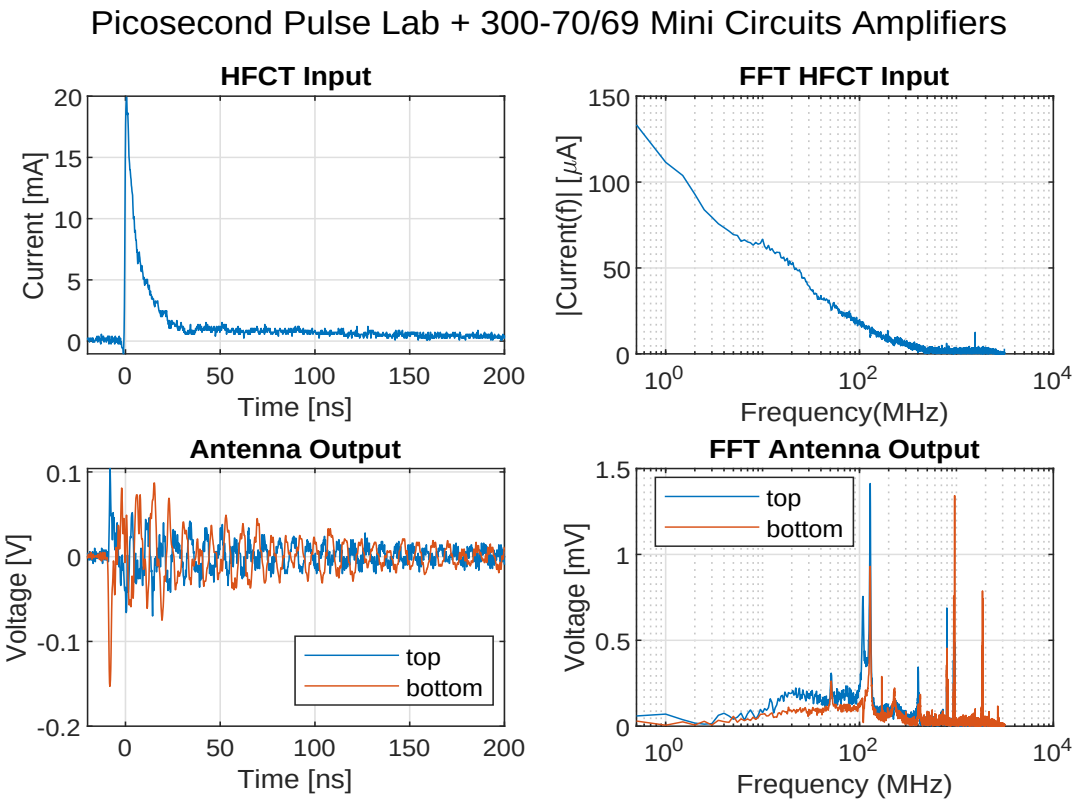

Figure 89: HFCT and Femto 300-70/69 Mini Circuits Amplifiers Top and Bottom Loop Time Domain and Frequency Response of Magnetic Antenna to the PPLG pulse

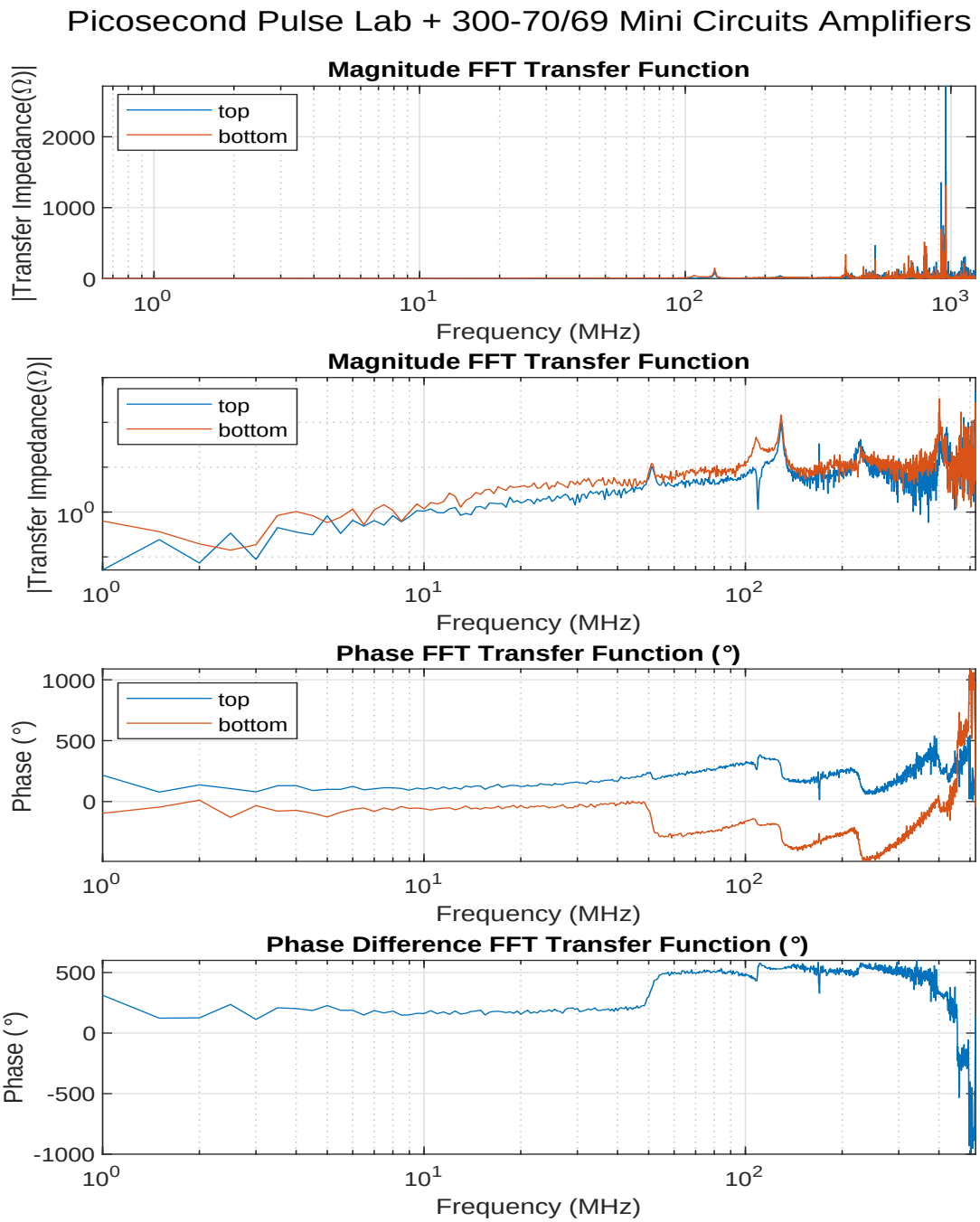

Figure 90: Mini Circuits Amplifier Bode diagram of Magnetic Antenna loops.

Applying a PD filter:

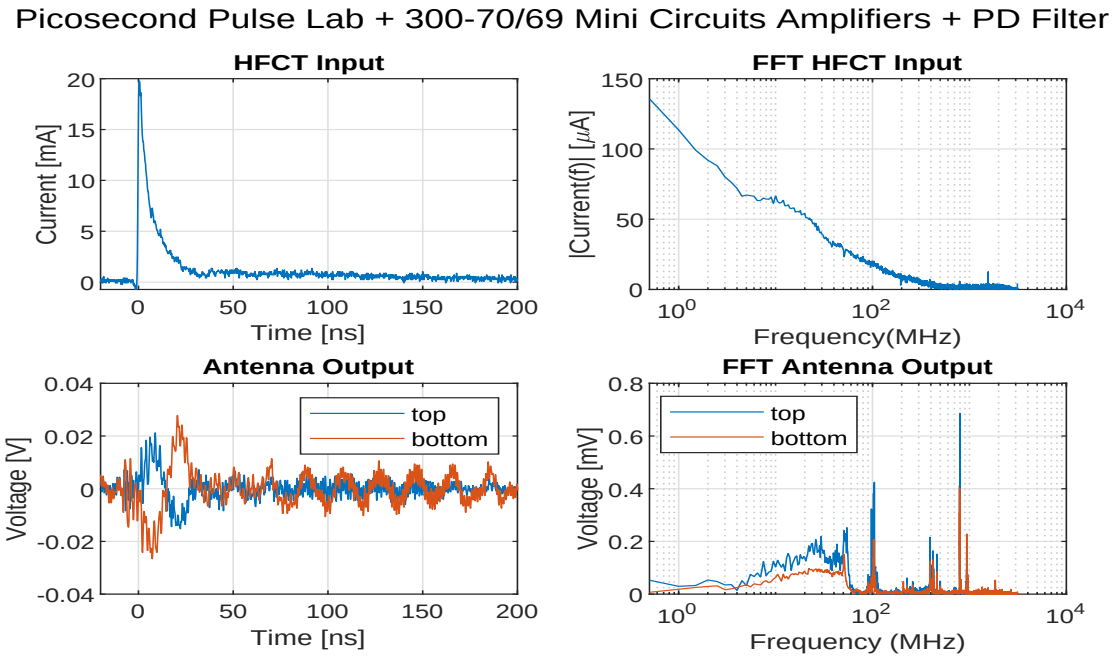

Figure 91: HFCT and Femto 300-70/69 Mini Circuits Amplifiers with PDFs Top and Bottom Loop Time Domain and Frequency Response of Magnetic Antenna to the PPLG pulse

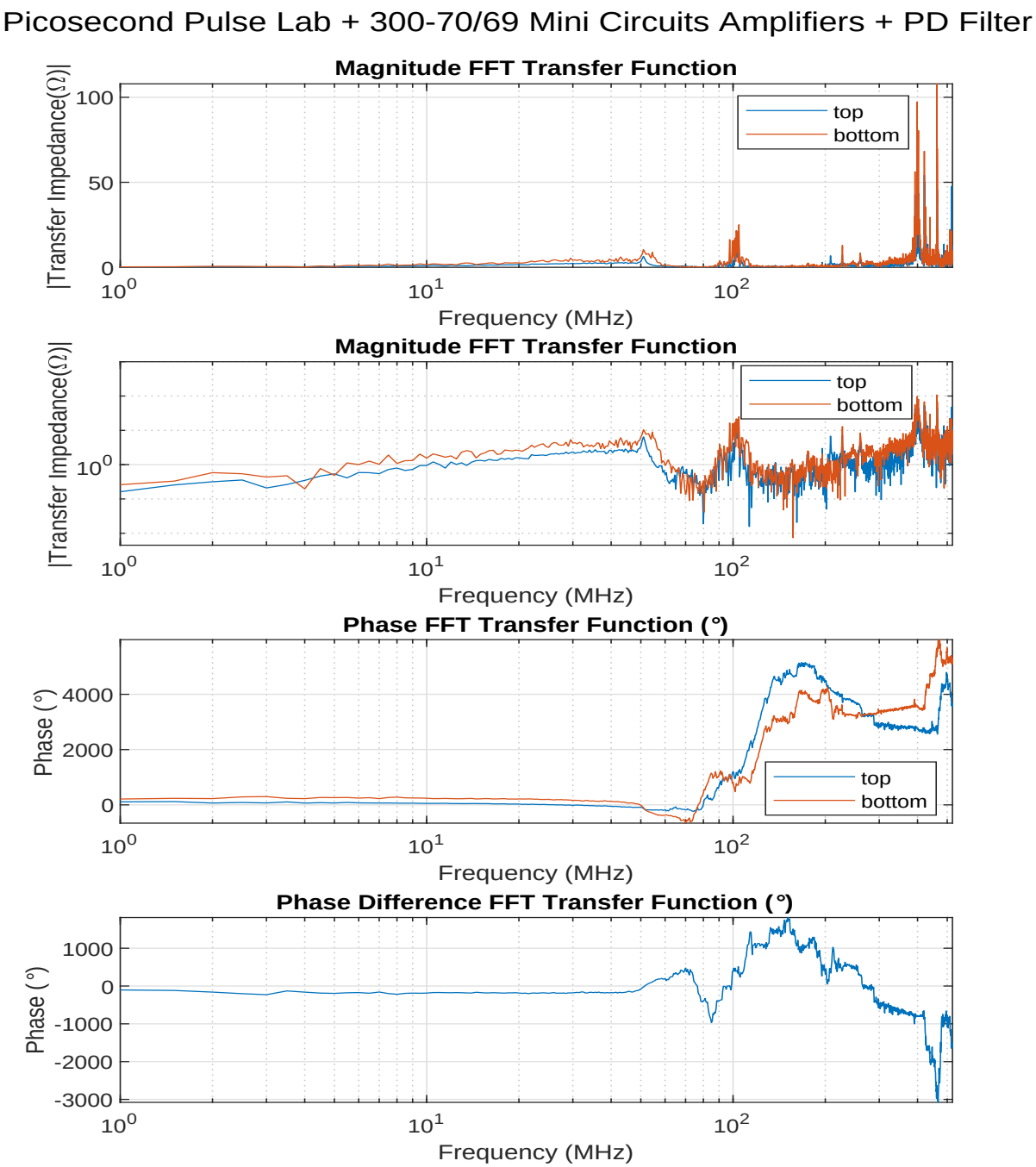

Figure 92: Mini Circuits Amplifier with PDF Bode diagram of Magnetic Antenna loops.

Using Cores - 42

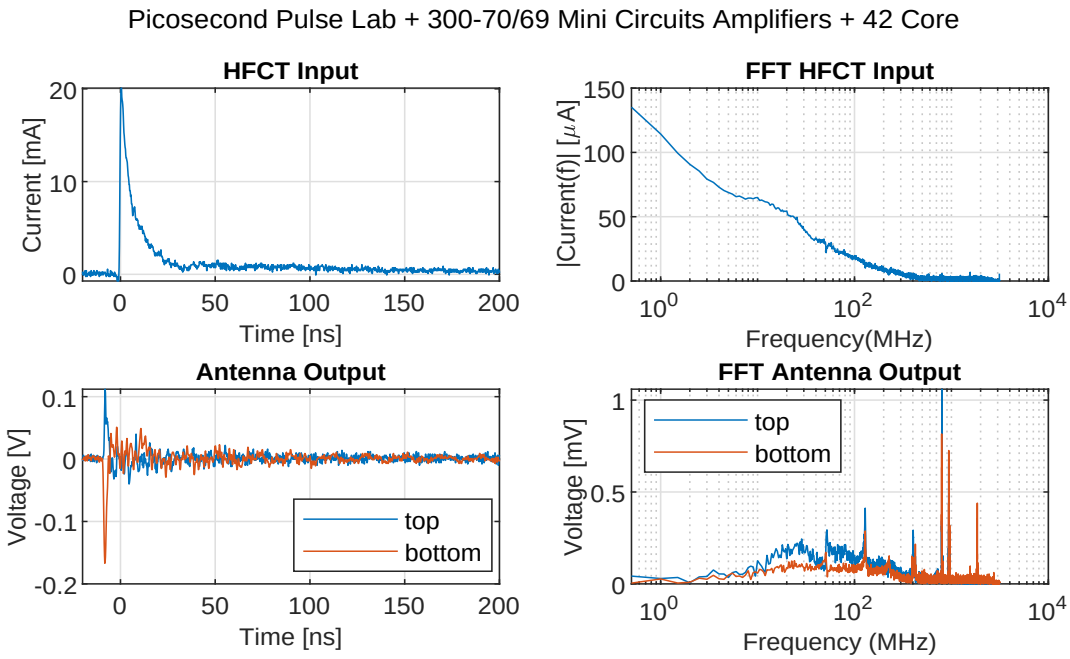

Figure 93: HFCT and Mini Circuits Amplifier with 42 Core Magnetic Antenna Top and Bottom Loop Response to pulse

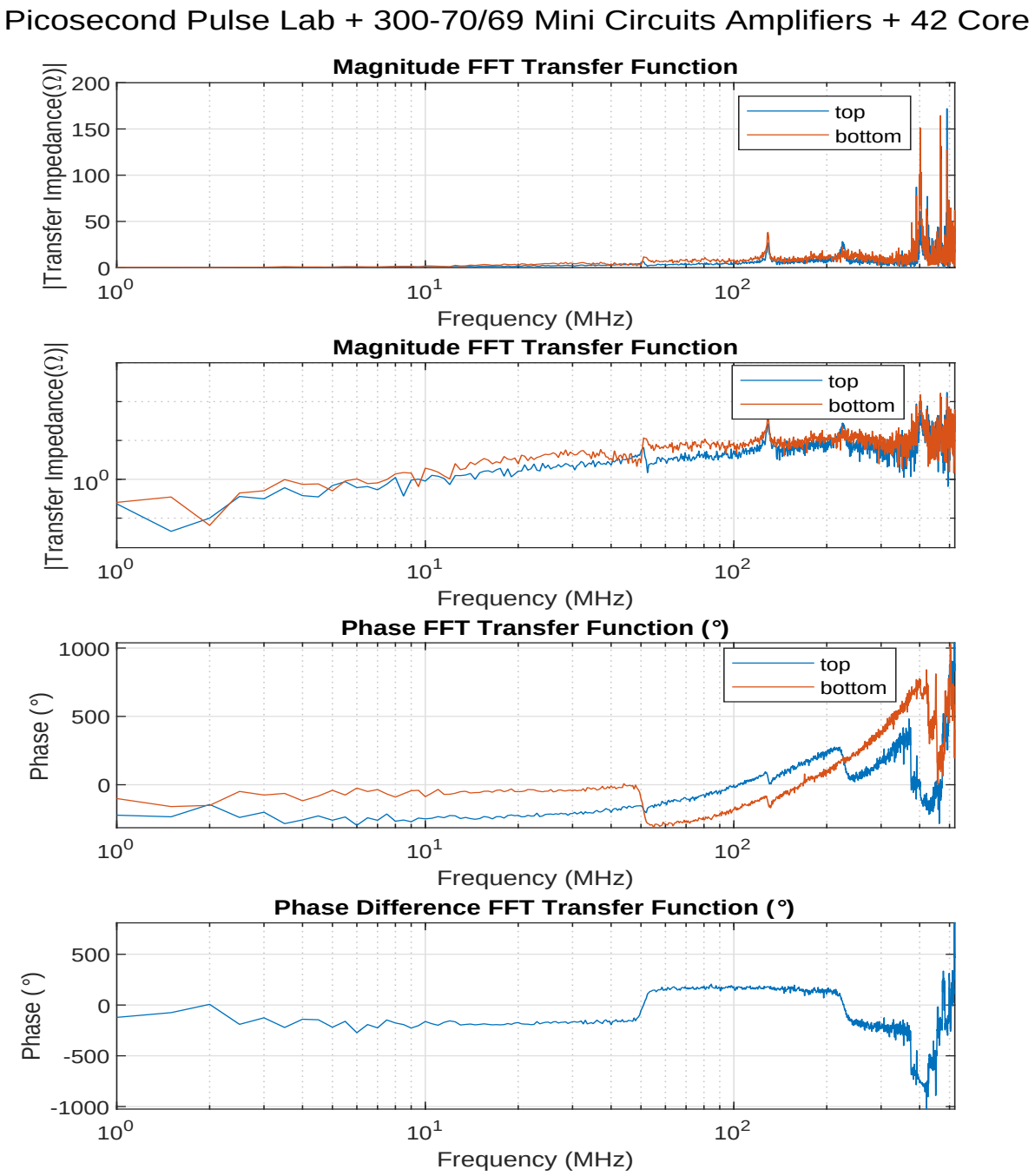

Figure 94: Mini Circuits Amplifier with 42 Core Bode diagram of Magnetic Antenna loops.

Using Cores - 72

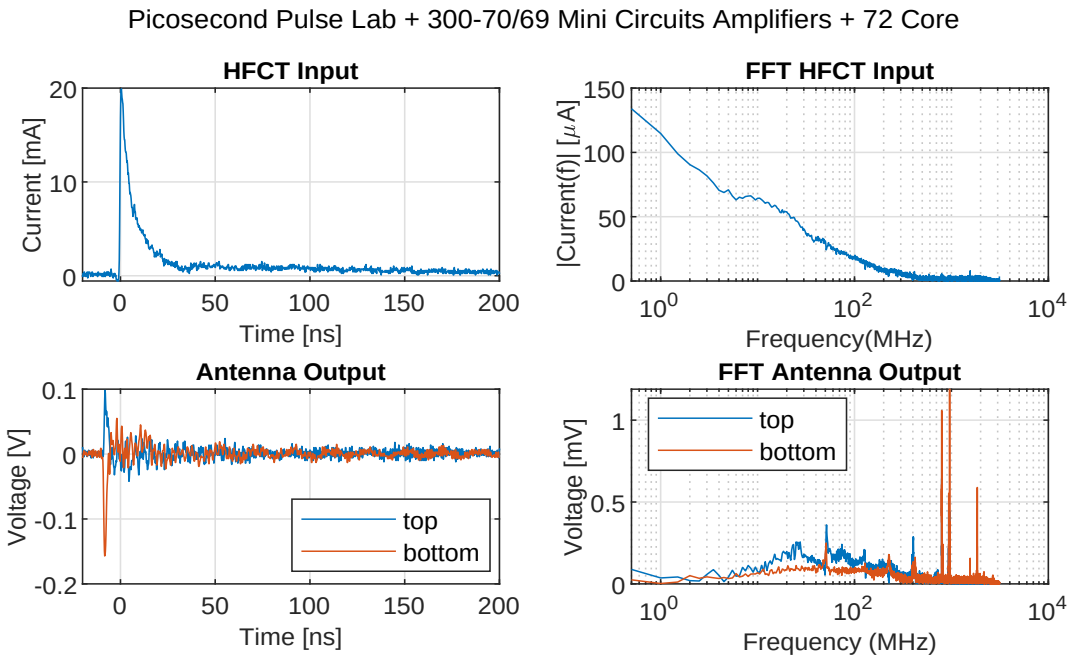

Figure 95: HFCT and Mini Circuits Amplifier with 72 Core Magnetic Antenna Top and Bottom Loop Response to pulse

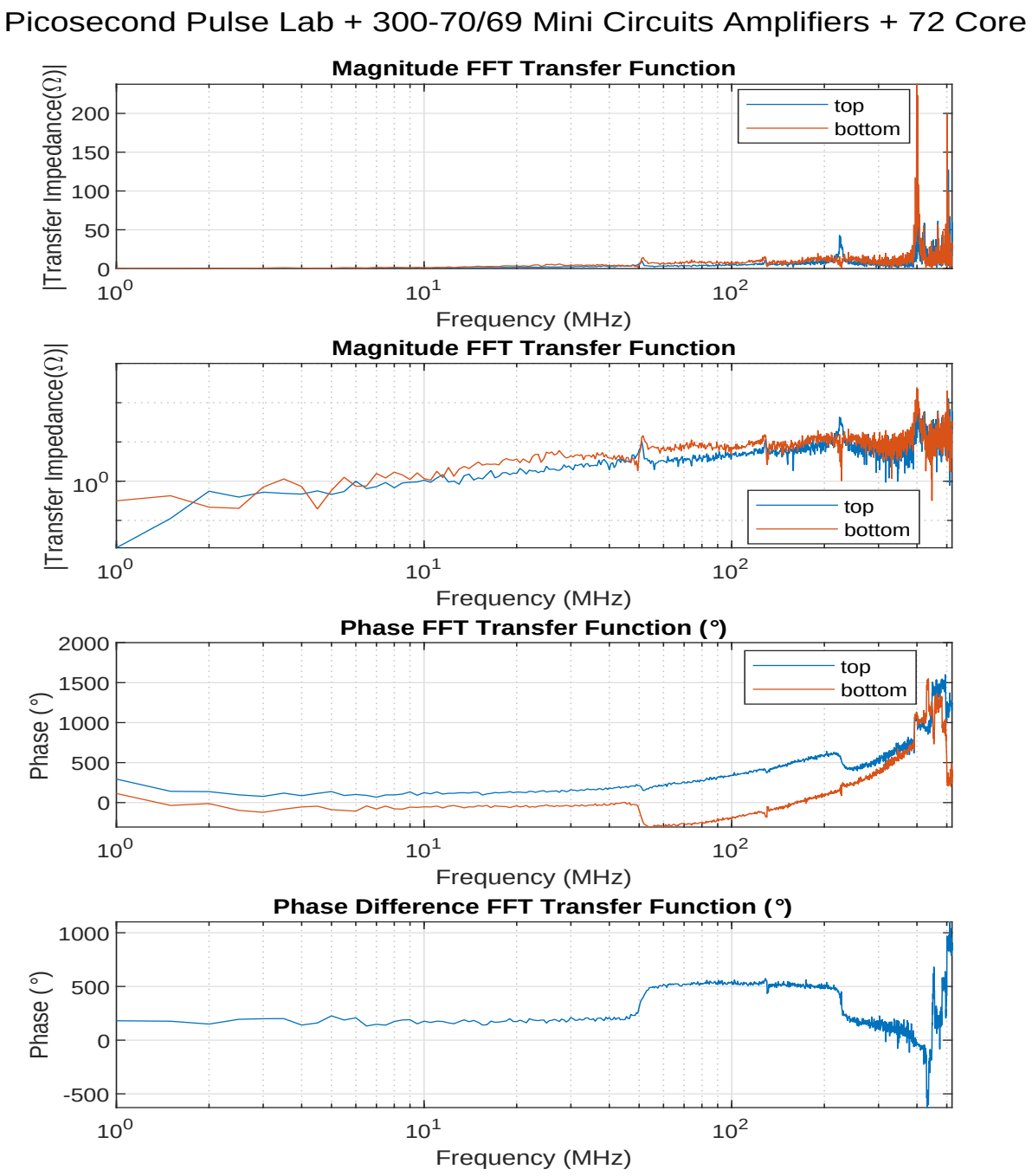

Figure 96: Mini Circuits Amplifier with 72 Core Bode diagram of Magnetic Antenna loops.

A.3 Antenna Plots Input/Output + Bode Workbench - Femto 400M-5k

A.3.1 Avalanche Nanosecond Pulse Generator

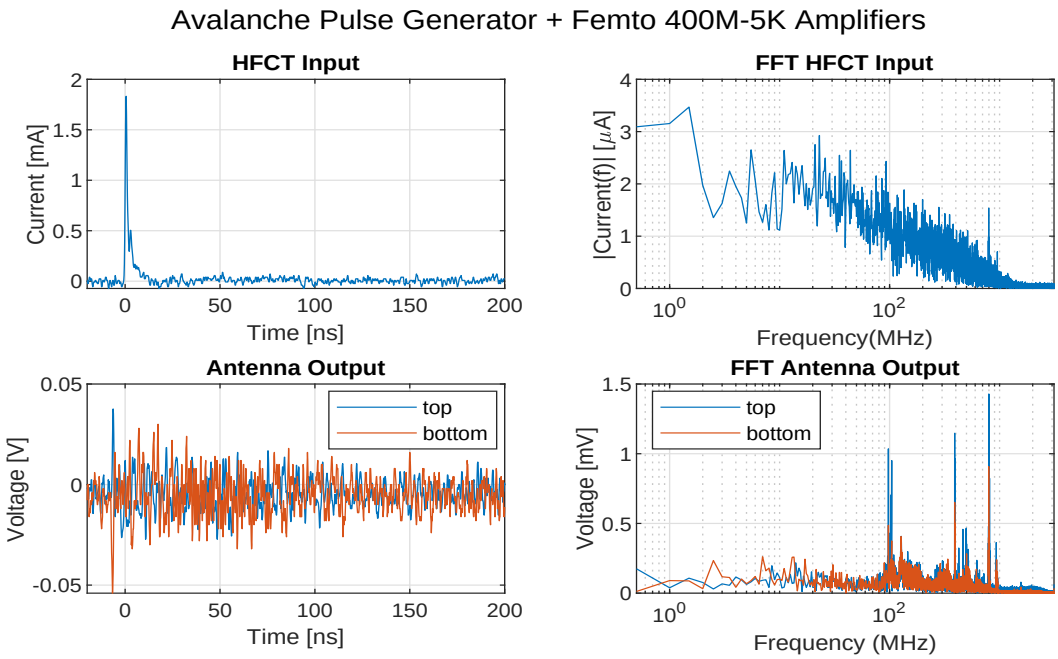

Figure 97: HFCT current (input) and 300-70/69 Mini Circuits Amplifiers Magnetic Antenna voltage (output) measurement in time domain and frequency domain for the top and bottom loop Response to the Avalanche Nanosecond Pulse

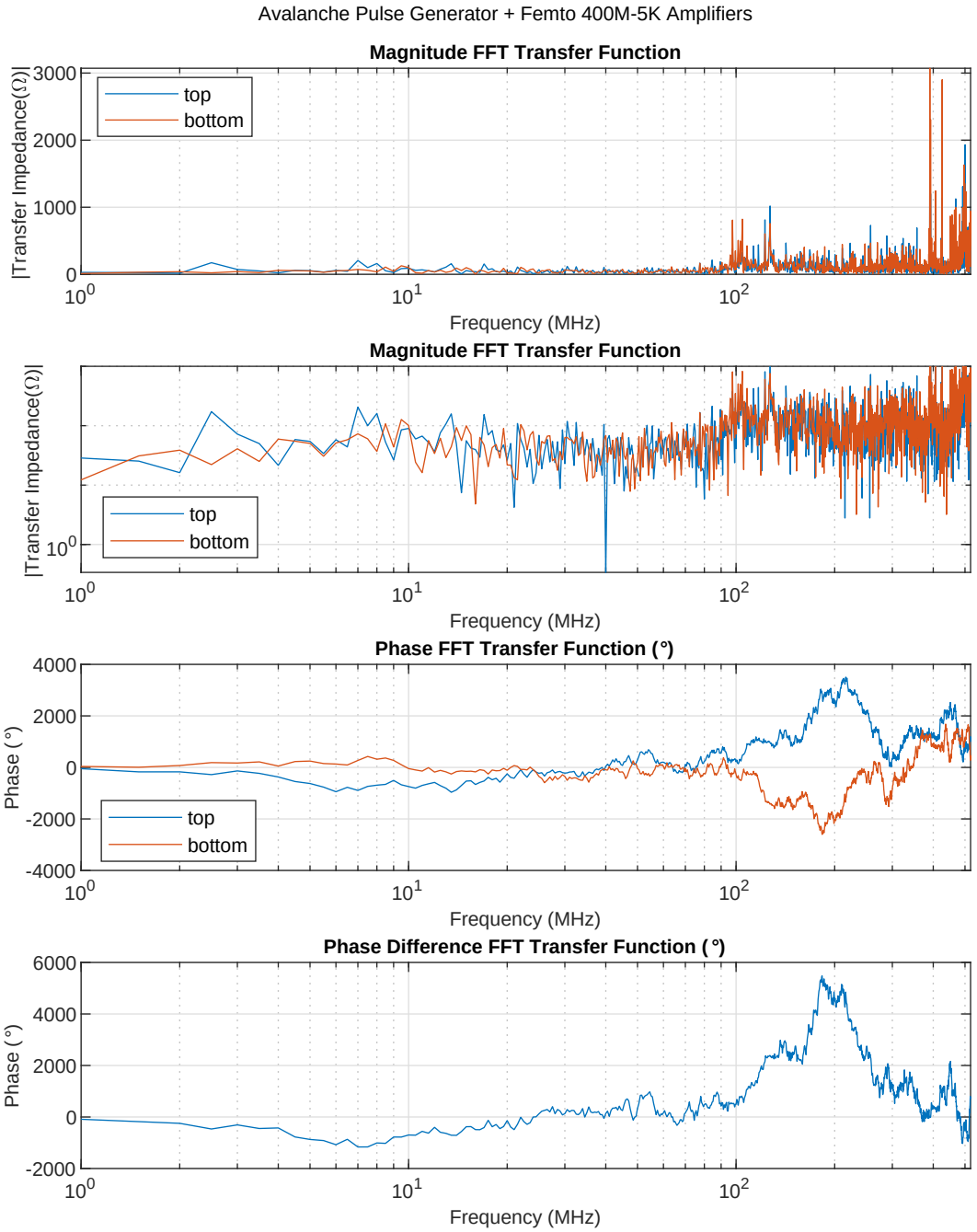

Figure 98: Frequency range until 250MHz of Mini Circuits Amplifier Bode diagram of Magnetic Antenna loops.

Using Cores-42

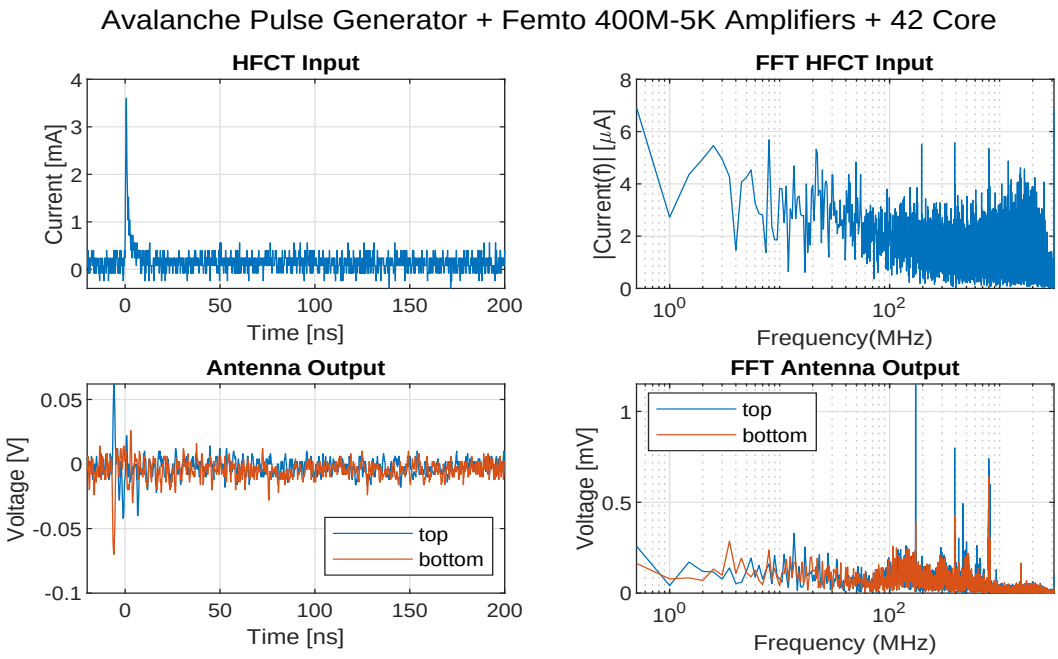

Figure 99: HFCT current (input) and 300-70/69 Mini Circuits Amplifiers with the 42 Cores Magnetic Antenna voltage (output) measurement in time domain and frequency domain for the top and bottom loop response to the Avalanche Nanosecond Pulse

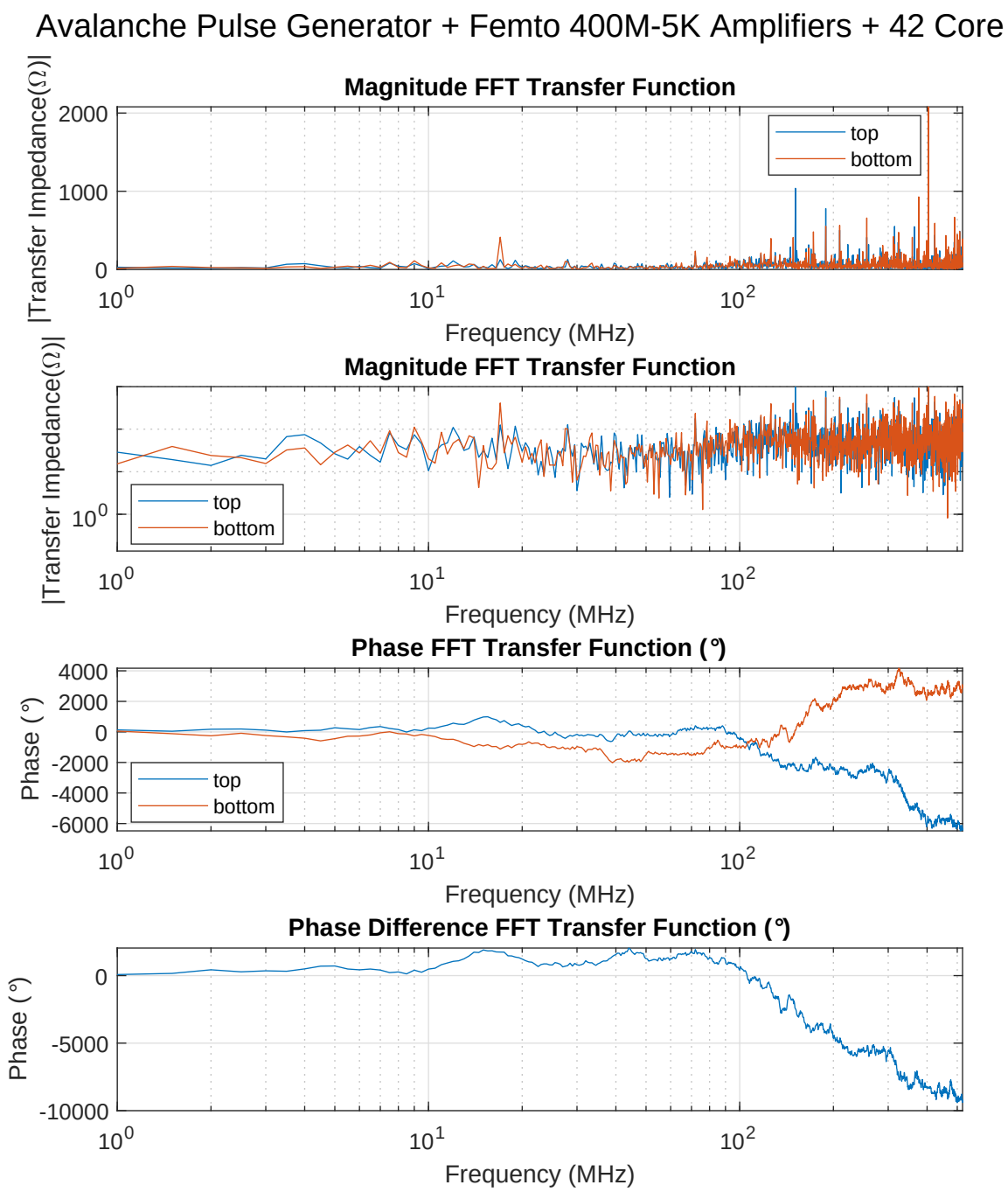

Figure 100: Mini Circuits Amplifier with 42 Core Bode diagram of Magnetic Antenna loops.

Using Cores-72

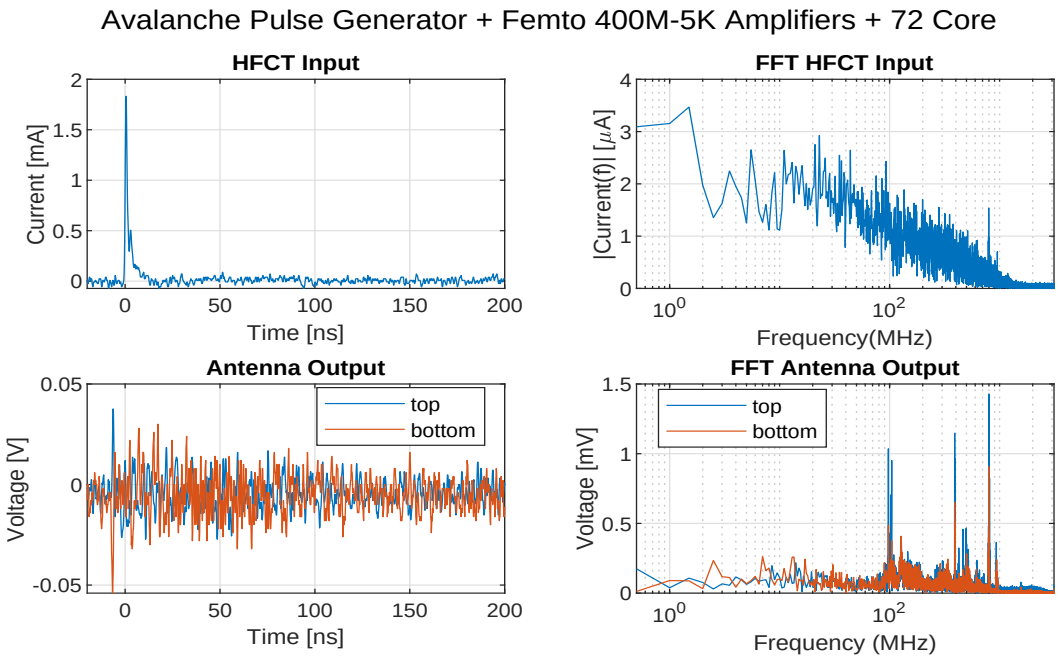

Figure 101: HFCT current (input) and 300-70/69 Mini Circuits Amplifiers with the 72 Cores Magnetic Antenna voltage (output) measurement in time domain and frequency domain for the top and bottom loop response to the Avalanche Nanosecond Pulse

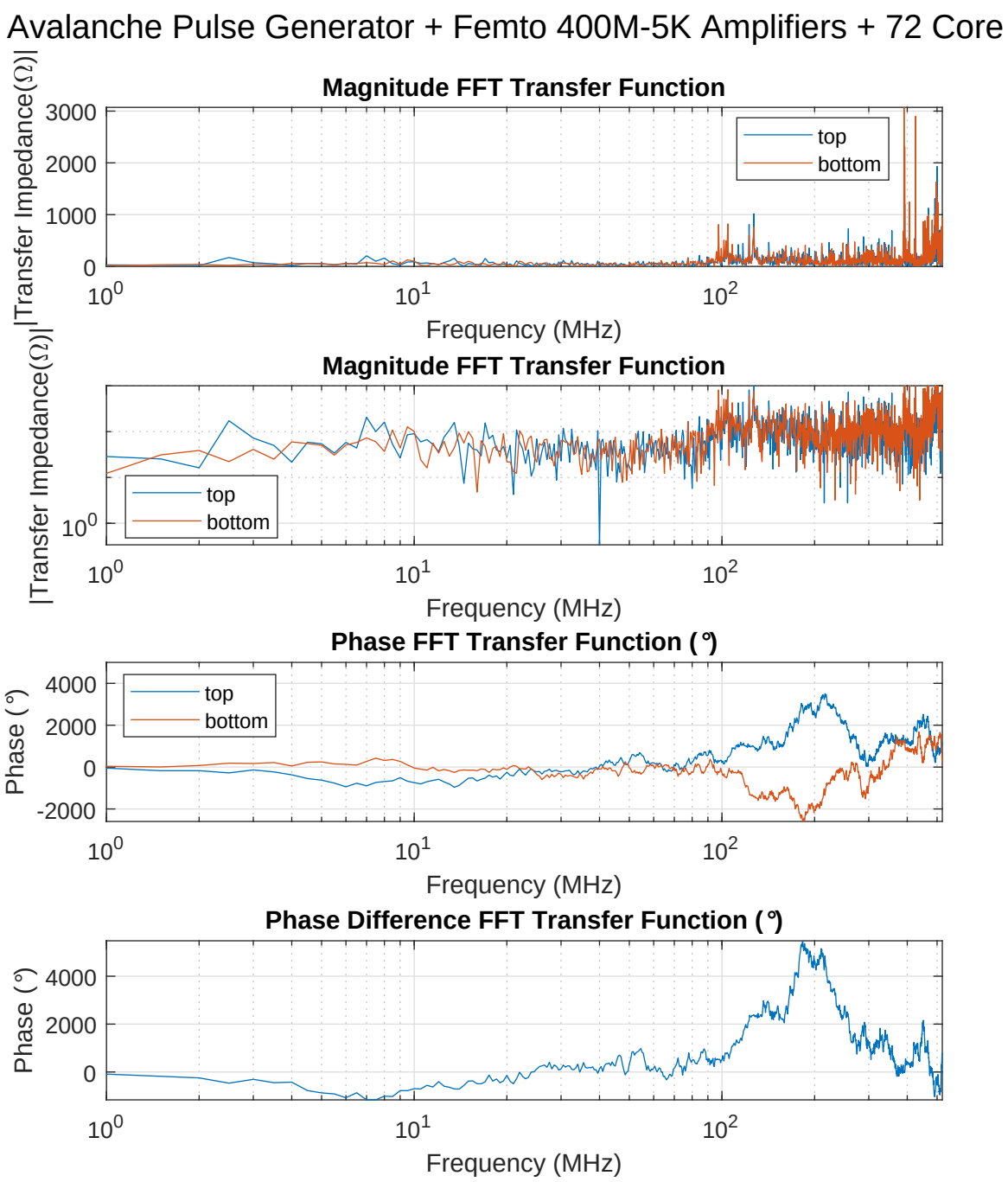

Figure 102: Mini Circuits Amplifier with 72 Core Bode diagram of Magnetic Antenna loops.

A.3.2 Picosecond Pulse Labs Generator

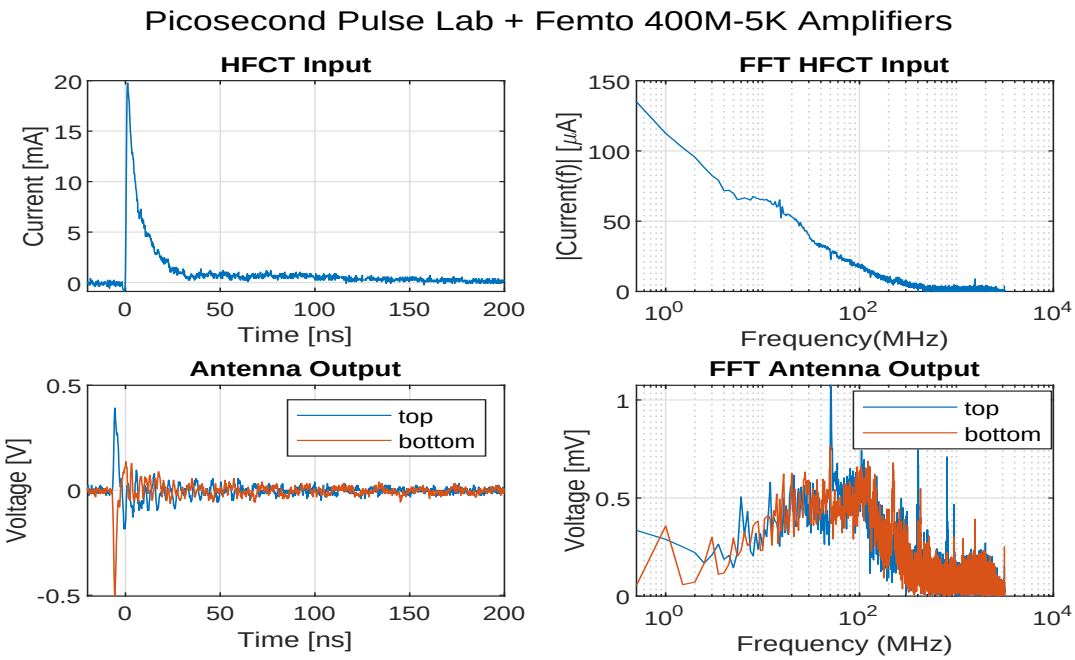

Figure 103: HFCT current (input) and 300-70/69 Mini Circuits Amplifiers Magnetic Antenna voltage (output) measurement in time domain and frequency domain for the top and bottom loop Response to the Avalanche Nanosecond Pulse

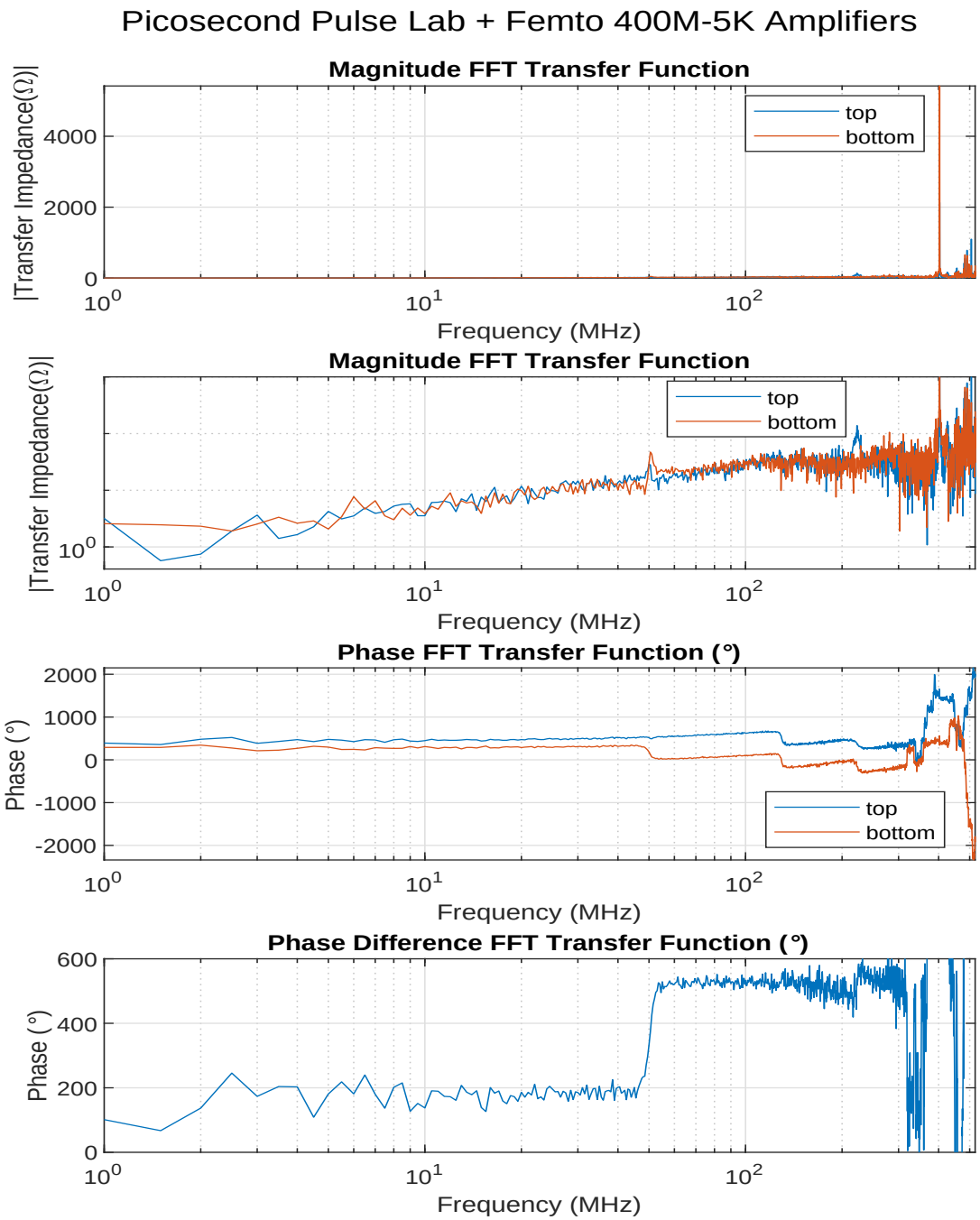

Figure 104: Frequency range until 250MHz of Mini Circuits Amplifier Bode diagram of Magnetic Antenna loops.

Using Cores-42

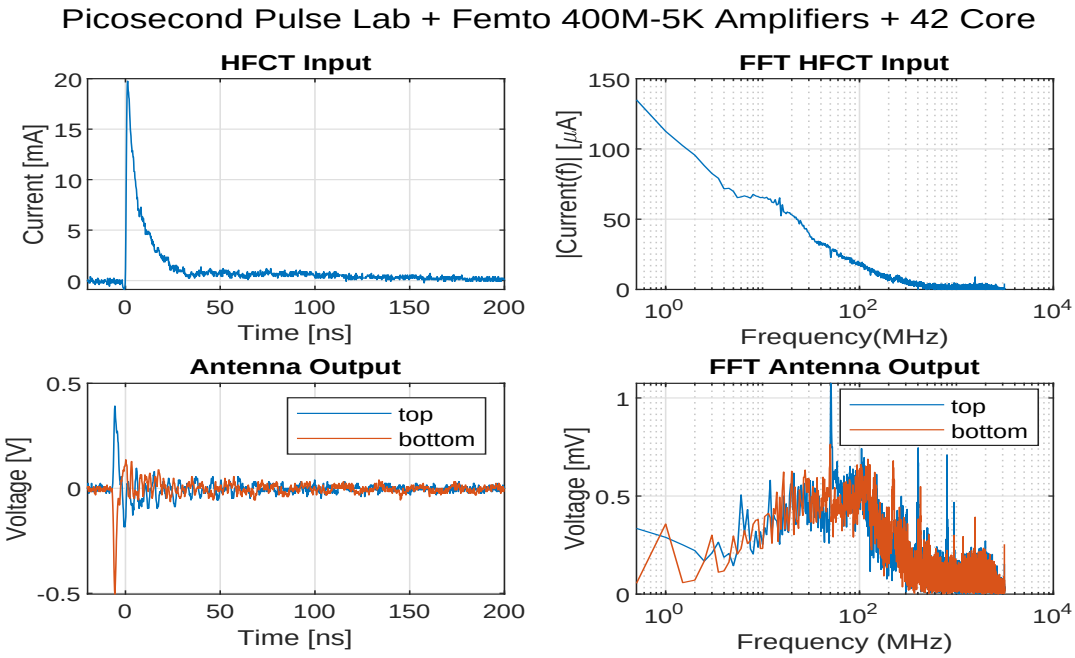

Figure 105: HFCT current (input) and 300-70/69 Mini Circuits Amplifiers with the 42 Cores Magnetic Antenna voltage (output) measurement in time domain and frequency domain for the top and bottom loop response to the Avalanche Nanosecond Pulse

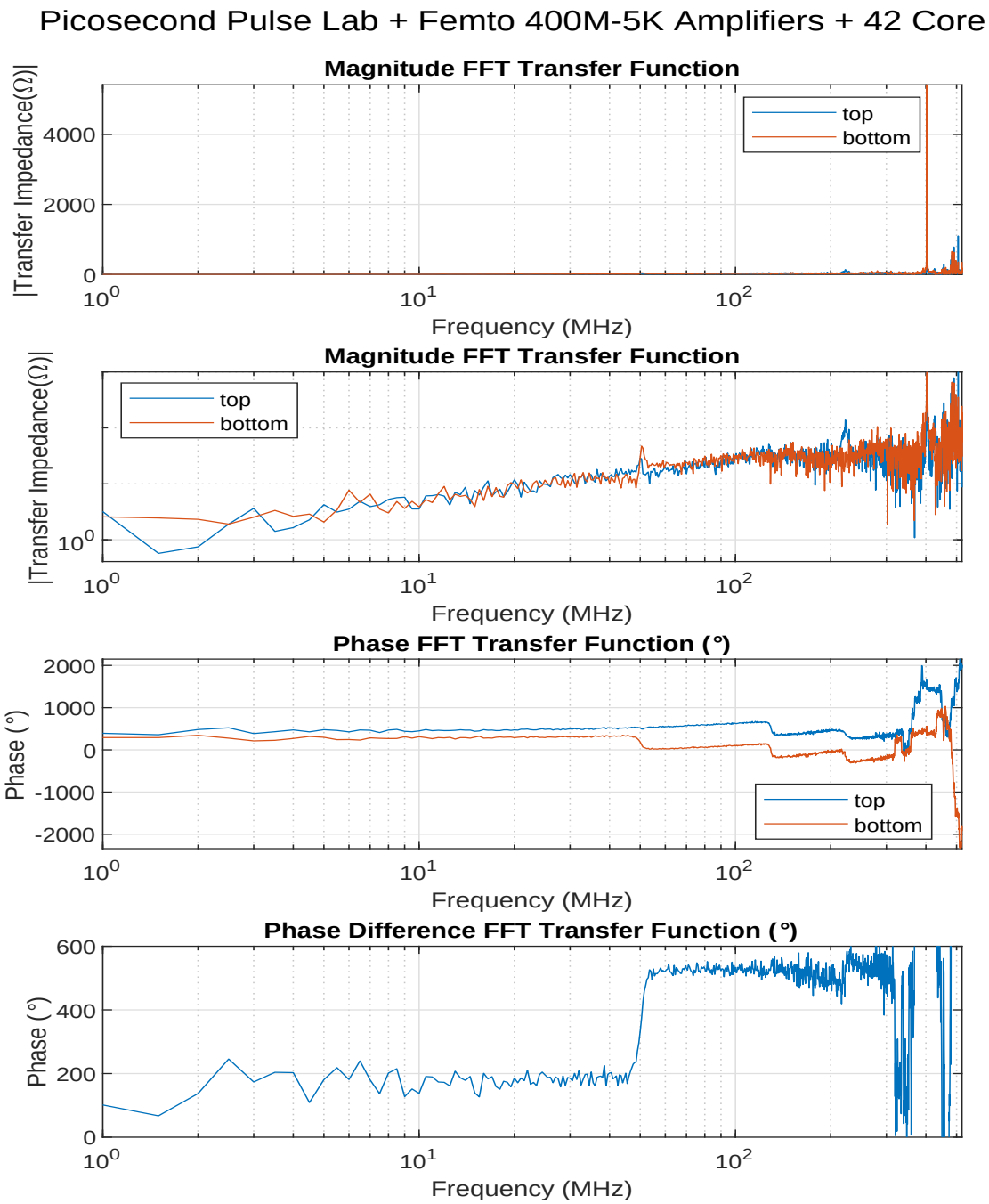

Figure 106: Mini Circuits Amplifier with 42 Core Bode diagram of Magnetic Antenna loops.

Using Cores-72

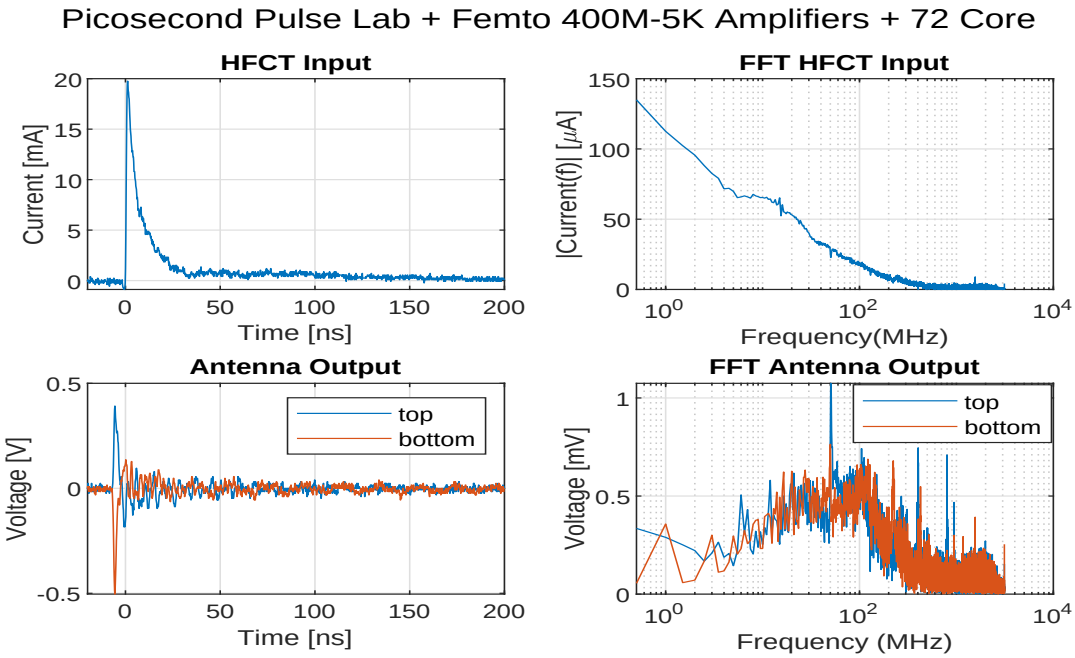

Figure 107: HFCT current (input) and 300-70/69 Mini Circuits Amplifiers with the 72 Cores Magnetic Antenna voltage (output) measurement in time domain and frequency domain for the top and bottom loop response to the Avalanche Nanosecond Pulse

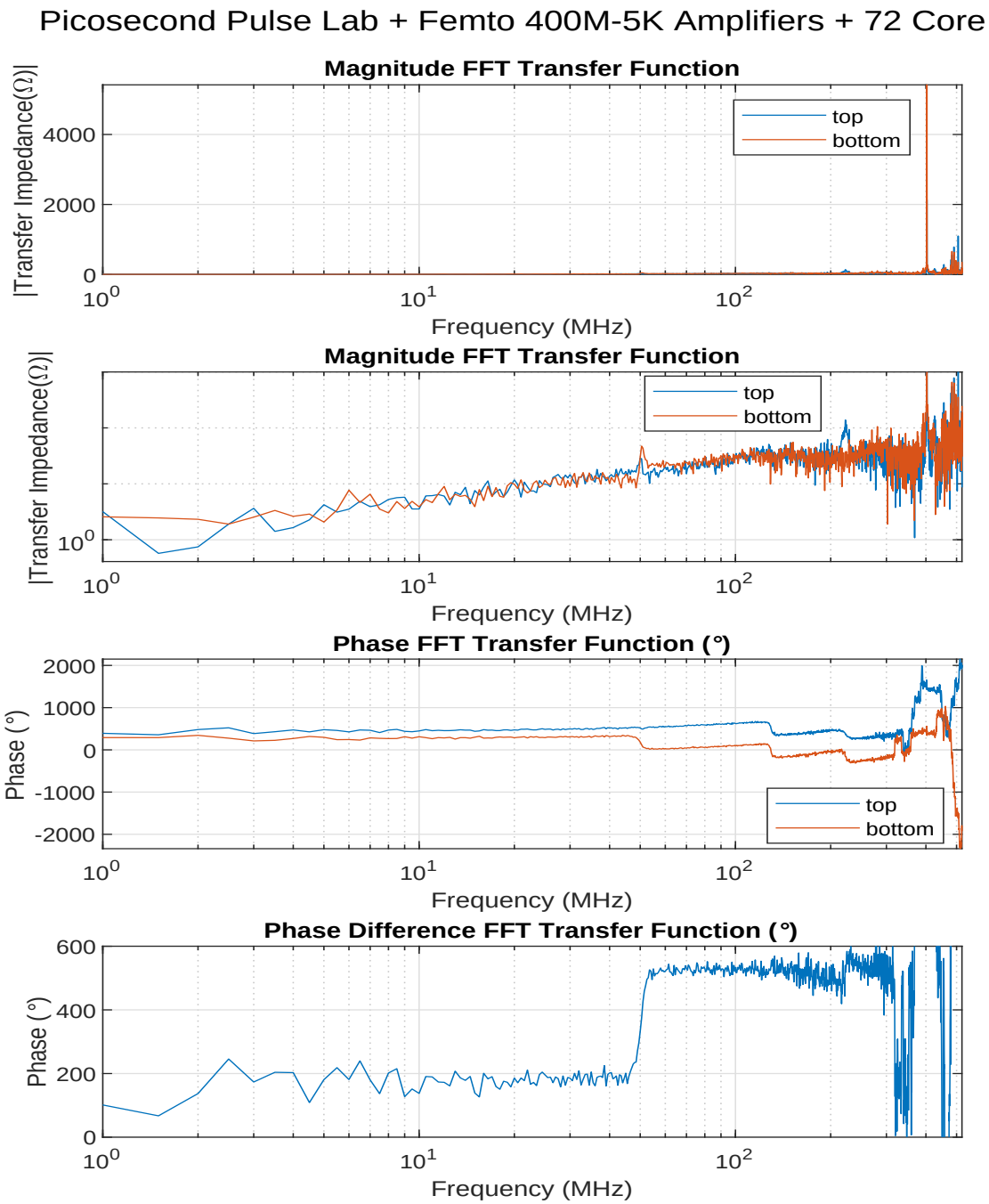

Figure 108: Mini Circuits Amplifier with 72 Core Bode diagram of Magnetic Antenna loops.

A.4 Magnitude Response Core Comparison Plots

A.4.1 Antenna Plots Input/Output + Bode Workbench - Femto 40M-100K

Avalanche Pulse Generator

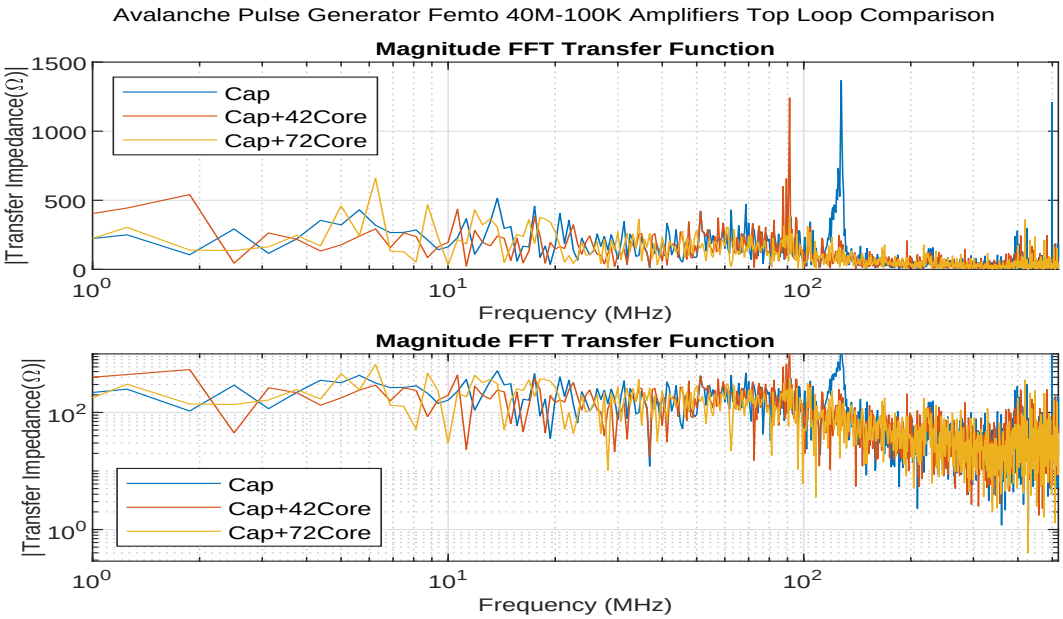

Figure 109: Comparing top loop transfer impedance of base, core42, and core 72 with the Avalanche Nanosecond Pulse Generator and Femto 40M-100K Amplifier

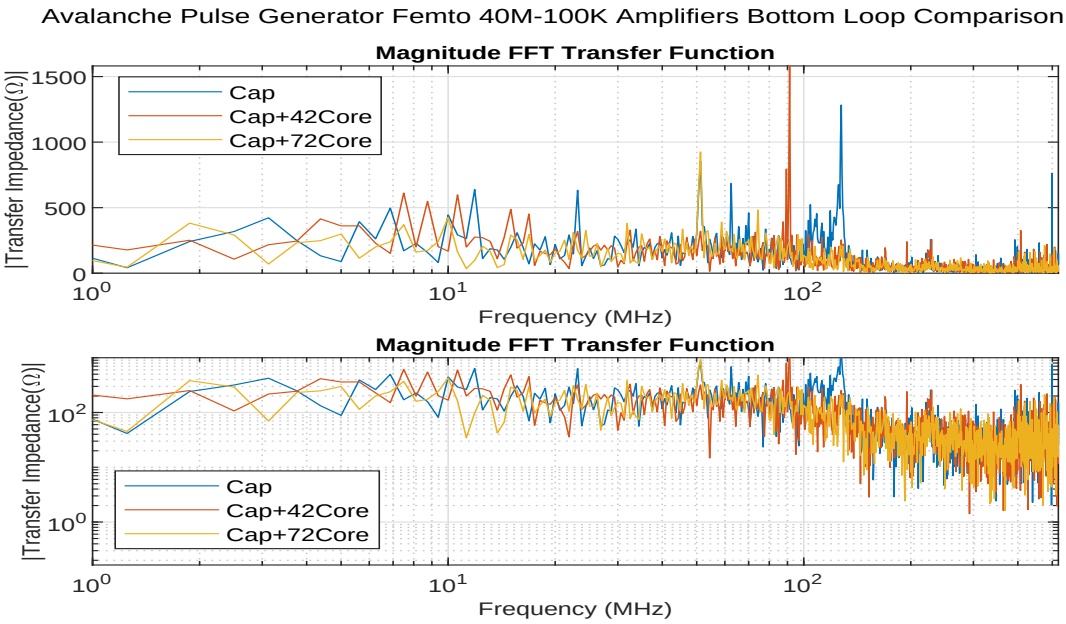

Figure 110: Comparing bottom loop transfer impedance of base, core42, and core 72 with the Avalanche Nanosecond Pulse Generator and Femto 40M-100K Amplifier

Picosecond Pulse Generator

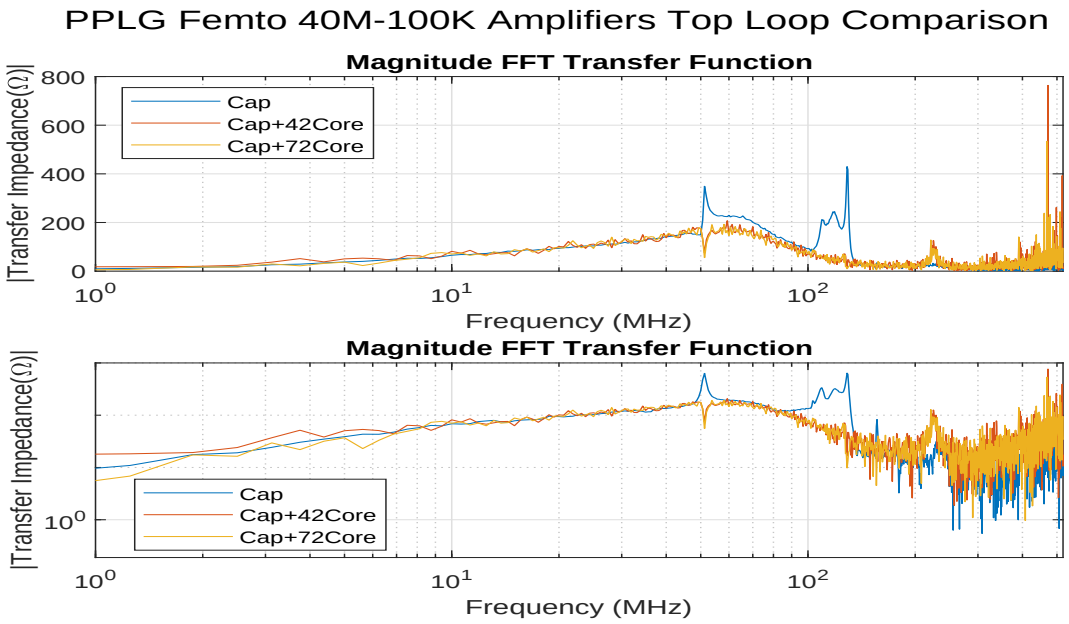

Figure 111: Comparing top loop transfer impedance of base, core42, and core 72 with the Picosecond Pulse Lab Generator and Femto 40M-100K Amplifier

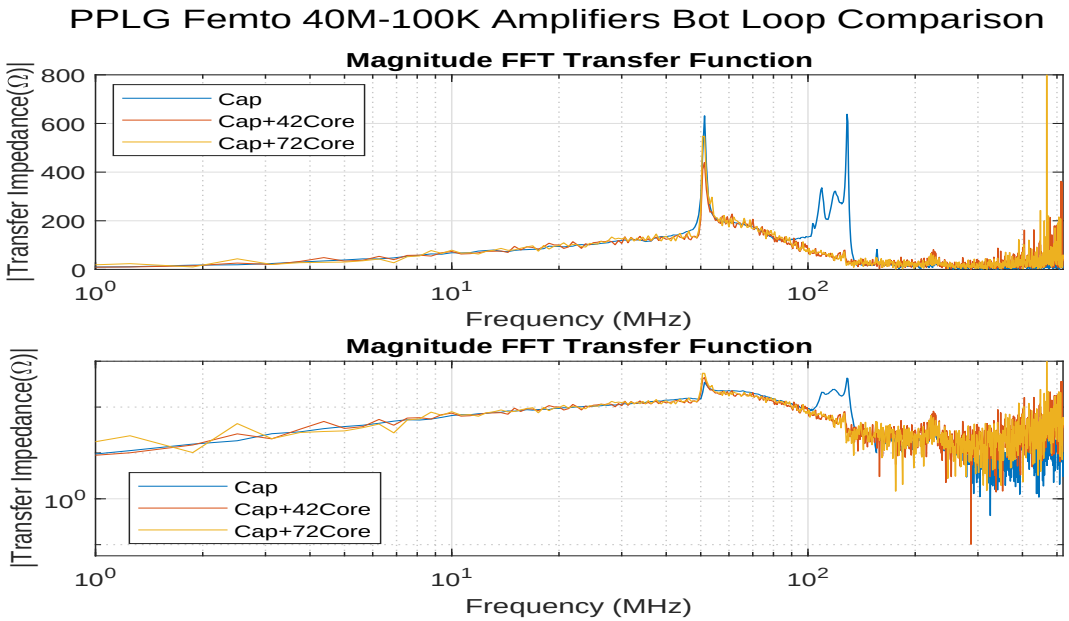

Figure 112: Comparing bottom loop transfer impedance of base, core42, and core 72 with the Picosecond Pulse Lab Generator and Femto 40M-100K Amplifier

A.4.2 70/69 Minicircuits Amplifier

Avalanche Pulse Generator

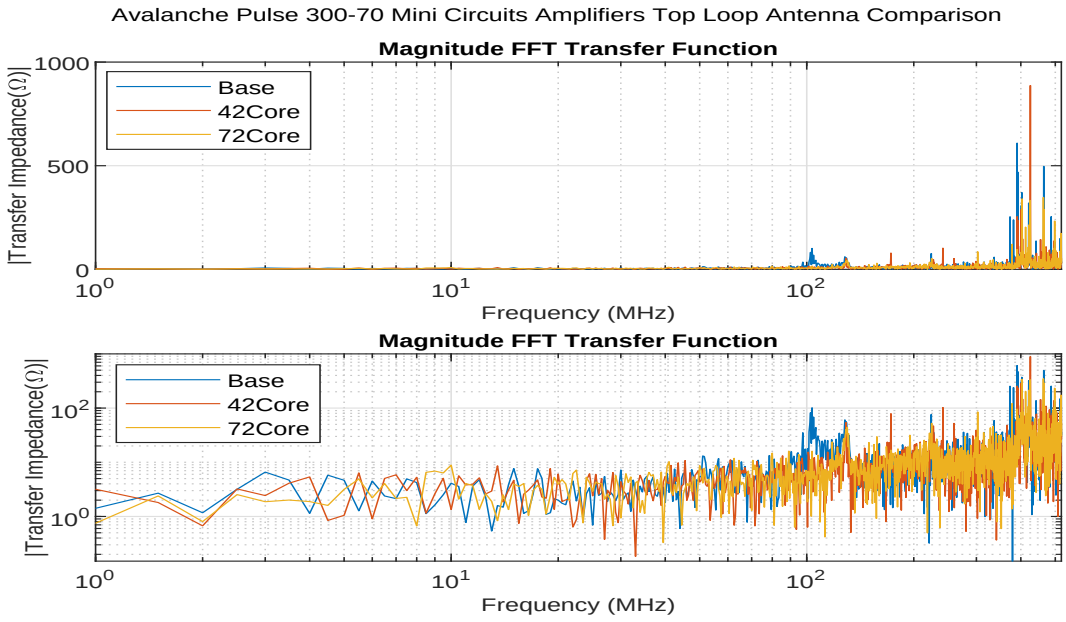

Figure 113: Comparing top loop transfer impedance of base, core42, and core 72 with the Picosecond Pulse Lab Generator and 300-70 Mini Circuits Amplifier

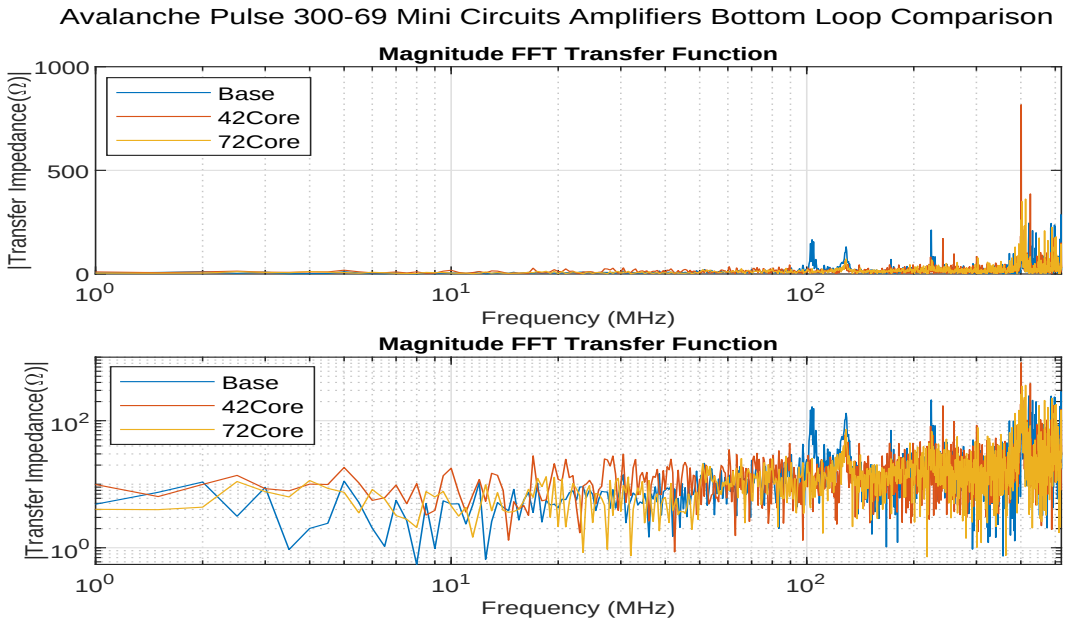

Figure 114: Comparing bottom loop transfer impedance of base, core42, and core 72 with the Picosecond Pulse Lab Generator and 300-69 Mini Circuits Amplifier

Picosecond Pulse Generator

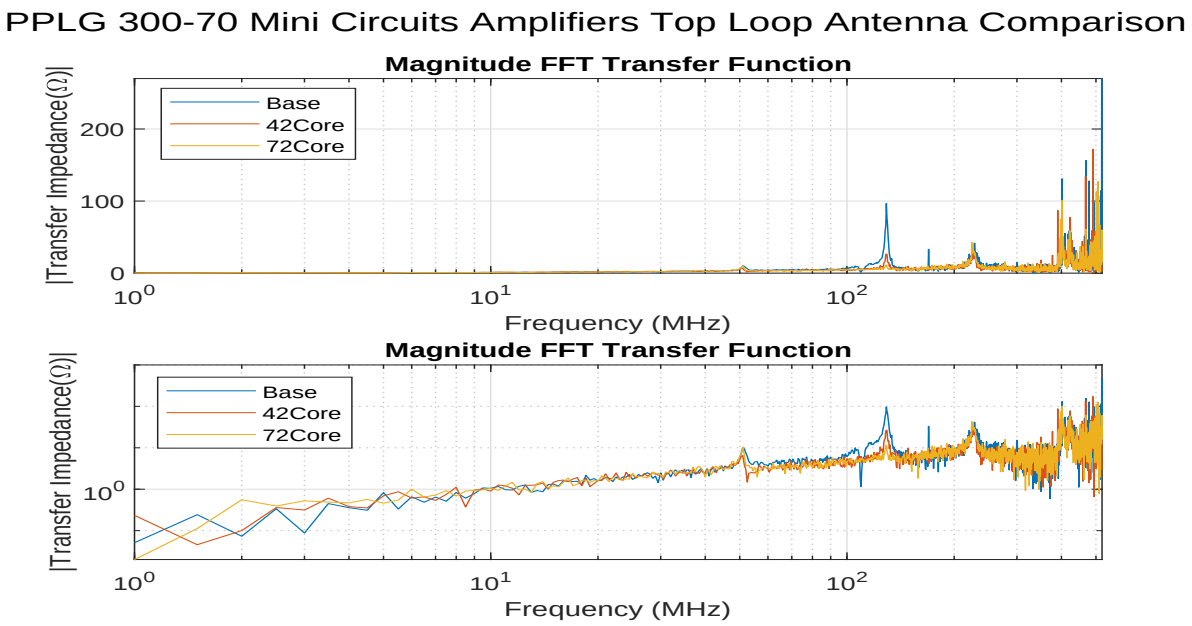

Figure 115: Comparing top loop transfer impedance of base, core42, and core 72 with the Picosecond Pulse Lab Generator and 300-70 Mini Circuits Amplifier

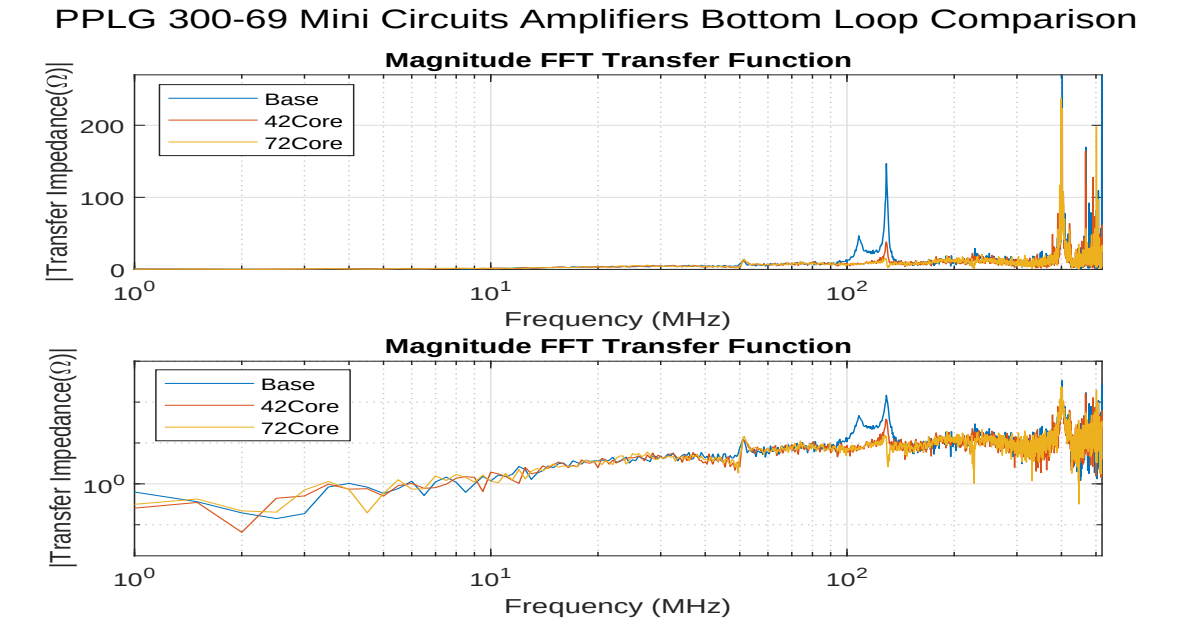

Figure 116: Comparing bottom loop transfer impedance of base, core42, and core 72 with the Picosecond Pulse Lab Generator and 300-69 Mini Circuits Amplifier

A.4.3 Femto 400M-5K

Avalanche Pulse Generator

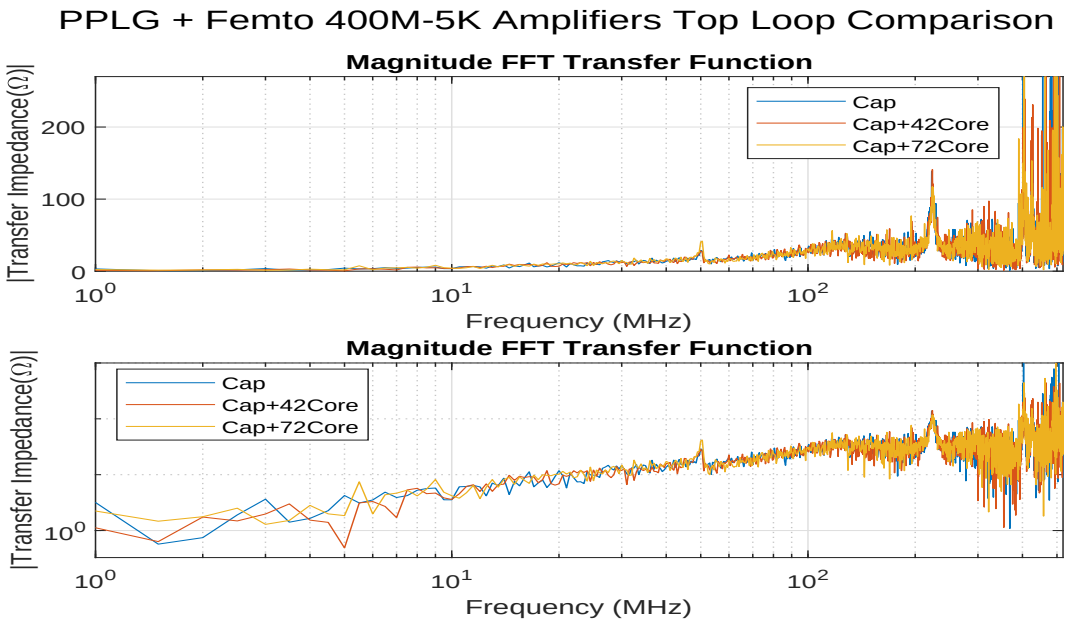

Figure 117: Comparing top loop transfer impedance of base, core42, and core 72 with the Picosecond Pulse Lab Generator and Femto 400M-5K Amplifier

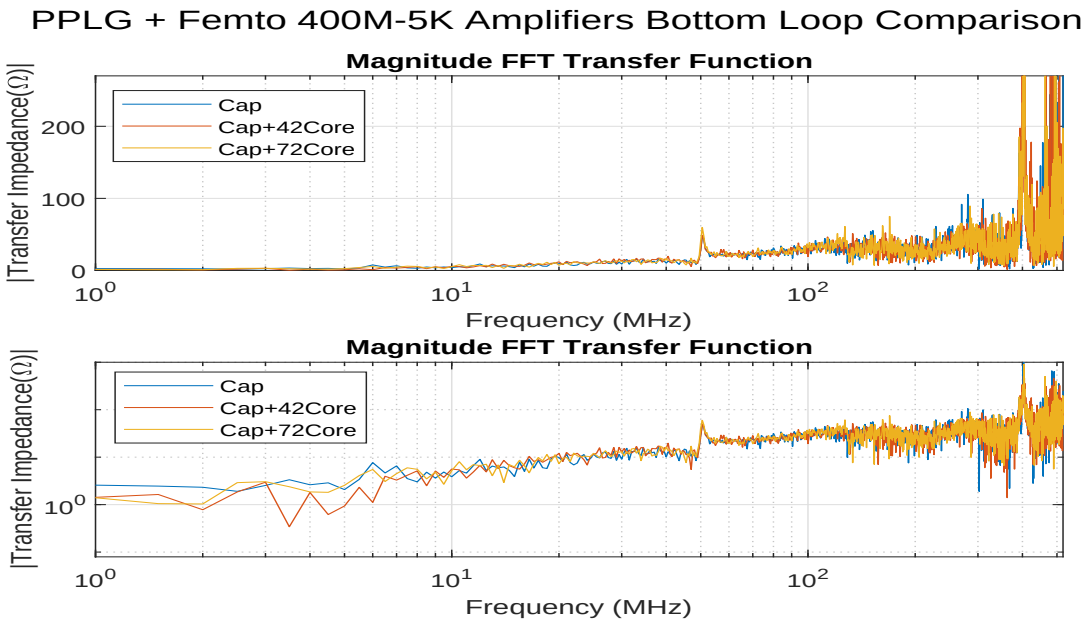

Figure 118: Comparing top loop transfer impedance of base, core42, and core 72 with the Picosecond Pulse Lab Generator and Femto 400M-5K Amplifier

Picosecond Pulse Generator

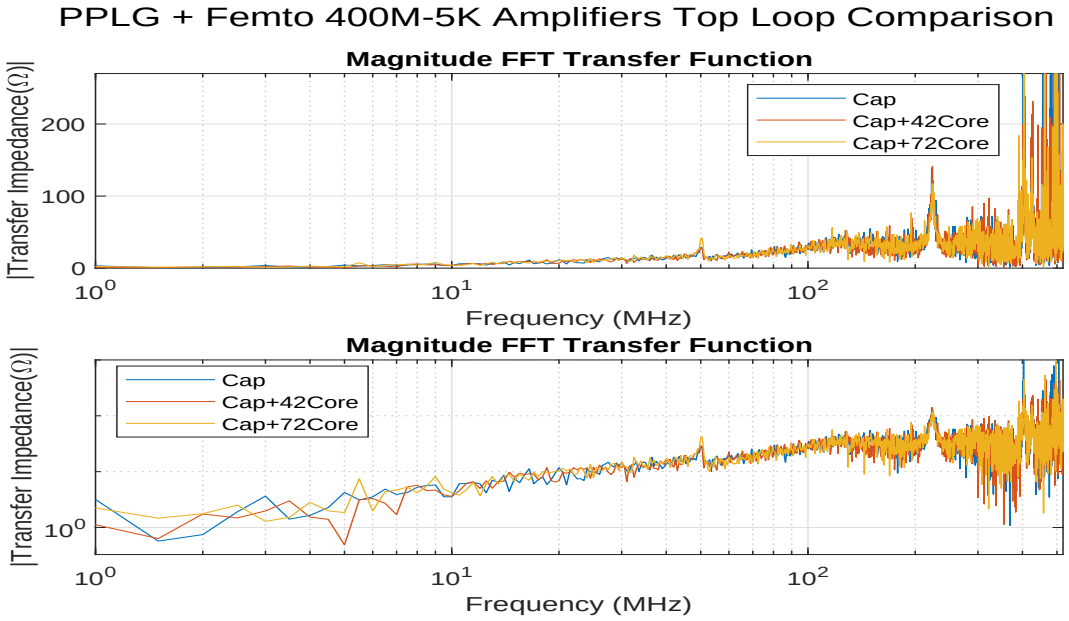

Figure 119: Comparing top loop transfer impedance of base, core42, and core 72 with the Picosecond Pulse Lab Generator and Femto 400M-5K Amplifier

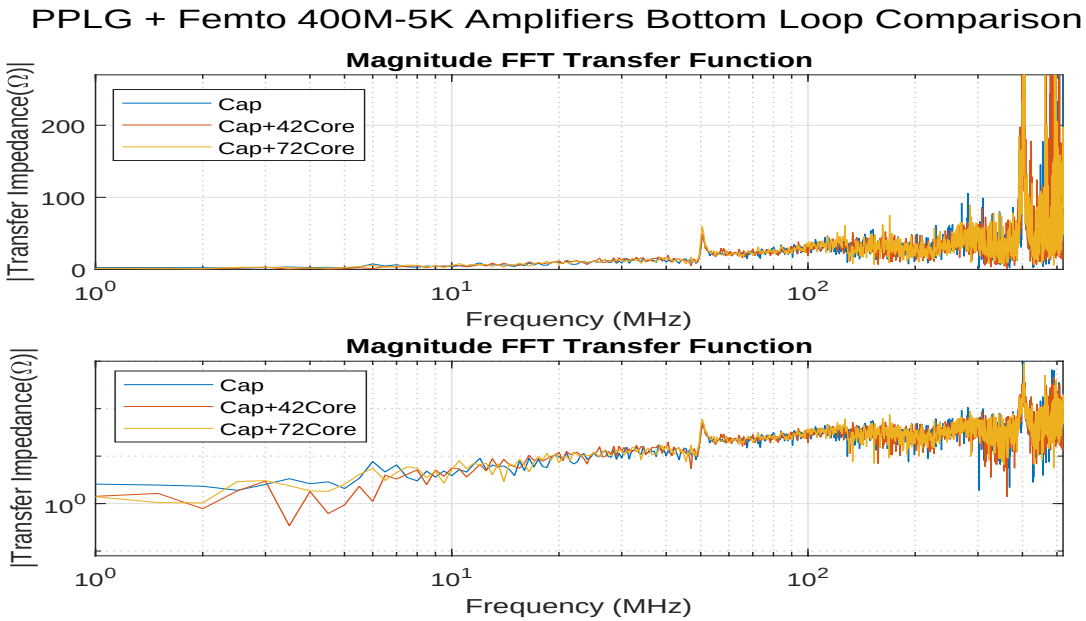

Figure 120: Comparing top loop transfer impedance of base, core42, and core 72 with the Picosecond Pulse Lab Generator and Femto 400M-5K Amplifier

A.5 Impedance matching

To understand the phenomena of wave reflections it is important to investigate basic transmission and reflection theory. The reflection coefficient Γ is calculated in Equation(11). Where Z1 is the characteristic impedance of the medium in which the wave approaches the boundary and Z2 is the opposite face's characteristic impedance. The Transmission coefficient is calculated in Equation(12).

$$\Gamma = \frac{Z_2 - Z_1}{Z_2 + Z_1} \tag{11}$$

$$T = 1 + \Gamma = \frac{2 \cdot Z_2}{Z_2 + Z_1} \tag{12}$$

No reflections are desired. Hence by perfectly matching Z1 and Z2 the reflection coefficient is 0 and thus no reflections will occur.
The characteristic impedance is calculated through deriving the Kirchoff Current Law (KCL) equations of the transmission line model as shown in Figure 121. The KCL equations give rise to the telegraph equations for a transmission line which can be expressed to solve for the characteristic impedance Z_0.

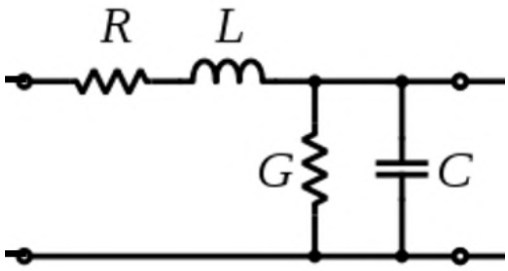

Figure 121: Lumped Transmission line model [19]

The characteristic impedance Z_{GIS} of the coaxial structure is

$$Z_{GIS} = \sqrt{\frac{R + j\omega L}{G + j\omega C}} \approx \sqrt{\frac{L}{C}} = \frac{1}{2\pi}\sqrt{\frac{\mu}{\epsilon}} \ln \frac{D}{d} \tag{13}$$

where the distributed circuit parameters are: L, the inductance, C, the capacitance, R, the resistance and G, the conductance. The ω is the angular frequency. The resistance and conductance of the conductor used is negligible and hence the approximation in Equation(13) is valid showing a frequency independence and geometrical dependance.

A.6 Localization Methods Landscape Histograms

Please note: due to the large spread in some outliers for the x-axis values the figure appears to be low-resolution at first glance. The image is a encapsulated postscript vector file and can indefinitely be zoomed into for higher resolution and clarity. Some frequency bins are expanded to 0.46 m to ensure the fit of the plots on the page.

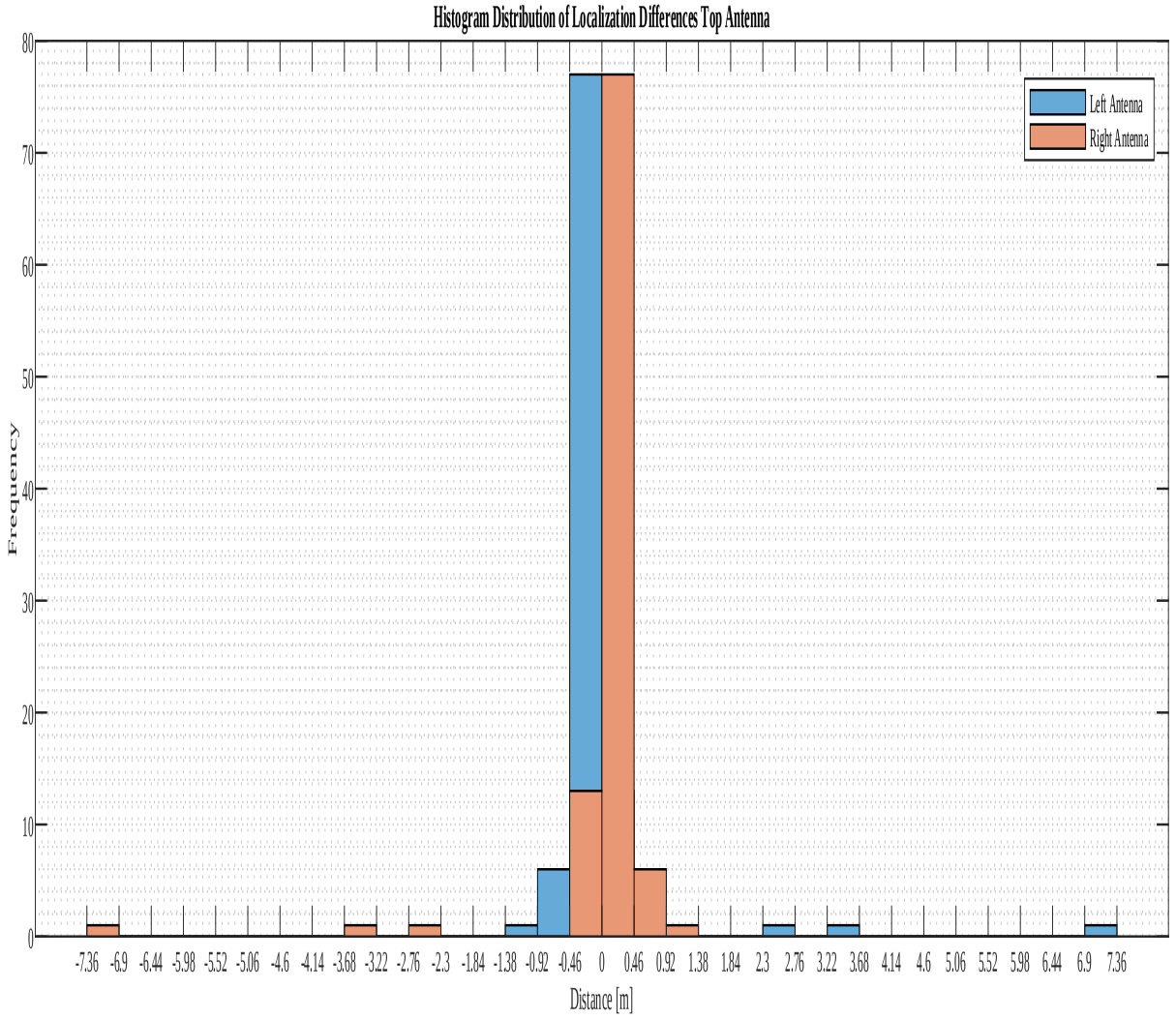

Figure 122: TPD Method Histogram of Distance Distribution of Top Antenna - Location B

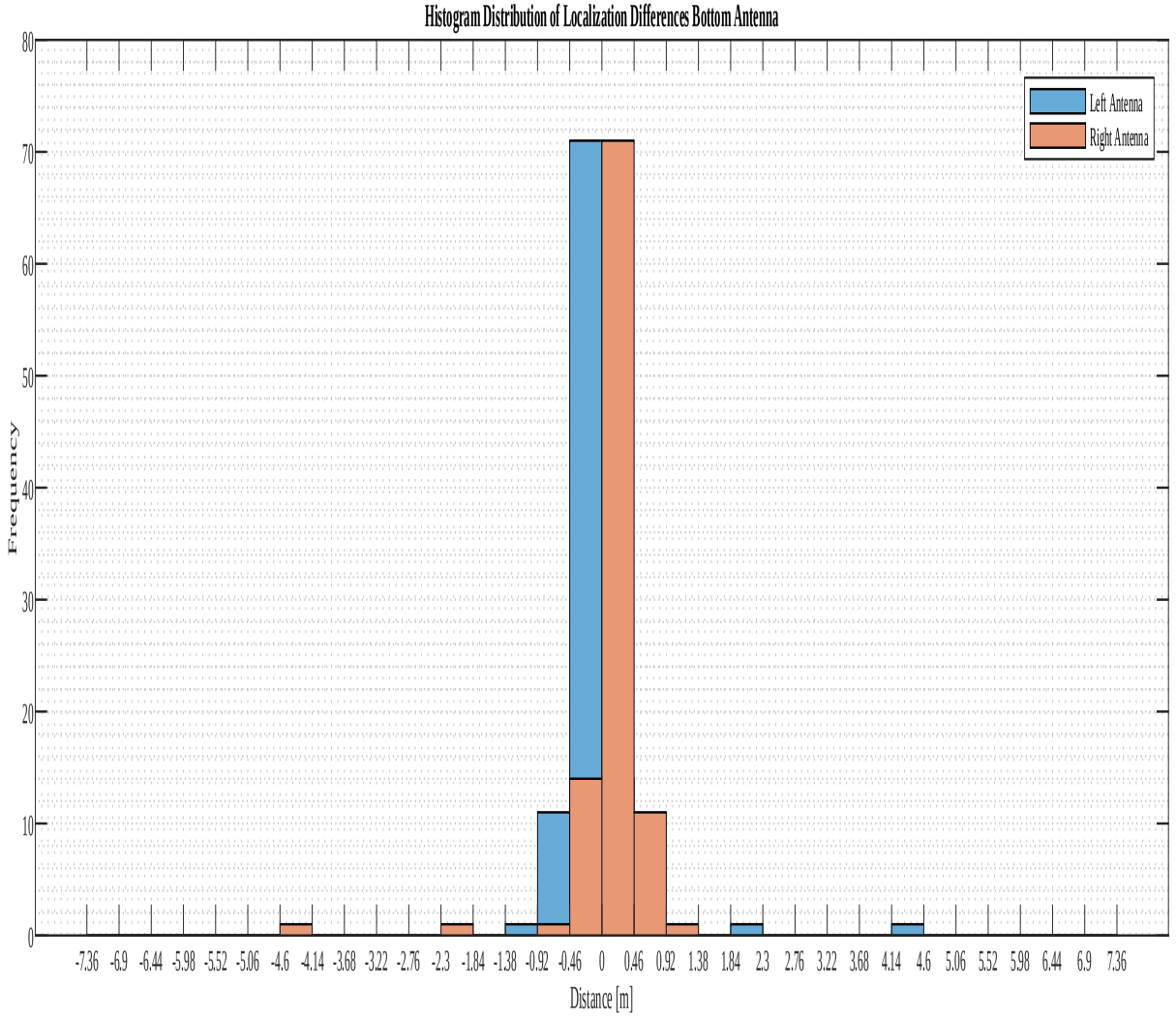

Figure 123: TPD Method Histogram of Distance Distribution of Bottom Antenna - Location B

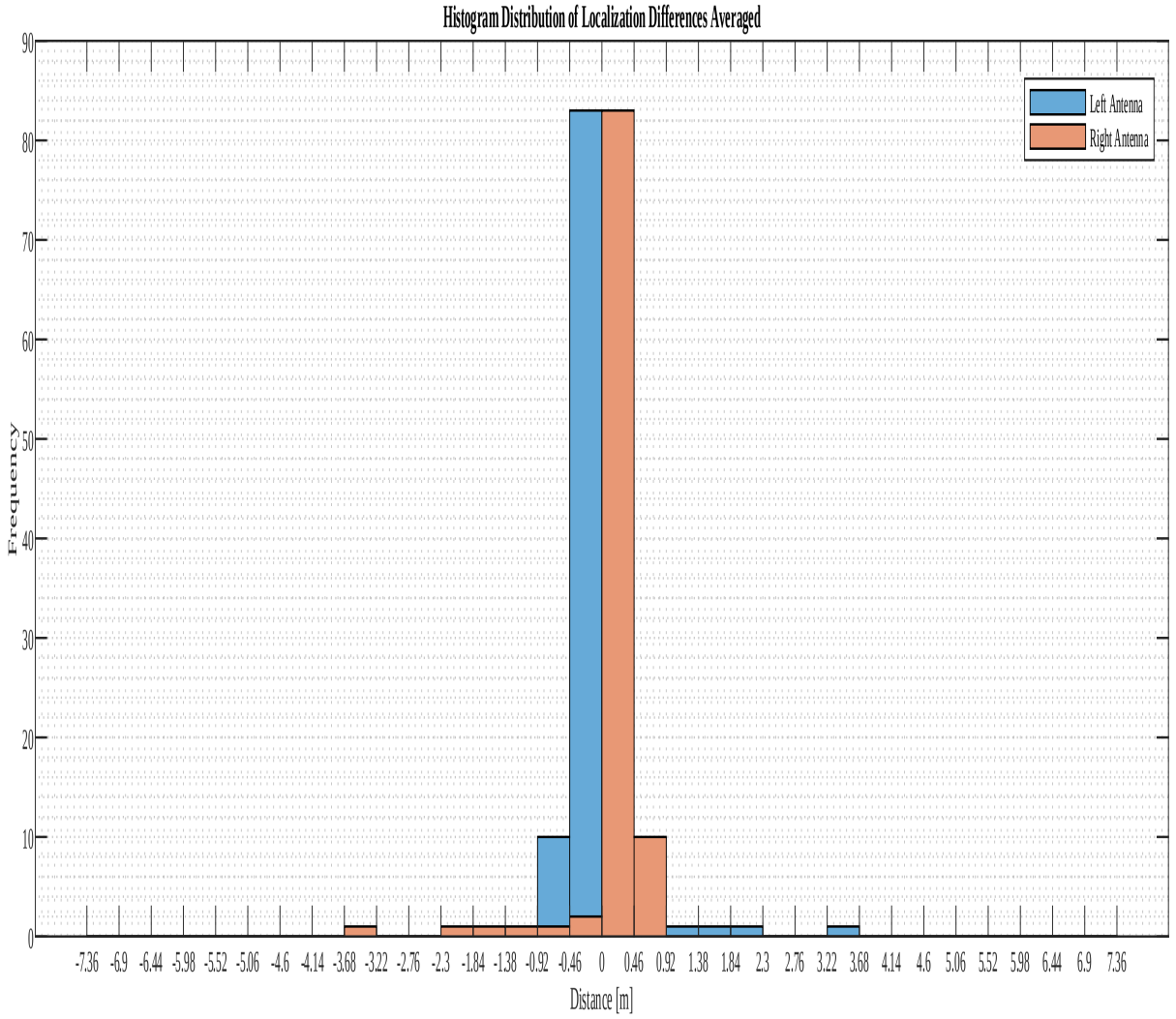

Figure 124: TPD Method Histogram Average Distance Distribution of Top & Bottom Antenna - Location B

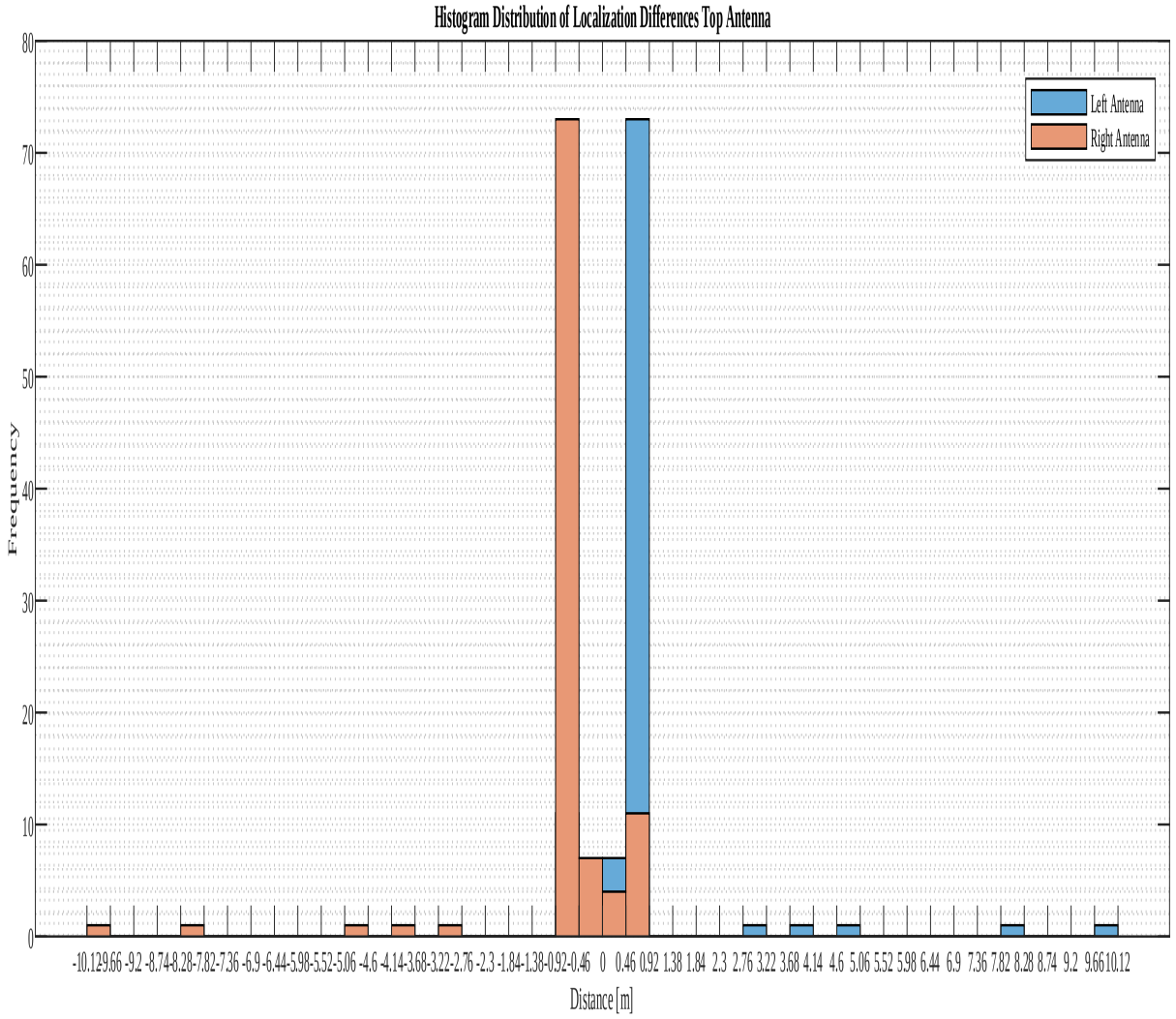

Figure 125: TPD Method Histogram of Distance Distribution of Top Antenna - Location D

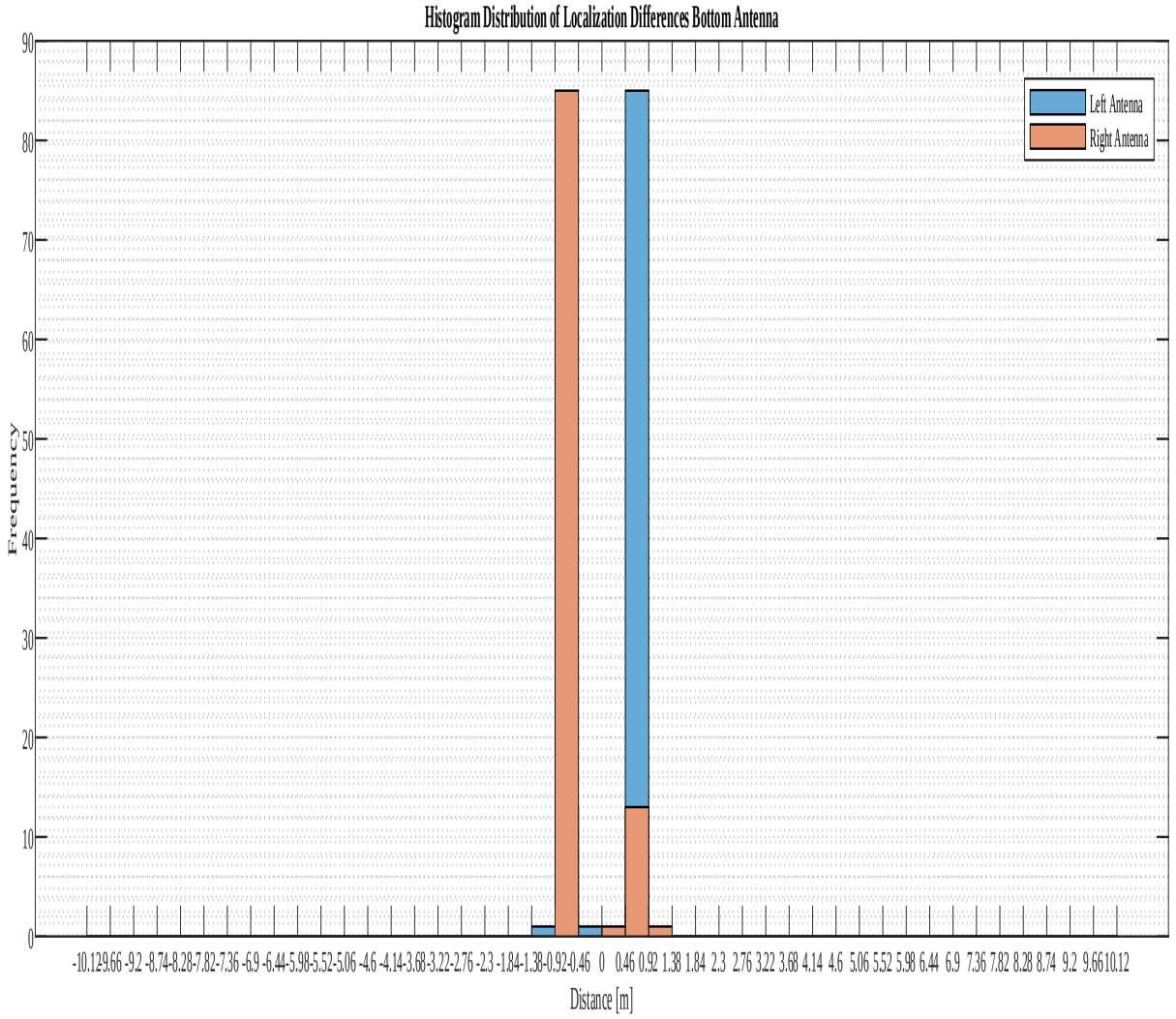

Figure 126: TPD Method Histogram of Distance Distribution of Bottom Antenna - Location D

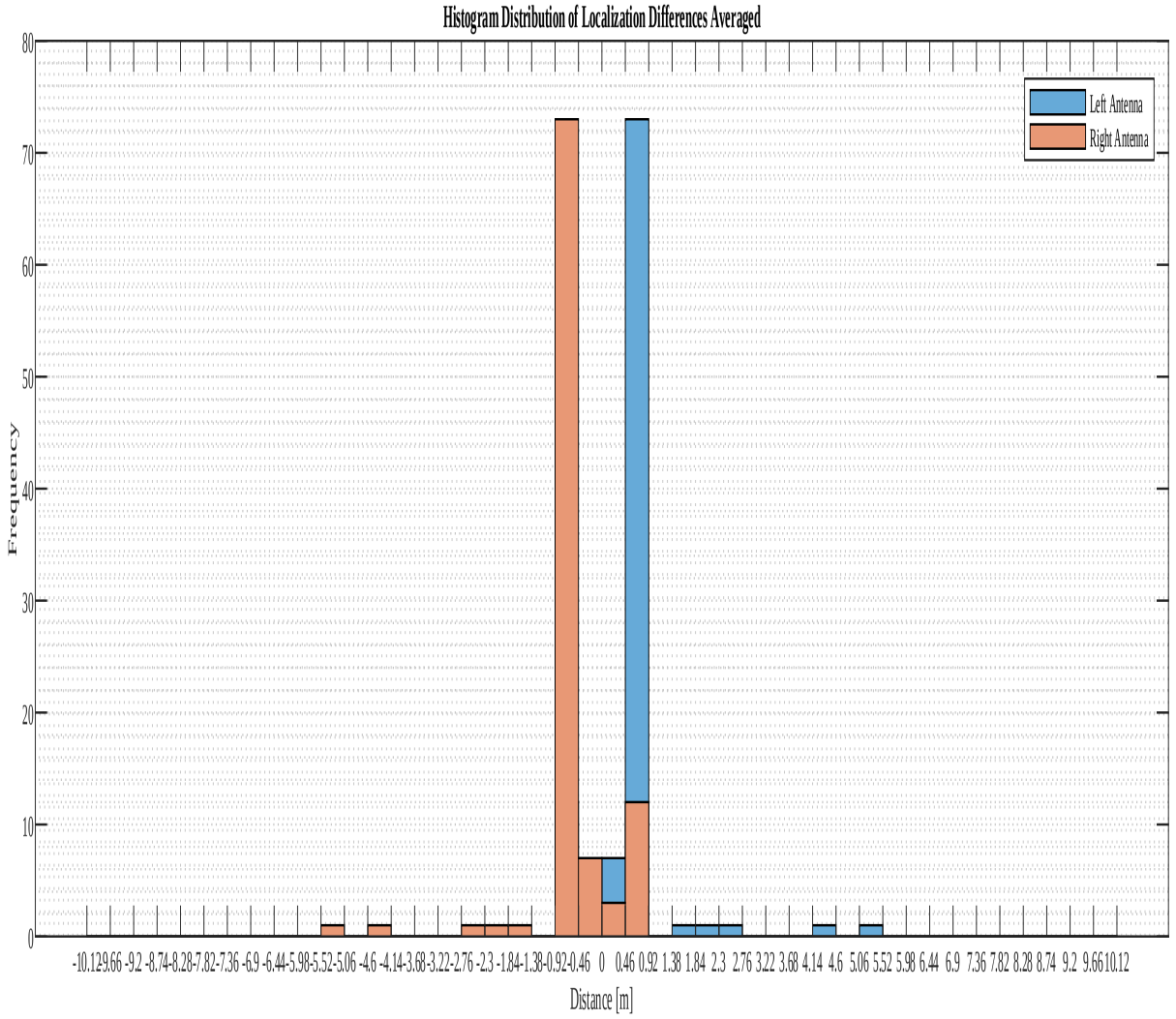

Figure 127: TPD Method Histogram Average Distance Distribution of Top & Bottom Antenna - Location D

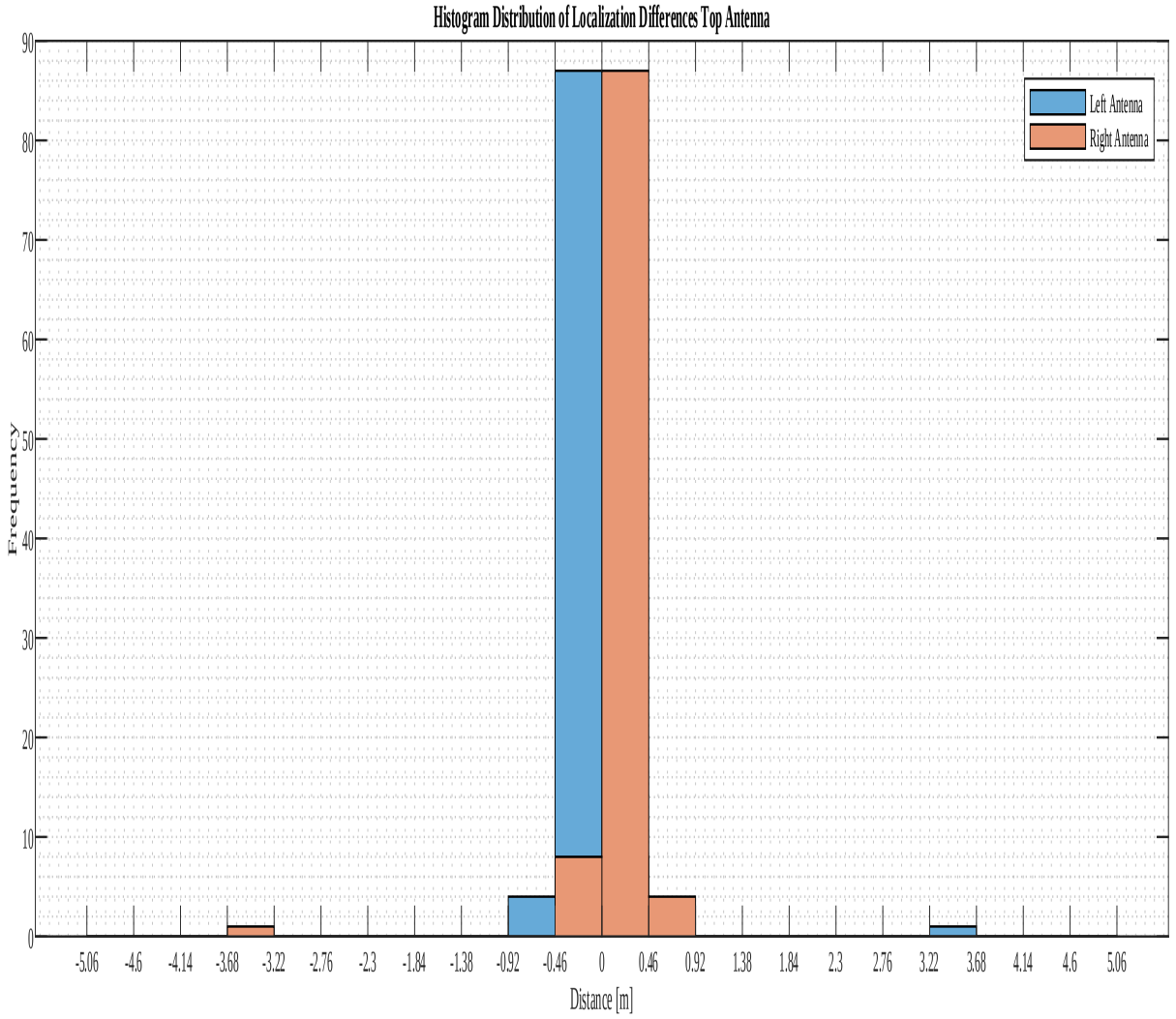

Figure 128: EC Method Histogram of Distance Distribution of Top Antenna - Location B

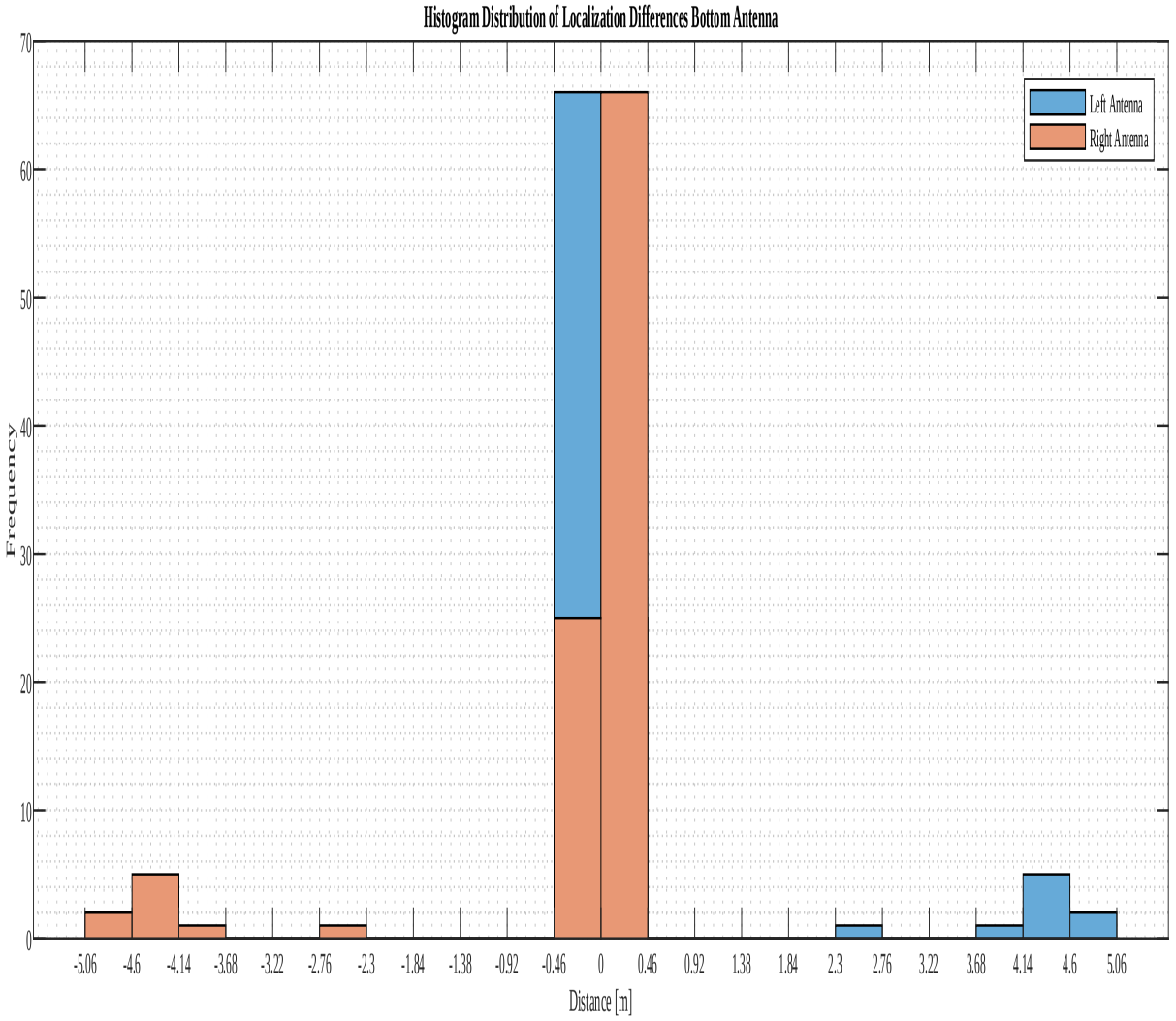

Figure 129: EC Method Histogram of Distance Distribution of Bottom Antenna - Location B

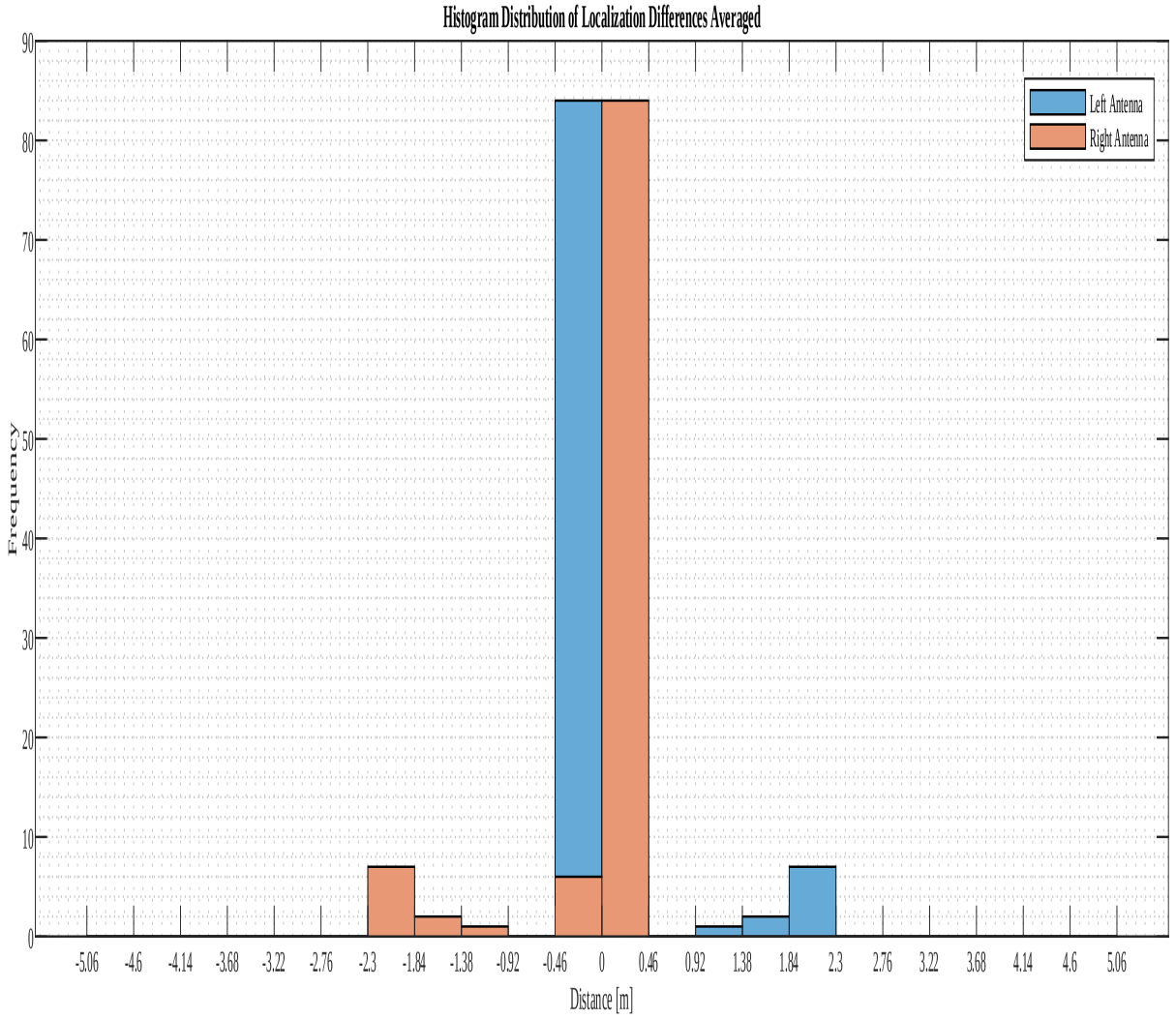

Figure 130: EC Method Histogram Average Distance Distribution of Top & Bottom Antenna - Location B

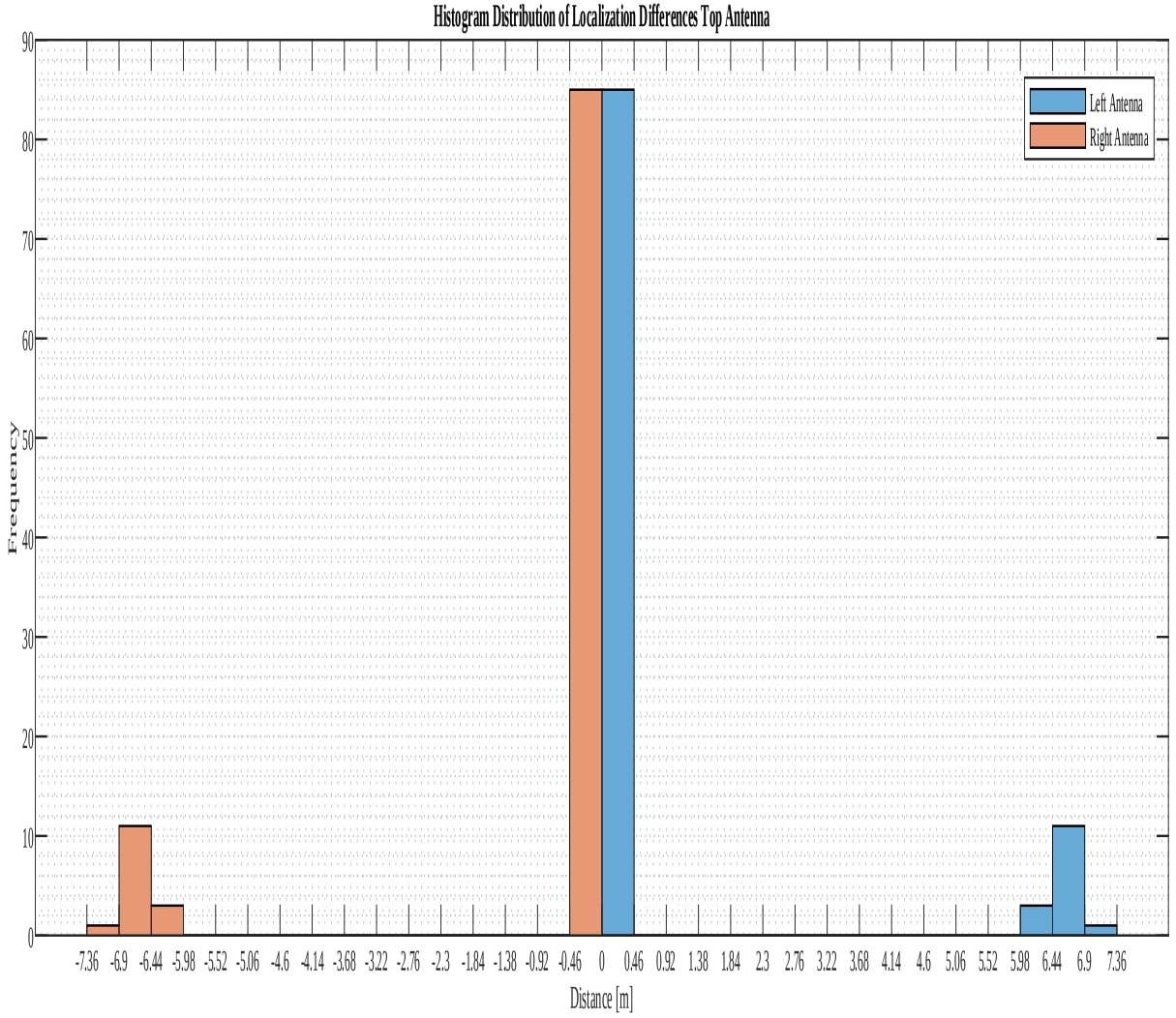

Figure 131: EC Method Histogram of Distance Distribution of Top Antenna - Location D

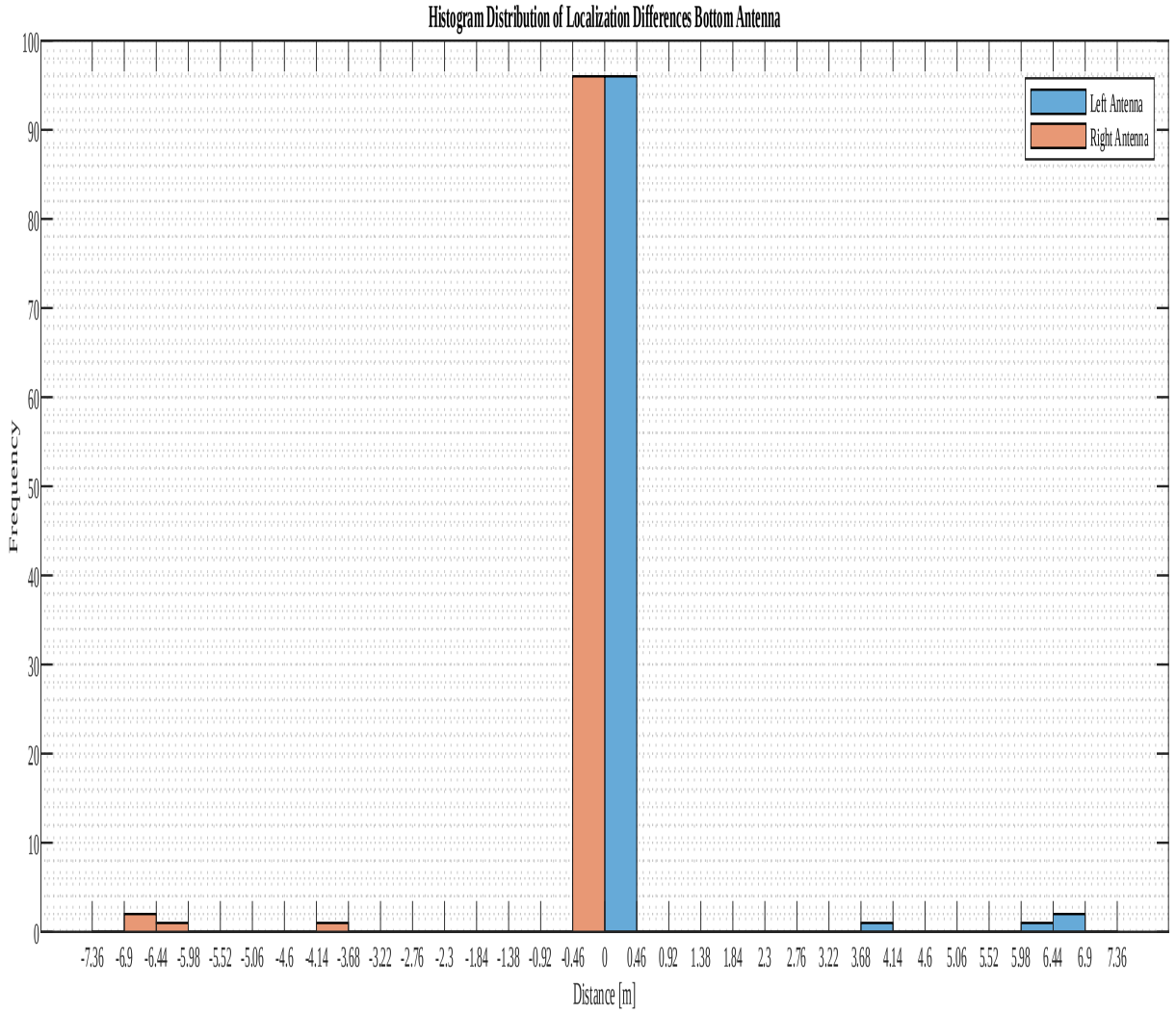

Figure 132: EC Method Histogram of Distance Distribution of Bottom Antenna - Location D

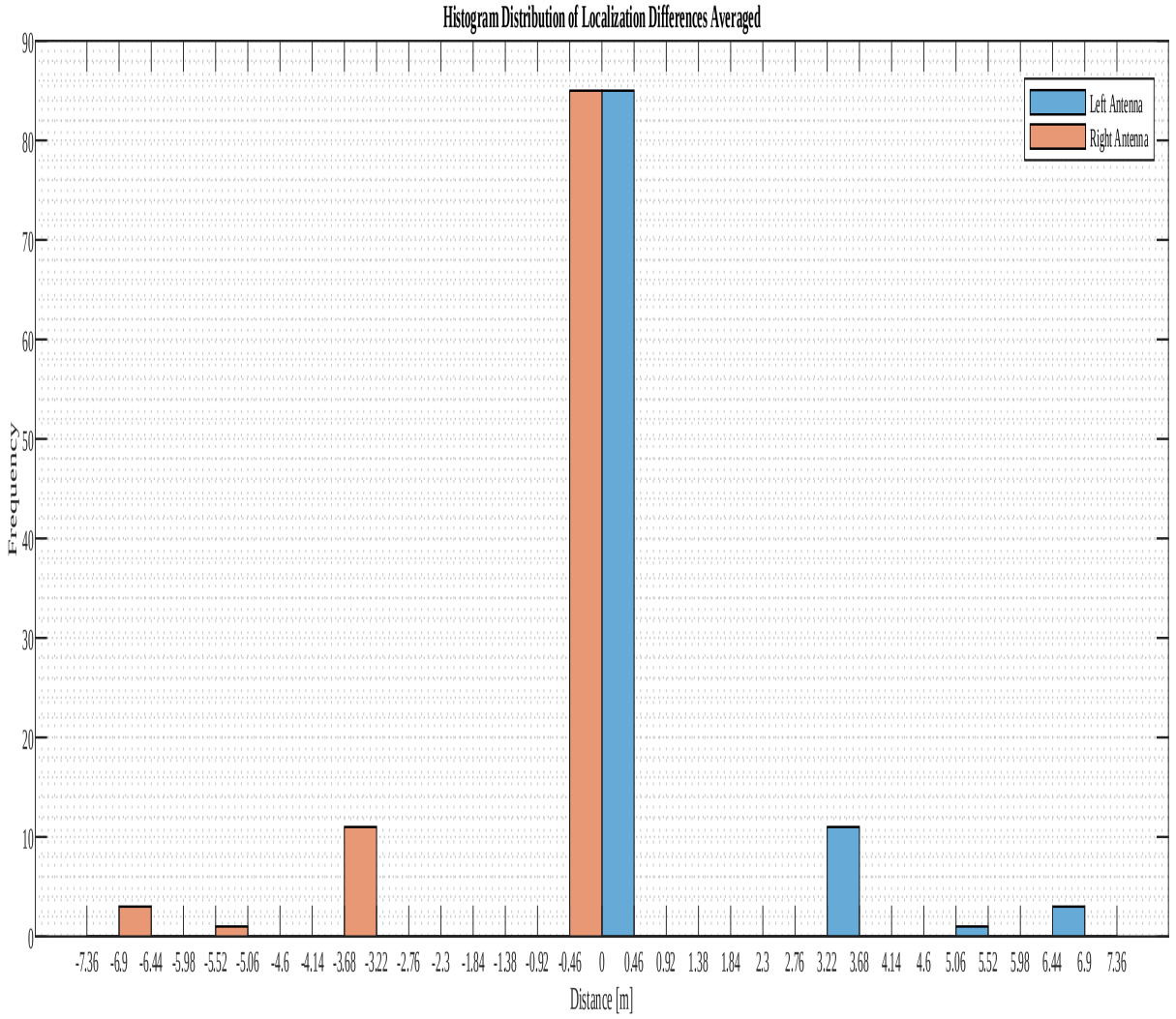

Figure 133: EC Method Histogram Average Distance Distribution of Top & Bottom Antenna - Location D

References

[1] RVO, "The roadmap from 1,000 to 4,500 MW offshore wind capacity," Offshore wind energy in the Netherlands , Mar-2015. [Online]. Available: https://www.rvo.nl/sites/default/files/2015/03/OffshorewindenergyintheNetherlands.pdf.[Accessed:31-May-2020].

[2] TenneT, "TenneT Offshore Documents," TenneT Offshore Documents, 2020. [Online]. Available: https://offshore-documents.tennet.eu/nl/. [Accessed: 31-May-2020].

[3] OffshoreStiftung, "PROMOTioN - Progress on Meshed HVDC Offshore Transmission Networks," PROMOTioN - Progress on Meshed HVDC Offshore Transmission Networks — German Offshore Wind Energy Foundation, 27-May-2020. [Online]. Available: https://www.offshore-stiftung.de/en/PROMOTioN. [Accessed: 31-May-2020].

[4] ABB, "Why HVDC Economic and environmental advantages - Why choose HVDC over HVAC," ABB . [Online]. Available: https://new.abb.com/systems/hvdc/why-hvdc/economic-and-environmental-advantages. [Accessed: 01-Jun-2020].

[5] DNV GL, "PROMOTioN," DNV GL. [Online]. Available: https://www.dnvgl.com/cases/promotion-80645. [Accessed: 31-May-2020].

[6] PROMOTioN, "Succesful completion of HVDC gas insulated switchgear (GIS) test installation," PROMOTioN, 08-Oct-2018. [Online]. Available: https://www.promotion-offshore.net/news_events/news/detail/succesful-completion-of-hvdc-gas-insulated-switchgear-gis-test-installation/. [Accessed: 09-Jun-2020].

[7] ABB, "Gas-insulated switchgear," ABB HV GIS. [Online]. Available: https://new.abb.com/high-voltage/gis. [Accessed: 04-Oct-2019].

[8] F. Neuhof, "Gearing up," Utilities Middle East, 19-Jul-2010. [Online]. Available: https://www.utilities-me.com/article-641-gearing-up. [Accessed: 28-Oct-2019].

[9] F. H. Kreuger, Industrial high voltage: 4. Coordinating - 5. Testing - 6. Measuring. Delft: Delft University Press, 1992.

[10] Stone, G.C. & Sedding, H.G. & Chan, C. & Wendel, C.. (2018). Comparison of Low Frequency and High Frequency PD Measurements on Rotating Machine Stator Windings. 349-352. 10.1109/EIC.2018.8481128.

[11] M. Escurra, "Characterization of a new method for partial discharges measurements in HVDC GIS," TU Delft Repositories, 01-Jan-1970. [Online]. Available: http://resolver.tudelft.nl/uuid:b6309cea-238c-4e27-b211-bbed15af8b40. [Accessed: 25-Sep-2019].

[12] A. Rodrigo-Mor, F. Muñoz, and L. Castro-Heredia, "A Novel Antenna for Partial Discharge Measurements in GIS Based on Magnetic Field Detection," Sensors, vol. 19, no. 4, p. 858, Feb. 2019.

[13] A. R. Mor, L. C. Heredia, and F. Muñoz, "A magnetic loop antenna for partial discharge measurements on GIS," International Journal of Electrical Power & Energy Systems, vol. 115, p. 105514, 2020.

[14] Fuping Zeng, Ju Tang, Xiaoxing Zhang, Siyuan Zhou and Cheng Pan (October 17th 2018). Typical Internal Defects of Gas-Insulated Switchgear and Partial Discharge Characteristics, Simulation and Modelling of Electrical Insulation Weaknesses in Electrical Equipment, Ricardo Albarracín Sánchez, IntechOpen, DOI: 10.5772/intechopen.79090. Available from: https://www.intechopen.com/books/simulation-and-modelling-of-electrical-insulation-weaknesses-in-electrical-equipment/typical-internal-defects-of-gas-insulated-switchgear-and-partial-discharge-characteristics

[15] Williams, Jim. "High Speed Amplifier Techniques A Designer's Companion for Wideband Circuitry." AN47 - High Speed Amplifier Techniques Application Note Linear Technology Corporation, Aug. 1991, pp. 93–95., https://www.analog.com/media/en/technical-documentation/application-notes/an47fa.pdf.

[16] V. Aaradhi y K. Gaidhani, «Partial discharge in Gas Insulated Substations (GIS): A Development and Engineering Perspective,» de Environment and Electrical Engineering (EEEIC), 2013 12th International Conference on, Wroclaw, 2013.

[17] Mor, Armando & Heredia, Luis & Muñoz, Fabio. (2018). A Novel Approach for Partial Discharge Measurements on GIS Using HFCT Sensors. Sensors. 18. 4482. 10.3390/s18124482.

[18] Boeck, W.; Albiez, M.; Bengtsson, T.; Diessner, A.; Feger, R.; Feser, K.; Girodet, A.; Gulski, E.; Hampton, B.F.; Hücker, T.; Judd, M.D.; et al. Partial discharge detection system for GIS: Sensitivity verification for the UHF method and the acoustic method. Electra 1999, 153, 75–87.

[19] Arthur Anderson, "BOM Tool," All About Circuits. [Online]. Available: https://www.allaboutcircuits.com/technical-articles/transmission-lines-from-lumped-element-to-distributed-element-regimes/. [Accessed: 03-Nov-2019].

[20] Hoek, Stefan & Riechert, Uwe & Strehl, Thomas & Feser, Kurt & Tenbohlen, Stefan. (2007). New Procedures for Partial Discharge Localization in Gas-Insulated Switchgears in Frequency and Time Domain.

[21] P. Wagenaars, P. A. A. F. Wouters, P. C. J. M. van der Wielen and E. F. Steennis, "Accurate estimation of the time-of-arrival of partial discharge pulses in cable systems in service," in IEEE Transactions on Dielectrics and Electrical Insulation, vol. 15, no. 4, pp. 1190-1199, August 2008, doi: 10.1109/T-DEI.2008.4591242.

[22] P. Wagenaars, P. A. A. F. Wouters, P. C. J. M. van der Wielen and E. F. Steennis, "Algorithms for Arrival Time Estimation of Partial Discharge Pulses in Cable Systems," Conference Record of the 2008 IEEE International Symposium on Electrical Insulation, Vancouver, BC, 2008, pp. 694-697, doi: 10.1109/ELINSL.2008.4570425.

[23] X. Li, X. Wang, A. Yang and M. Rong, "Partial Discharge Source Localization in GIS Based on Image Edge Detection and Support Vector Machine," in IEEE Transactions on Power Delivery, vol. 34, no. 4, pp. 1795-1802, Aug. 2019, doi: 10.1109/TPWRD.2019.2925034.

[24] Muñoz-Muñoz, Fabio Rodrigo-Mor, Armando. (2020). Partial Discharges and Noise Discrimination Using Magnetic Antennas, the Cross Wavelet Transform and Support Vector Machines. Sensors. 20. 3180. 10.3390/s20113180.